Title
Improving the Resolving Power of Ultraviolet to Near-Infrared Microwave Kinetic Inductance Detectors

Author
Zobrist, Nicholas Reinhard

Publication Date
2022

University of California, Santa Barbara

Improving the Resolving Power of Ultraviolet to Near-Infrared Microwave Kinetic Inductance Detectors

A dissertation submitted in partial satisfaction of the

requirements for the degree of

Doctor of Philosophy

in

Physics

by

Nicholas Reinhard Zobrist

Committee in charge:

Professor Benjamin A. Mazin, Chair

Professor Ania Jayich

Professor Omer Blaes

June 2022

The Dissertation of Nicholas Reinhard Zobrist is approved.

Professor Omer Blaes

Professor Ania Jayich

Professor Benjamin A. Mazin, Committee Chair

June 2022

Improving the Resolving Power of Ultraviolet to Near-Infrared Microwave Kinetic Inductance Detectors

by

Nicholas Reinhard Zobrist

To my family for always supporting me

Acknowledgments

A Ph.D. doesn't just happen by itself. Countless people have helped me along the way, and, for that, I am in all of your debt. It is not possible to list everyone who influenced my research over the past six years, but I'd like to acknowledge some of the most significant contributions here.

My thesis advisor, Ben Mazin, continues to work tirelessly both to advance the field of low temperature detectors and to foster a positive research experience for his students. I am extremely grateful for the opportunities that I've had working in his lab and for all of his advice. It is safe to say that none of this work would be possible without him.

To my labmates, thank you for all of your insightful conversations over the years. The office has never been a boring place, and I've learned so much just by listening to your individual research struggles. Specifically, I'd like to thank Seth Meeker for giving me a comprehensive introduction to microwave electronics and astrophysical instrumentation. I've always been impressed by your complete understanding of your projects, and I hope a bit of that thoroughness has rubbed off on me. In addition, Neelay Fruitwala deserves a medal for helping me sort out factors of two in the noise calculations for this dissertation. He also has been an invaluable resource whenever I strayed anywhere close to code that needs to be compiled.

All of the devices that I've tested and designed at UCSB had to be fabricated first.

Thank you Paul Szypryt, Grégoire Coiffard, Miguel Daal, and Bruce Bumble for your work in the clean room. You've taught me so much about micro-fabrication techniques. Your work is often as much an art as a science, and your dedication to the field can be clearly seen in the results.

Miguel, thank you as well for being such a good mentor. It is relatively uncommon to have the opportunity to work with one's undergraduate research advisor in graduate school. You helped me tremendously by bridging the gap between the dark matter and photon detector communities. I'm glad that we ended up in the same place for such a long time. I wish you the best of luck with your future research.

Thank you, also, to NASA for providing much of the funding that enabled this work. My advisor at the Jet Propulsion Laboratory, Peter Day, has always been generous with his time and lab resources. Your parametric amplifiers have really revolutionized the capabilities of our detectors.

On a personal note, graduate school can sometimes be stressful. I am so lucky to be able to rely on the love and support of my family and friends. Climbing in the hills outside Santa Barbara has been a wonderful distraction to that end. Thank you Andrew Baish for teaching me the ropes and all of the best spots. Reminders that not everything interesting is physics have also regularly been welcome. Thank you Dylan Nesbit for bringing a bit of classics-diversity to our friend group. Jamie Burke, I apologize for all of my bad jokes during graduate school, but I very much appreciate consistently being able to rely on at least a courtesy laugh from you. Zach Porter, thank you for convincing me that birds are, in fact, real. You will definitely remain my go-to source for bird related trivia. Finally, I have always been able to count on my good friend Alex Dorsett when times get tough. Thank you for helping maintain my general sanity and for pushing me to be more passionate about my hobbies.

Curriculum Vitæ

Nicholas Reinhard Zobrist

Education

2019 M.A. in Physics — University of California, Santa Barbara

2015 B.A in Physics and Applied Mathematics — University of California, Berkeley

Honors and Awards

2020 Eddleman Summer Research Fellowship Mentor

2017 NASA Space Technology Research Fellowship

Publications

[1] **N. Zobrist**, W. H. Clay, G. Coiffard, M. Daal, N. Swimmer, P. Day, and B. A. Mazin, "Membrane-less phonon trapping and resolution enhancement in optical microwave kinetic inductance detectors", 2022, arXiv:2204.13669 [astro-ph.IM].

[2] S. Steiger, J. I. Bailey, **N. Zobrist**, N. Swimmer, R. Dodkins, K. K. Davis, and B. A. Mazin, "The MKID Pipeline: A Data Reduction and Analysis Pipeline for UVOIR MKID Data", The Astronomical Journal **163**, 193 (2022).

[3] J. M. Miller, **N. Zobrist**, G. Ulbricht, and B. A. Mazin, "Improving the energy resolution of photon counting microwave kinetic inductance detectors using principal component analysis", Journal of Astronomical Telescopes, Instruments, and Systems **7**, 1–10 (2021).

[4] S. Steiger, T. Currie, T. D. Brandt, O. Guyon, M. Kuzuhara, J. Chilcote, T. D. Groff, J. Lozi, A. B. Walter, N. Fruitwala, J. I. Bailey, III, **N. Zobrist**, N. Swimmer, I. Lipartito, J. P. Smith, C. Bockstiegel, S. R. Meeker, G. Coiffard, R. Dodkins, P. Szypryt, K. K. Davis, M. Daal, B. Bumble, S. Vievard, A. Sahoo, V. Deo, N. Jovanovic, F. Martinache, G. Doppmann, M. Tamura, N. J. Kasdin, and B. A. Mazin, "SCExAO/MEC and CHARIS Discovery of a Low-mass, 6 au Separation Companion to HIP 109427 Using Stochastic Speckle Discrimination and High-contrast Spectroscopy*", The Astronomical Journal **162**, 44 (2021).

[5] **N. Zobrist**, N. Klimovich, B. Ho Eom, G. Coiffard, M. Daal, N. Swimmer, S. Steiger, B. Bumble, H. G. LeDuc, P. Day, and B. A. Mazin, “Improving the dynamic range of single photon counting kinetic inductance detectors”, Journal of Astronomical Telescopes, Instruments, and Systems **7**, 010501 (2021).

[6] J. P. Smith, B. A. Mazin, A. B. Walter, M. Daal, J. I. Bailey III, C. Bockstiegel, **N. Zobrist**, N. Swimmer, S. Steiger, and N. Fruitwala, “Flexible Coaxial Ribbon Cable for High-Density Superconducting Microwave Device Arrays”, IEEE Transactions on Applied Superconductivity **31**, 1–5 (2021).

[7] N. J. Swimmer, B. A. Mazin, C. Bockstiegel, J. I. Bailey, G. Coiffard, M. Daal, K. Davis, N. Fruitwala, I. Lipartito, J. Smith, S. Steiger, **N. Zobrist**, T. Cook, S. Chakrabarti, C. Mendillo, J. Martel, and K. Hewawasam, “The PICTURE-C MKID camera”, in Ground-based and Airborne Instrumentation for Astronomy VIII, edited by C. J. Evans, J. J. Bryant, and K. Motohara (Dec. 2020), p. 79.

[8] N. Fruitwala, P. Strader, G. Cancelo, T. Zmuda, K. Treptow, N. Wilcer, C. Stoughton, A. B. Walter, **N. Zobrist**, G. Collura, I. Lipartito, J. I. Bailey, and B. A. Mazin, “Second generation readout for large format photon counting microwave kinetic inductance detectors”, Review of Scientific Instruments **91**, 124705 (2020).

[9] A. B. Walter, N. Fruitwala, S. Steiger, J. I. Bailey, **N. Zobrist**, N. Swimmer, I. Lipartito, J. P. Smith, S. R. Meeker, C. Bockstiegel, G. Coiffard, R. Dodkins, P. Szypryt, K. K. Davis, M. Daal, B. Bumble, G. Collura, O. Guyon, J. Lozi, S. Vievard, N. Jovanovic, F. Martinache, T. Currie, and B. A. Mazin, “The MKID Exoplanet Camera for Subaru SCExAO”, Publications of the Astronomical Society of the Pacific **132**, 125005 (2020).

[10] G. Coiffard, M. Daal, **N. Zobrist**, N. Swimmer, S. Steiger, B. Bumble, and B. A. Mazin, “Characterization of sputtered hafnium thin films for high quality factor microwave kinetic inductance detectors”, Superconductor Science and Technology **33**, 07LT02 (2020).

[11] **N. Zobrist**, G. Coiffard, B. Bumble, N. Swimmer, S. Steiger, M. Daal, G. Collura, A. B. Walter, C. Bockstiegel, N. Fruitwala, I. Lipartito, and B. A. Mazin, “Design and performance of hafnium optical and near-IR kinetic inductance detectors”, Applied Physics Letters **115**, 213503 (2019).

[12] **N. Zobrist**, B. H. Eom, P. Day, B. A. Mazin, S. R. Meeker, B. Bumble, H. G. LeDuc, G. Coiffard, P. Szypryt, N. Fruitwala, I. Lipartito, and C. Bockstiegel, “Wide-band parametric amplifier readout and resolution of optical microwave kinetic inductance detectors”, Applied Physics Letters **115**, 042601 (2019).

[13] **N. Zobrist**, M. Daal, J. Y. Corbin, B. Sadoulet, and B. Mazin, “Disk Resonator Design for Kinetic Inductance Detectors”, Journal of Low Temperature Physics **194**, 394–403 (2019).

[14] M. Daal, **N. Zobrist**, N. Kellaris, B. Sadoulet, and M. Robertson, “Properties of selected structural and flat flexible cabling materials for low temperature applications”, Cryogenics **98**, 47–59 (2018).

[15] A. Walter, B. A. Mazin, C. Bockstiegel, N. Fruitwala, P. Szypryt, I. Lipartito, S. Meeker, **N. Zobrist**, G. Collura, G. Coiffard, P. Strader, O. Guyon, J. Lozi, and N. Jovanovic, “MEC: the MKID exoplanet camera for high contrast astronomy at Subaru (Conference Presentation)”, in Ground-based and Airborne Instrumentation for Astronomy VII, Vol. 10702, edited by H. Takami, C. J. Evans, and L. Simard (July 2018), p. 31.

[16] S. R. Meeker, B. A. Mazin, A. B. Walter, P. Strader, N. Fruitwala, C. Bockstiegel, P. Szypryt, G. Ulbricht, G. Coiffard, B. Bumble, G. Cancelo, T. Zmuda, K. Treptow, N. Wilcer, G. Collura, R. Dodkins, I. Lipartito, **N. Zobrist**, M. Bottom, J. C. Shelton, D. Mawet, J. C. van Eyken, G. Vasisht, and E. Serabyn, “DARKNESS: A Microwave Kinetic Inductance Detector Integral Field Spectrograph for High-contrast Astronomy”, Publications of the Astronomical Society of the Pacific **130**, 065001 (2018).

[17] S. Rajendran, **N. Zobrist**, A. A. O. Sushkov, R. Walsworth, and M. Lukin, “A method for directional detection of dark matter using spectroscopy of crystal defects”, Physical Review D **96**, 035009 (2017).

[18] P. Szypryt, S. R. Meeker, G. Coiffard, N. Fruitwala, B. Bumble, G. Ulbricht, A. B. Walter, M. Daal, C. Bockstiegel, G. Collura, **N. Zobrist**, I. Lipartito, and B. A. Mazin, “Large-format platinum silicide microwave kinetic inductance detectors for optical to near-IR astronomy”, Optics Express **25**, 25894 (2017).

[19] **N. R. Zobrist**, M. Daal, B. Sadoulet, and S. Golwala, “A Distributed Method for Modeling Effective Cryogenic Flat Cable Heat Sinking”, Journal of Low Temperature Physics **176**, 1096–1102 (2014).

Abstract

Improving the Resolving Power of Ultraviolet to Near-Infrared Microwave Kinetic Inductance Detectors

by

Nicholas Reinhard Zobrist

Detection of ultraviolet to near-infrared light is useful for a variety of applications from dark matter searches to biological imaging and astronomy. The performance of these detectors often limits the achievable science goals for an application, so improvements to detector technologies can be transformative. This dissertation focuses on these detector enhancements, emphasizing the requirements for one particular application, exoplanet direct imaging. However, the work done here remains broadly applicable to fields needing highly sensitive sensors in this wavelength range.

Finding and studying the properties of exoplanets orbiting distant stars can tell us much about solar system dynamics and the formation of our own solar system. With sufficiently precise measurements we might also discover the presence of water or even biological processes on these planets. To achieve this goal, we need astronomical instrumentation capable of separating an exoplanet's light from its host star by directly imaging it. For many exoplanets, though, we receive at our telescope only roughly one photon for every billion from the star. Even worse, these two light sources often partially overlap because of the relative closeness of exoplanets to their stars and the diffraction limit set by the finite size

of our telescope optics. Therefore, the extreme contrast ratio between the brightness of the star and planet sets the performance requirements for this kind of instrument.

Carrying out this measurement with the traditional semiconductor based sensors can be difficult. They detect the intensity of light at each pixel and introduce excess noise into the system. However, superconducting sensors avoid this limitation because of their extra sensitivity. Each individual incident photon can be resolved making them essentially perfect photon counting detectors, which enables the detection of exoplanets with more challenging contrast ratios than detectable with conventional detectors. The system noise in a superconducting sensor, instead, determines how accurately the photon energy can be measured through the size of the detector response. Because of this extra energy measurement capability these detectors do not need the complicated optical systems typically used to measure an exoplanet's atmospheric spectrum. The accuracy at which we can resolve these planetary spectra determines how much we can learn about a planet and, as such, is the principal metric for the performance of these devices.

The Microwave Kinetic Inductance Detector (MKID) is unique among other superconducting technologies because it allows for the simple readout of tens to hundreds of thousands of pixels, which is a requirement for when the exact location of an exoplanet is unknown. This dissertation focuses on improving the spectral resolving power of MKIDs to make them the superior option for ultraviolet to near-infrared measurements and, in particular, for exoplanet direct imaging. Chapters 1 and 2 discuss the significance of MKIDs as astronomical detectors and the relevant physics needed to understand their operation. In the following chapters, four separate areas where I have contributed to the advancement of MKIDs are laid out. Chapter 3 covers improvements to the data analysis. A new sensor material for MKIDs is characterized in chapter 4. Chapter 5 shows how the readout scheme can be improved to lower the system noise. Finally, in chapter 6 improvements are made to the detector geometry. With the advancements considered in this dissertation, both the spectral range and resolving power of MKIDs have been increased by a factor of 3.

Table of Contents

List of Figures

List of Tables

List of Terms

ARCONS Array Camera for Optical to Near-IR Spectrophotometry. 13, 50, 51

BCS The Bardeen, Cooper, and Schrieffer theory of superconductivity. 16, 17, 19, 24, 25, 88

DARKNESS DARK-speckle Near-infrared Energy-resolving Superconducting Spectrophotometer. 13, 14, 50, 52

DFT Discrete Fourier Transform. 112, 113

EMCCD Electron-Multiplying Charge-Coupled Device. 8, 108

HEMT High Electron Mobility Transistor. 63, 69, 71, 74–76, 78, 79, 133, 134, 136

IFS Integral Field Spectrograph. 5, 7, 9, 14, 90, 108, 109

MEC MKID Exoplanet Camera. 12–14, 50, 52, 80, 85

MKID Microwave Kinetic Inductance Detector. xii, xiii, 12–15, 22, 23, 25, 29, 33, 36, 46, 48–50, 52, 53, 57, 60, 63–66, 69, 74–76, 78–82, 85–89, 92, 93, 95, 97, 98, 102, 108–111, 133, 134

PMMA Polymethyl Methacrylate. 55, 94, 95

PSD Power Spectral Density. 38, 66–68, 70, 130, 131, 133, 134

STJ Superconducting Tunnel Junction. 11, 14, 88, 108

TES Transition Edge Sensor. 11, 14, 108

TKID Thermal Kinetic Inductance Detector. 25, 48

TLS Two-Level System. 60–62, 65, 72–74, 80, 109, 133

TWPA Traveling Wave Parametric Amplifier. 75, 76, 78–82, 85–87, 130, 133–135, 137

1

Introduction and Motivation

Energy resolving, single photon counting detectors sensitive to light in the ultraviolet to near-infrared wavelength range are useful in a variety of different fields. In bio-analysis research, there is demand for detectors that can measure fast, low-light biological processes with energy sensitivity [1]. Axion and hidden photon dark matter searches, too, could benefit from these kinds of detectors by expanding the searchable parameter space into the 0.1 to 10 $\mathrm{eV\,c^{-2}}$ mass range [2]. Here, we specialize to a particular astrophysical application for these detectors, exoplanet direct imaging, to emphasize the usefulness of this technology and since it is the current focus of our research group. However, the improvements discussed within have a broader significance to any photon-starved application requiring a fast, wide field of view detector with energy resolution in this wavelength range.

Exoplanets—planets orbiting stars other than our own—are the primary motivator for this dissertation. Studying them provides us with a way to understand our own solar system. Through the distribution of observed exoplanets, we can gauge how common or unique our home is. By looking at similar systems at different stages after their formation, we can understand their evolution. Ultimately, we are interested in the signatures of life and determining the prevalence of conditions conducive to it. This chapter will introduce the rest of this dissertation by further discussing the science goals of exoplanet astronomy and how they inform the kinds of instrumentation we use to study these systems.

1.1 Exoplanet Spectroscopy

Two different techniques have been developed that can both detect and probe the atmospheric composition of exoplanets: transit and direct imaging spectroscopy. In the rare case where the exoplanet orbit aligns with our own observation angle of the system, we can detect the change in brightness as the planet transits in front of its star. The atmosphere of the planet absorbs light at specific wavelengths according to its composition, and by measuring the spectral distribution of this light, we can gain information about its atmospheric components. This type of measurement is more sensitive to small planets with short orbital periods but is mostly insensitive to the distance of the star from Earth. The Kepler space telescope is responsible for over 2,600 exoplanet discoveries made through the transit method which to date accounts for more than half of all discovered exoplanets [3–5]. Direct imaging, however, aims to separate light emanating from a planet from its host star by spatially resolving the system. To do so, the star light must be suppressed using a coronagraph, and an adaptive optics system must be used to correct for atmospheric effects in ground-based observations. The spectrum of the reflected or thermally emitted light coming from the exoplanet can then be measured. Direct imaging

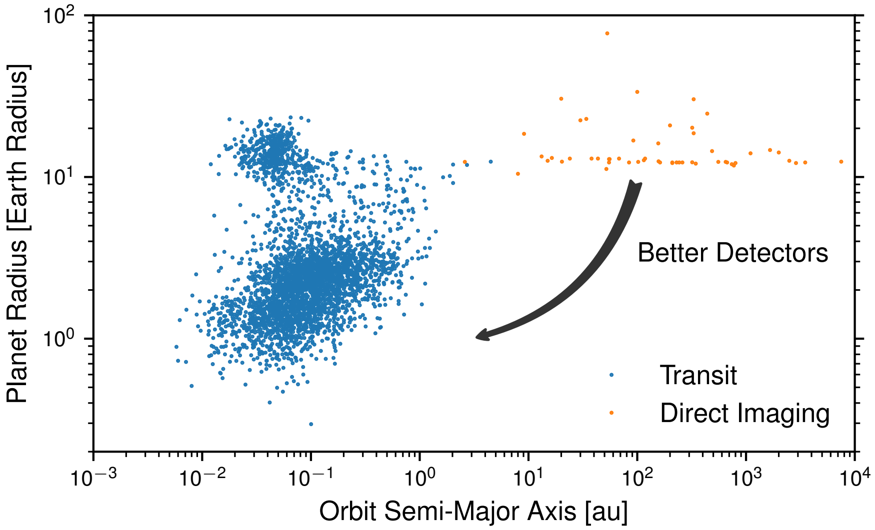

Figure 1.1: The size of discovered exoplanets and their orbits are plotted with respect to that of Earth. Planets that have been directly imaged so far are both much larger and further from their host star than Earth. New detectors should help push measurements toward the bottom left corner of the plot to compliment data from transit spectroscopy. The data plotted here were collected from reference 6.

is largely complementary to transit spectroscopy as it is most sensitive to larger planets further from their host stars and can see planets that never transit in front of their star, but the technique can only be used on nearby star systems. Figure 1.1 shows the distribution of planets already detected with these two methods and where the detector improvements discussed in this dissertation can help fill in the unmeasured exoplanet parameter space.

1.1.1 Direct Imaging

Directly imaging an exoplanet is the same as simply taking its picture. However, a normal camera cannot resolve a faint exoplanet awash in the background light of its star. Typically a large telescope is needed along with a coronagraph to block the diffracted star light while letting the light from around the star to pass. There are several ground-based observatories and instruments designed for this type of measurement: the Gemini Planet

Imager [7, 8], SPHERE [9], SCExAO [10, 11], Project 1640 and the Stellar Double Coronagraph [12, 13], the Keck Planet Imager and Characterizer [14], and MagAO-X [15]. These observatories have allowed us to measure exoplanets with brightness contrast ratios up to 10^{-6} with respect to their host star. However, they are ultimately limited in their achievable contrast by the uncontrolled scattered and diffracted light arising from atmospheric turbulence, which shows up as image speckles. Adaptive optics are typically used to correct for these aberrations and consist of a deformable mirror paired with a detector that can remove the effects of turbulence from the incoming wavefront in real time. Speckles change at a variety of speeds, so the update rate for this correction limits the precision of the wavefront control that can be done. For example, on sky demonstrations of speckle nulling, a technique for removing uncorrected speckles, typically update the wavefront control at a $<$10 Hz rate which require detectors with frame rates $\sim$100 Hz [11, 16, 17]. Reaching higher contrast ratios on the ground with this technique requires improved detectors with faster frame rates and lower noise.

To detect an earth-like planet the limits imposed by atmospheric speckles must be overcome, or a space-based observatory must be used. Space observations not only benefit from a lack of atmospheric speckles but also avoid issues with the earth's atmosphere interfering with spectral measurements. As such, several space-based missions have been proposed. HabEx is a proposed 4 m diameter space telescope featuring a starshade [18]. The LUVOIR mission would be larger with either a 15 m or 8 m diameter space telescope with no starshade [19]. Both systems would have coronagraphs along with a variety of detectors to facilitate different kinds of measurements. In the most recent decadal survey from NASA, a 6 m compromise between the LUVOIR and HabEx was prioritized [20].

However, even if work on one of these missions were to begin soon, it would not be ready to take data until far in the future. In the meantime, better ground-based instrumentation is needed to improve our ability to directly image exoplanets.

1.1.2 Detector Requirements

Several types of instruments are suitable for exoplanet direct imaging, but broadly fall into two categories: (1) low spectral resolution, wide field of view spectrometers and (2) high spectral resolution, point source spectrometers. This dissertation focuses on improvements to Integral Field Spectrographs (IFSs), which fall into the first category. IFSs are essentially cameras, but at each pixel they also measure the spectrum of incident light. These instruments are most useful for the quick, initial detection and characterization of exoplanets which is important as there are many stars to investigate. Afterward, if an exoplanet is deemed interesting enough, a higher resolution spectrometer can be used. IFS performance falls into three categories: spectral resolution, detector noise, and system throughput.

The required spectral resolution or resolving power, defined as the photon energy divided by the full-width-half-maximum energy uncertainty ($R = {}^{E}/_{\Delta E}$), is determined by the type of spectrum being observed. Exoplanet spectra vary widely depending on the planet type and age. However, the spectrum of an exoplanet similar to earth (exoearth), like shown in figure 1.2, will have spectral features for several molecules associated with life at visible to near-infrared wavelengths: O_3, H_2O, CO_2, O_2, and CH_4 [21]. The resolving power required to measure these features also depends on the exoearth's age. To

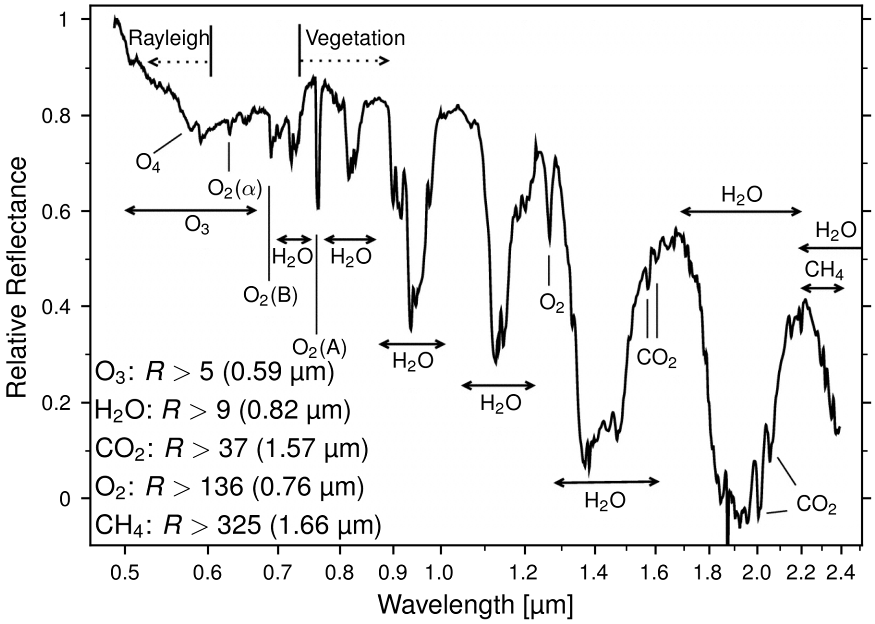

Figure 1.2: An example reflected light spectrum of an earth-like planet is shown with its different atmospheric components labeled. The data are taken from reference [21]. The minimum resolving power required to detect several molecular spectral features across all geological atmospheric epochs is tabulated on the bottom left [22]. These values represent the easiest to measure features per molecule across all visible to near-infrared wavelengths. However, other features may be measurable with lower resolving powers during particular periods in a planet's evolution or for other planet types.

ensure detection no matter the exoearth's age, strict resolving power requirements can be set [22]. The easiest to measure spectral feature for each molecule is labeled in figure 1.2. In general, O_3 and H_2O are the easiest to measure molecules with even the most difficult features requiring no more than $R > 26$. CO_2 is a medium difficulty molecule with a $R > 63$ required to measure all spectral features in the infrared and $R > 210$ in the visible. O_2 is the most difficult molecule to measure requiring $R > 244$ in the near-infrared and $R > 143$ in the visible. CH_4 is the most variable among the molecules listed here. For a majority of an exoearth's lifetime, $R > 54$ would be sufficient to measure all of the CH_4 spectral features. However, for very young or old planets $R > 325$ is required. With these values in mind and because follow up instruments can always measure an interesting spectrum more precisely, $R > 100$ is often cited as a reasonable detector goal for this type of instrument [23].

Detector noise constraints for direct imaging are fairly complex. Recognizing that we should try to characterize as many exoplanets as possible, one way of conceptualizing how much noise is tolerable is to model how many exoplanets we would find given a finite time interval. To achieve roughly 95 % of the exoearth detection yield of a noiseless detector in a space-based mission with $R = 50$, a dark current $<2.5 \times 10^{-4}\ \mathrm{e^-\ pixel^{-1}\ s^{-1}}$ and a read noise of $<0.1\ \mathrm{e^-\ pixel^{-1}}$ is required [24]. For higher resolving powers, the noise constraints get tighter in a conventional IFS since the light needs to be spread over more pixels to measure the energy more accurately. These strict targets come from the extremely low light levels that would reach us from an exoearth. Based on models of our optical systems and an exoearth's expected albedo, we can estimate less than one photon to arrive at our detector per pixel per minute for a space based instrument [23].

1.1.3 Commercial Detectors

Several mature detector technologies exist that are available to make an exoplanet IFS. All of these options are semiconductor based where photons promote electrons above the band gap of the material allowing the generated current to be measured. However, the process of reading out each pixel's current is not perfect, and the total number of photons absorbed cannot be determined exactly. Additionally, spectral resolution is achieved through the use of a lenslet array which disperses light across several pixels depending on the incident wavelength. To reach an $R = 50$, for example, each spectral pixel would need to contain approximately 60 physical pixels [23]. Higher resolving powers require proportionally more physical pixels.

Typically, two different semiconductor detector technologies are required for the best performance over the whole visible to near-infrared energy range. Electron-Multiplying Charge-Coupled Devices (EMCCDs) are the most mature detector for visible astronomy and, after an extensive study of tradeoffs, were chosen for the currently in development Nancy Grace Roman Space Telescope (formally known as the Wide-Field Infrared Survey Telescope or WFIRST) [25]. The current generation of EMCCDs have significant problems with radiation hardness, and in space-based operation would lose performance over the span of a typical mission [23]. They have sub-electron read noise and a dark current of $5 \times 10^{-4}\,\mathrm{e^{-}\,pixel^{-1}\,s^{-1}}$ and must be cooled to ~170 K [25].

In the near-infrared, HgCdTe detectors are the most mature and have been used on both the Hubble Space Telescope and the James Web Space Telescope. These detectors have higher read noise than EMCCDs in the range of 2 to $5\,\mathrm{e^{-}\,pixel^{-1}}$, but their dark currents are well below what is needed for exoplanet measurements [18, 19, 23]. To reach this performance, the devices must be cooled to lower temperatures, ~90 K [18, 19].

1.2 Superconducting Detectors

The semiconductor detector technologies presented in section 1.1.3 are state-of-the-art but fall short of the strict requirements for directly imaging an earth-like planet and characterizing its atmosphere. As discussed in section 1.1.2, the amount of light received from an exoearth can be quite small for those with the highest contrast ratios. The primary area of concern for semiconductor detectors, then, is the noise added to the measured photon counts. This problem is exacerbated by the standard IFS design which splits the light from one spectral pixel across many physical pixels, further reducing the photon flux and increasing the read noise.

Superconducting detectors have a natural advantage over semiconductor detectors when photon counting noise is important for an application. Like semiconductors, superconductors also have an electronic band gap which can be used to create a detector. However, the gap energies in superconductors are typically on the order of a thousand times smaller than in semiconductors. This size difference allows the photon signals in superconductors to be orders of magnitude larger. Individual photons absorbed in the superconductor can be resolved with effectively no noise. Even better, because the gap energy is so small, there is no intrinsic limitation that prevents these detectors from operating in the entire ultraviolet to near-infrared wavelength range, circumventing the need for multiple detector technologies.

Additionally, superconducting detectors are often as simple as one or two layers of metal patterned onto high quality crystalline dielectrics. This quality helps them be resistant the harsh radioactive environment of space with which semiconductor detectors struggle. Experiments at proton beam sources have shown that an equivalent 5 year radiation exposure at the Legrange L2 point has little effect on these kinds of sensors [26].

For ground-based observations, too, superconducting detectors have an advantage over semiconductor detectors. As mentioned in section 1.1.2, atmospheric speckles limit these types of observations with further improvements requiring faster detectors. As HgCdTe detectors are readout at higher speeds, they become more noisy, so they are not an option for the longer wavelengths. A true single photon counting detector, though, could be readout at much faster speeds while detecting the full ultraviolet to near-infrared range. Initial lab testing has demonstrated this type of wavefront control reaching frame rates of >30 Hz [27]. More advanced analysis techniques are also available for single photon counting detectors that help reach below the speckle noise floor [28].

In addition to the above advantages, a superconducting pixel can be energy resolving by measuring the size of the detector response made when a photon is absorbed. Unlike in semiconductor detectors, each physical pixel is then a spectral pixel. This property allows for a small array of superconducting pixels to have the same performance as a semiconductor detector array with 100 times more pixels. Mega-pixel semiconductor cameras can then be replaced with kilo-pixel superconducting cameras. Since we get perfect photon counting for free, to be truly competitive the superconducting single pixel resolving power needs to be comparable to the multi-pixel semiconductor resolving power. This parameter is the primary metric that needs to be improved in these detectors, and the rest of this dissertation addresses progress along this front.

1.2.1 Historic Examples

Superconducting thin films deposited on high quality crystalline wafers have been used as detectors since the 1940s. The first of these types of detectors were bolometers which used the dramatic change in resistance near the superconducting transition temperature to measure the power dissipated by the absorption of photons [29, 30]. These devices operate at a temperature on the transition's edge, $T \sim T_c$, and so are often called

Transition Edge Sensors (TESs). Modern versions of these detectors span a wide range of applications including measurements across the electromagnetic spectrum from millimeter waves [31] through to gamma rays [32]. In particular, single photon counting is achieved for high enough photon energies. Single photon counting TESs have been demonstrated in the ultraviolet to near-infrared range [33] with resolving powers of about 11 at 1 µm [34] and have found uses in bio-analysis research [1]. Intense interest in this technology has spurred the development of TES multiplexing readout schemes which enable arrays with several thousand pixels, at the cost of great effort and complexity [35]. The largest demonstrated TES array in the ultraviolet to near-infrared wavelength range to date, however, remains at 36 pixels [36].

The possibility of a superconducting detector operated at temperatures well below T_c was first suggested in 1961 using Superconducting Tunnel Junctions (STJs) [37]. These detectors use the tunneling current across a thin dielectric junction to measure the energy absorbed by incident radiation. STJs were developed for single photon detection in the ultraviolet to near-infrared wavelength range in the 1996 [38], and they ultimately surpassed TESs at these photon energies, reaching resolving powers of 16 at 1 µm [39]. Arrays as large as 120 pixels were developed for astronomical imaging as well [40]. Progress in recent years on STJs has waned in part because of the lack of a large supporting community to help tackle the readout complexities of large arrays. However, much of the physics used to understand superconducting detectors resulted from work done to improve STJ performance.

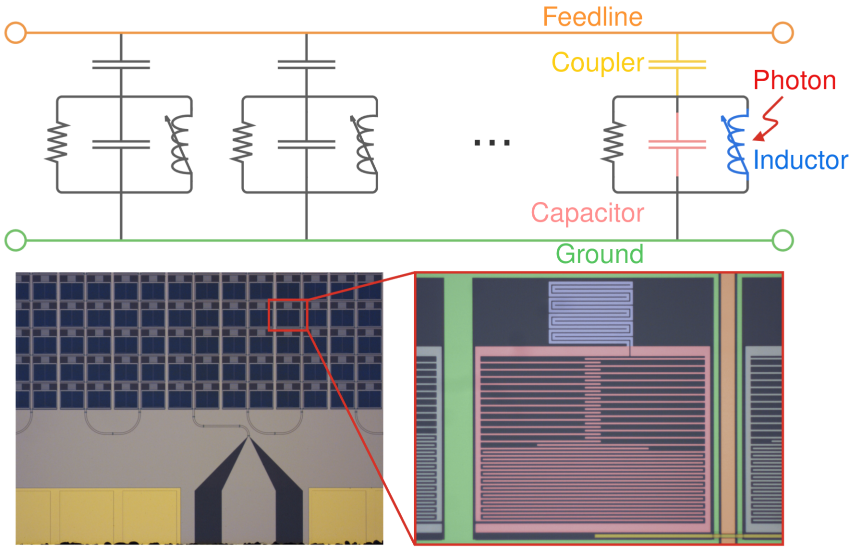

Figure 1.3: *Top:* A schematic version of an MKID array is shown. Each resonator has a different resonance frequency where it acts as a short to ground. Off resonance, the resonator does not interact with the feedline. Photons break Cooper pairs in the inductor changing its kinetic inductance. *Bottom Left:* A microscope image of a portion of an MKID array for the MEC instrument is shown. *Bottom Right:* Each pixel is a lumped element resonator. The components have been colored according to the schematic diagram above. Incident photons are focused onto each pixel's inductor.

1.2.2 Microwave Kinetic Inductance Detectors

This dissertation focuses on a different type of detector technology based on the kinetic inductance effect. The lack of resistance in a superconductor allows pairs of electrons, called Cooper pairs, to travel without scattering. Unlike in a normal conductor, these electrons can have significant momentum which presents itself as an extra inductance or reluctance to changes in velocity. The amount of inductance present is sensitive to the distribution of broken Cooper pairs, called quasiparticles. By patterning the superconductor into a microwave resonator, changes in this quasiparticle distribution caused by photon absorption can be sensitively measured [41, 42]. For this reason, we call these sensors Microwave Kinetic Inductance Detectors (MKIDs).

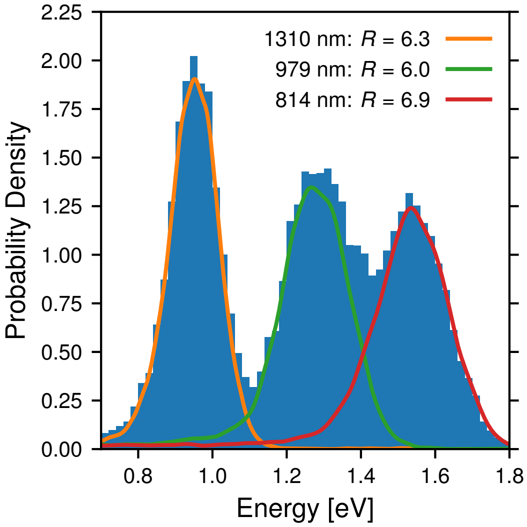

Figure 1.4: Plotted is a typical combined spectrum of three lasers with wavelengths from 1,300 to 800 nm from a PtSi$_x$ MEC device. Each laser was turned on individually, and each resulting distribution was computed with a kernel density estimate. From the distributions we measure R = 6 to 7 across this range of photon energies.

By fabricating each resonator with a different resonance frequency, detectors can be addressed simultaneously by using a superposition of probe tones. Figure 1.3 shows how this scheme allows for the readout of thousands of detectors on a single readout line. MKIDs natively solve the longstanding problem of how to easily wire and readout kilo-pixel sized arrays of superconducting detectors. As such, they have a dynamic community of scientists dedicated to improving them and fashioning them into instruments. By 2016, single photon counting MKIDs in the ultraviolet to near-infrared range had been demonstrated using TiN$_x$ and PtSi$_x$ and achieved resolving powers which varied from 4 to 7 at 1 µm in arrays of up to 20,000 pixels [43, 44]. Three astronomical instruments have been made using this technology to date: the Array Camera for Optical to Near-IR Spectrophotometry (ARCONS) [45], the DARK-speckle Near-infrared Energy-resolving Superconducting Spectrophotometer (DARKNESS) [46], and the MKID Exoplanet Camera (MEC) [47].

Figure 1.4 shows a measurement of a three laser spectrum with one of these devices. These results show that as of 2016 MKIDs still underperformed with respect to TESs and STJs and needed to do much better to be useful for a competitive exoplanet IFS. The rest of this dissertation will focus on the improvements made to the MKID resolving power in the six years after 2016, which occurred in parallel to the instrumentation and readout developments for DARKNESS and MEC.

2

MKID Physics

MKIDs display a rich variety of condensed matter physics, electrodynamics, and enable sensitive probes of several different material properties. As such, this chapter aims to bring the major theoretical developments important to MKIDs into focus by highlighting results in the field of superconductivity and micro-resonator analysis. However, a complete description of this type of physical system could fill a book, so we limit ourselves to the most important findings relevant for understanding the results presented in the rest of this dissertation.

2.1 Superconductivity

The first successful theoretical description of superconductors came from from the seminal 1957 work by Bardeen, Cooper, and Schrieffer [48]. The lack of resistance at low temperatures in these materials was explained by the introduction of an attractive potential between electrons which binds them into what are often referred to as Cooper pairs.

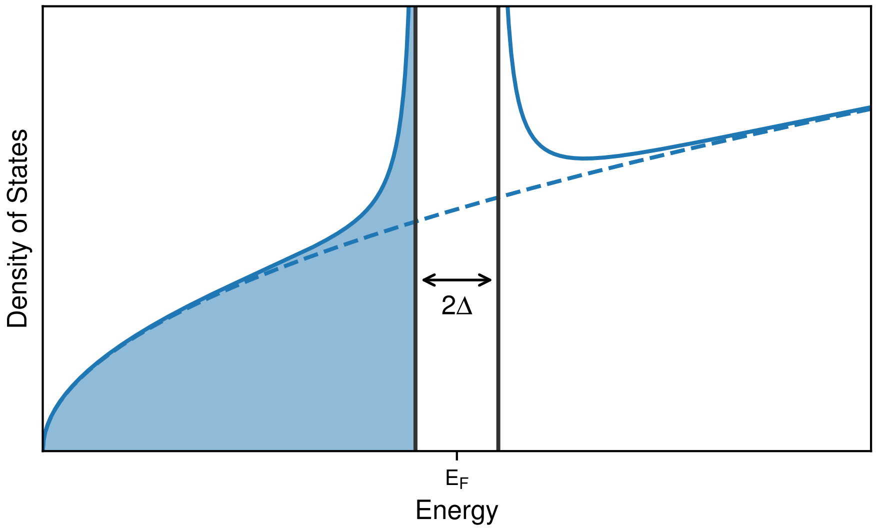

Figure 2.1: At low temperatures the electron density of states of a superconductor develops a gap around the Fermi energy, E_F (solid line). At zero temperature, all electrons have energies in the filled in region and can not flow as current. At higher temperatures the gap, Δ, gets smaller until it disappears (dashed line). The relative scales of Δ, E_F, and the background density of states are exaggerated for clarity.

The density of states of the remaining electrons develops an energy gap where no states are allowed. This gap prevents small energy perturbations from scattering the electrons as they would in a normal metal. Ultimately, the lack of scattering is what is responsible for the zero resistance characteristic of superconductivity. Figure 2.1 shows a schematic picture of this temperature dependent energy gap, $\Delta(T)$.

The Bardeen, Cooper, and Schrieffer theory of superconductivity (BCS) described the effects of an appropriately sized attractive potential on a metal at low temperatures and suggested that it originated from the interaction between electrons and quantized lattice vibrations, also known as phonons. However, a detailed, quantitative microscopic picture of how this interaction works was absent until the 1960 development by Éliashberg [49]. The theory gives a set of equations which can be solved for a renormalization function, $Z(E,T)$, and an order parameter $\Delta(E,T)$. These two functions can then be used to calculate the physical properties of a superconducting system at a given energy, E, and temperature, T. In this theory, Δ gains an energy dependence and can be complex which removes the unphysical singularity in the BCS density of states. However, in many cases the BCS theory is used for calculations anyways as it is simpler, and the Éliashberg result often can be found simply by multiplying the BCS result by the renormalization function at zero energy and the transition temperature, $Z(0, T_c) = 1 + \lambda$ [50]. Here λ is the electron-phonon coupling constant which takes into account the phonon density of states and the interaction matrix element. Typically, λ must be measured for a given superconductor but can also be found in tables for many common materials [51].

2.1.1 Density of States and Pairs

The density of states presented in figure 2.1 represents the states available to unpaired electrons. Only those unpaired electrons with energies above the Fermi energy, E_F, can carry current. These electrons are typically called quasiparticles since they still behave like particles but move as if they have a different mass because the complex interactions between the other electrons and nuclei. The introduction of a gap in the density of states turns the superconductor into an insulator with respect to these unpaired electrons. At zero temperature, then, all of the current in a superconductor is carried by the Cooper pairs which have their own density function. We can calculate these density of state functions from the complex Éliashberg order parameter that reduces to the gap energy in the BCS case.

First, we introduce several complex functions that will be useful for calculations.

$$n(\epsilon, T) = \frac{\epsilon}{\sqrt{\epsilon^2 - \Delta(\epsilon, T)^2}} \tag{2.1a}$$

$$p(\epsilon, T) = \frac{\Delta(\epsilon, T)}{\sqrt{\epsilon^2 - \Delta(\epsilon, T)^2}} \tag{2.1b}$$

$$\tan\theta(\epsilon, T) = \frac{i\Delta(\epsilon, T)}{\epsilon} \tag{2.1c}$$

We have written these functions with respect to the Fermi energy, $\epsilon = E - E_F$, and care needs to be taken to choose the branch of the square root in these functions with a positive imaginary part. $\theta(\epsilon, T)$ is often referred to as the pairing angle.

The density of states for quasiparticles is then given by

$$\begin{aligned} N(\epsilon, T) &= N_0 \mathrm{Re}[n(\epsilon, T)] \\ &= N_0 \mathrm{Re}[\cos\theta(\epsilon, T)] \end{aligned} \tag{2.2}$$

where N_0 is the single spin density of states at the Fermi energy which we assume to be independent of energy on the scale of the gap [52]. A similar expression exists for Cooper pairs:

$$\begin{aligned} P(\epsilon, T) &= \mathrm{Re}[p(\epsilon, T)] \\ &= \mathrm{Im}[\sin\theta(\epsilon, T)]. \end{aligned} \tag{2.3}$$

However, $P(\epsilon, T)$ more accurately represents a pairing amplitude as the formula for the

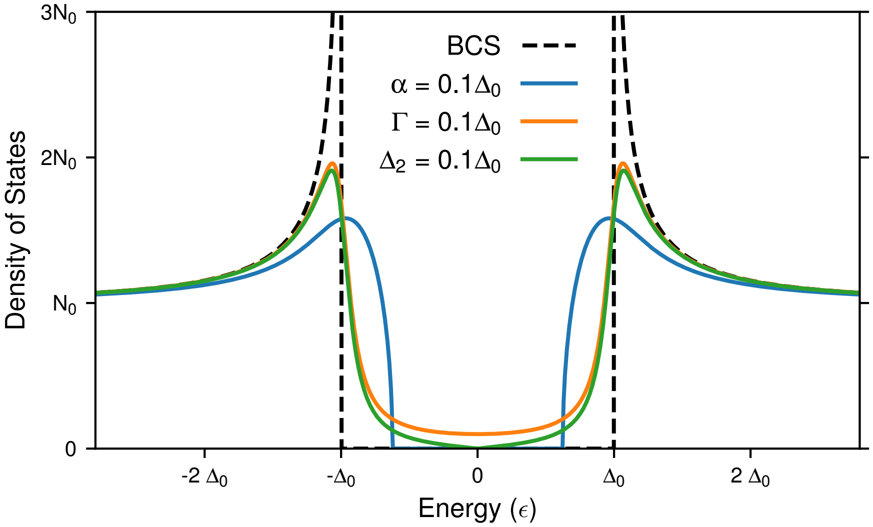

Figure 2.2: The superconducting density of states is plotted near the Fermi energy for several different types of gap broadening described in the text. Here, Δ_0 corresponds to gap energy that would exist if no broadening mechanism existed. The BCS density of states is shown for comparison.

supercurrent density is weighted against [53]

$$\begin{aligned}\tilde{P}(\epsilon, T) &= -\mathrm{Im}\left[p(\epsilon, T)^2\right] \\ &= \mathrm{Im}\left[\sin^2\theta(\epsilon, T)\right].\end{aligned} \tag{2.4}$$

In the BCS case, where $\Delta(T)$ is independent of energy, $\tilde{P}(\epsilon, T) = \frac{\pi\Delta(T)}{2}[\delta(\epsilon - \Delta(T)) - \delta(\epsilon + \Delta(T))]$ which shows all of the current is contained in the small energy region bordering the gap energy.

2.1.2 Gap Broadening

The BCS density of states has singularities at the borders of the gap region. These singularities do not exist in real superconductors as the phonon interactions worked out by Éliashberg turn them into narrow peaks with a finite height. In practice, though, many superconductors exhibit much more broadening of these peaks than expected, and this broadening seems to scale with disorder in the material. Early attempts to explain the discrepancy involved invoking magnetic impurities which were shown to suppress the gap energy and add sub-gap states [54]. However, those equations are complicated and do not always accurately describe the density of states. Here we list three of the simplest and most used parameterizations for $\Delta(\epsilon)$ to broaden the superconducting gap and discuss their physical mechanisms.

One of the most commonly used approximations for gap broadening in the density of states is the Dynes formula [55]. This formula can be derived directly from the Éliashberg formalism as a result of inelastic, pair-breaking electron-phonon scattering [56]. However, this explanation does not always describe the observed temperature dependance of the scattering parameter, $\Gamma(T)$. An alternative explanation is disorder induced pair-breaking scattering which results in a temperature independent Γ [57]. The Dynes formula for density of states can be derived by setting

$$\Delta(\epsilon, T) = \frac{\epsilon \bar{\Delta}(T)}{\epsilon + i\Gamma(T)}, \tag{2.5}$$

where $\bar{\Delta}(T)$ is the effective gap size.

Another approach for explaining a broadened density of states comes from the theory of nonequilibrium superconductivity based on Green's functions [58]. For dirty superconductors, where the mean free path is smaller than the coherence length and the penetration depth, this theory can be simplified into the Usadel equations [59]. In the limit of a spatially uniform superconductor the Usadel equations reduce to

$$\Delta(T)\cos\theta(\epsilon,T) + i\epsilon\sin\theta(\epsilon,T) - \alpha\sin\theta(\epsilon,T)\cos\theta(\epsilon,T) = 0, \tag{2.6}$$

where α represents a constant elastic spin-flip scattering on magnetic impurities. Here, Δ is independent of energy and is real. This equation replaces equation 2.1c for the pairing angle. Δ can be solved by moving to the Matsubara representation, $\epsilon \to i\epsilon_n = (2n + 1)i\pi k_B T$, and using the additional self consistency equation:

$$\Delta(T) = \frac{2\pi k_B}{\log\left({}^{T}\!/\!_{T_c}\right) + \psi(n_c + {}^{3}\!/\!_{2}) - \psi({}^{1}\!/\!_{2})} \sum_{n=0}^{n_c} \sin\theta(i\epsilon_n, T). \tag{2.7}$$

$\psi(x)$ is the digamma function and $n_c = \lfloor {}^{\Theta_D}\!/\!_{2\pi T} - {}^{1}\!/\!_{2} \rfloor$ is a cutoff imposed by the Debye temperature, Θ_D [60, 61]. The pair angle can then be solved for at the real energies by plugging $\Delta(T)$ back into equation 2.6.

Finally, and perhaps most simply, the order parameter may be taken to be a constant complex number.

$$\Delta(T) = \Delta_1(T) - i\Delta_2(T) \tag{2.8}$$

It can be shown that $\Delta_2(T)$ corresponds to a non-zero quasiparticle decay rate which is a characteristic of all superconductors [62, 63].

These three formalisms for broadening the superconducting gap are all based on different physical mechanisms. Figure 2.2 shows how each changes the density of states in a different way. However, in an actual superconductor, more than one of these mechanisms may be present, including ones not listed here. Thankfully, the density of states and pairs are often used to compute parameters of interest by integrating them over all energies as weighting functions. This procedure tends to be forgiving with respect to slight differences in how the broadening is determined. For cases like these where no measurement of the density of states exists, historically, one broadening model is chosen usually without much justification [64–67].

2.1.3 Proximity Effect

When a superconductor is placed in contact with another superconductor or metal, the Cooper pairs are able to interact with the electrons in the other material. In effect, superconductivity extends into neighboring metals by a length, $\sqrt{\hbar D / k_B T}$, where T is the temperature and D is the normal metal diffusion constant [53]. This phenomenon is called the proximity effect, and it can have important consequences for superconducting circuits like MKIDs. The primary tool used to understand the proximity effect is the theory of nonequilibrium superconductivity discussed in section 2.1.2 [58]. For thin films, scattering at the interfaces ensures that the dirty superconducting limit is valid, and the equations reduce to the Usadel formalism [68].

For stacked multilayer films, the pair angle and order parameter become a function of vertical position, z. A procedure exists to calculate them after which other material properties can be determined [69]. The Usadel equation becomes a set of differential equations.

$$\frac{\hbar D_i}{2}\frac{\partial^2 \theta_i}{\partial z^2} + \Delta_i(T, z)\cos\theta_i(\epsilon, T, z) + i\epsilon \sin\theta_i(\epsilon, T, z) - \alpha_i \sin\theta_i(\epsilon, T, z)\cos\theta_i(\epsilon, T, z) = 0 \tag{2.9}$$

The subscript i refers to the different material layers, and we have included the gap broadening term, α, from section 2.1.2. These equations are coupled by boundary conditions which enforce the conservation of spectral current. At an i/j layer boundary

$$\sigma_i \frac{\partial \theta_i}{\partial z} = \sigma_j \frac{\partial \theta_j}{\partial z} = \frac{G_{\text{int}}}{A} \sin\left(\theta_i - \theta_j\right), \tag{2.10}$$

where $\sigma_{i,j}$ are the normal state conductivities and $^{G_{\text{int}}}/_{A}$ is the interface conductance per area. At the two free interfaces in the multilayer $G_{\text{int}} = 0$. Equation 2.9 is solved in the same way as equation 2.6 by transforming to the Matsubara energies and using the self consistency equation for the gap defined in equation 2.7.

2.2 Superconducting Resonators

Superconducting resonators are the basis of several important emerging technologies, including the readout of superconducting quantum computing circuits now being developed in industry and academia [70] and sensitive photon detector arrays for astronomy (MKIDs) [41]. These devices are typically optimized for extremely low loss at frequencies in the microwave regime. When a photon of energy E_{photon} gets absorbed in the superconductor, it breaks Cooper pairs and creates a non-equilibrium distribution of quasiparticles. The excess quasiparticle density is given by

$$\delta n_{\text{qp}} = \frac{\eta_{\text{pb}} E_{\text{photon}}}{V \Delta}. \tag{2.11}$$

V is the superconductor volume. $\eta_{\text{pb}} \sim 0.59$ is the Cooper pair breaking efficiency and is roughly constant across all superconductors [71]. Here we will present a model which allows us to relate this change in the quasiparticle density in the inductor of our resonator caused by E_{photon} to the voltage signals that we measure with our readout electronics.

2.2.1 Quasiparticle Density

The thermal density of quasiparticles in a superconductor is given by

$$n_{\text{qp}}(T) = 4 \int_0^\infty N(\epsilon, T) F(\epsilon, T) d\epsilon \tag{2.12}$$

where $F(\epsilon, T) = \left[1 + e^{\epsilon / k_B T}\right]^{-1}$ is the Fermi-Dirac thermal distribution function. For the BCS case and $T \ll T_c$, the quasiparticle density can be approximated by [72, 73]

$$n_{\text{qp}}(T) = 2N_0 \sqrt{2\pi\Delta(T) k_B T} e^{-\frac{\Delta(T)}{k_B T}}. \tag{2.13}$$

The quasiparticle density should be exponentially suppressed at low temperatures. However, in practice, $n_{\text{qp}}(T)$ approaches a constant value as $T \rightarrow 0$ [74–77]. The source of this discrepancy is still up for debate and is likely system dependent. Often a number of potential sources are cited as the origin of these excess quasiparticles [77–82]. The use of the thermal distribution function in equation 2.13 is also probably incorrect. Heating from the readout tone may drive the quasiparticle population out of thermal equilibrium for example [80]. However, although the thermal distribution function may not be strictly appropriate, it is often used in place of a more complex analysis and gives quantitatively accurate results anyways [42].

Whatever the source, the bottleneck in the recombination of these quasiparticles is their accompanying background distribution of phonons and the phonon escape time into the substrate [83]. This feature lends itself to the simple model where the quasiparticle temperature is decoupled from the phonon temperature and has been useful in modeling the response of Thermal Kinetic Inductance Detectors (TKIDs) [73, 84, 85]. For non-thermal sensors like MKIDs, this model has also been shown to be applicable to the non-equilibrium creation of quasiparticles by a photon signal, which allows us to use it in this dissertation [86].

2.2.2 Complex Conductivity

To understand how the change in quasiparticle density, δn_{qp}, effects the resonator, we need to introduce the complex conductivity, σ. The imaginary part of σ comes from the large inertia of the Cooper pairs. Mattis and Bardeen [87] first worked out the equations for σ in the case of a BCS superconductor. These equations were later generalized by Nam [52] for both clean and dirty Éliashberg superconductors. If we define $\sigma/\sigma_N = \sigma_1 - i\sigma_2$, where σ_N is the normal state conductivity, in the notation used in section 2.1.1 at frequency f we have [88]

$$\sigma_1(f,T) = \frac{1}{hf}\int_{-\infty}^{\infty} d\epsilon [F(\epsilon,T) - F(\epsilon+hf,T)] \tag{2.14a}$$

$$\times \left[\mathrm{Re}[n(\epsilon,T)]\mathrm{Re}[n(\epsilon+hf,T)] + \mathrm{Re}[p(\epsilon,T)]\mathrm{Re}[p(\epsilon+hf,T)]\right]$$

$$\sigma_2(f,T) = \frac{-1}{hf}\int_{-\infty}^{\infty} d\epsilon [1 - 2F(\epsilon,T)] \tag{2.14b}$$

$$\times \left[\mathrm{Re}[n(\epsilon)]\mathrm{Im}[n(\epsilon+hf)] + \mathrm{Re}[p(\epsilon)]\mathrm{Im}[p(\epsilon+hf)]\right]$$

Initial attempts at determining how the complex conductivity should change when the quasiparticle density increases used a model developed by Owen and Scalapino [89]. Quasiparticles are assumed to be in thermal equilibrium with the phonons but not in chemical equilibrium with the pair state. These results gave good agreement with measurements of superconducting resonators [90]. However, the theory fails to predict the correct relationship between the gap energy and excess quasiparticle density [91, 92]. A more physical model uses the effective quasiparticle temperature introduced in section 2.2.1. We solve

$$\delta n_{\mathrm{qp}} = n_{\mathrm{qp}}(T^*) - n_{\mathrm{qp}}(T) = 4\int_0^{\infty} [N(\epsilon,T^*)F(\epsilon,T^*) - N(\epsilon,T)F(\epsilon,T)]d\epsilon \tag{2.15}$$

for the effective temperature, T^*, where the temperature, T, may or may not be the system temperature depending on if the quasiparticle density has saturated. With T^* and keeping in mind that the device is being readout at the signal generator's frequency, f_g, the change in the complex conductivity can be calculated.

$$\delta\sigma(\delta n_{\mathrm{qp}}) = \sigma(f_g, T^*) - \sigma(f_g, T) \tag{2.16}$$

2.2.3 Surface Impedance

The surface impedance of the resonator is ultimately the material parameter that we use to compute the resonance properties. Just like the complex conductivity it has a real and imaginary part: $Z_s = R_s + iX_s$. The real part is nonzero but exponentially suppressed at low temperatures since superconductors do have a finite amount loss for time varying signals. The imaginary part, $X_s = 2\pi f L_s$, is related to the surface inductance of the material. It is important to point out that the surface impedance does not necessarily equal the total impedance of the film. Instead, it is related to the total impedance based on two geometric parameters, $g = {}^{\alpha L}/_{L_s} = {}^{R}/_{R_s}$, which relates the dissipation and energy stored inside the superconductor to the surface impedance, and the kinetic inductance fraction, $\alpha = {}^{L_k}/_{L}$, which takes into account the magnetic field contribution to the total inductance outside the superconductor [93]. L_k is the kinetic inductance of the superconductor and is a film constant.

$$R + 2\pi i f L = g\left[R_s + \frac{2\pi i f}{\alpha} L_s\right] \tag{2.17}$$

Depending on the superconducting limit, the surface impedance has a different proportionality relationship with the complex conductivity [93, 94].

$$Z_s \propto \sigma^{-\gamma} \tag{2.18}$$

γ is either 1, 1/2, or 1/3 for the thin-film, dirty, and extreme anomalous limits, respectively. This relationship allows us to write

$$\frac{\delta Z_s(\delta n_{\mathrm{qp}})}{Z_s(f,T)} = \left(1 + \frac{\delta\sigma(\delta n_{\mathrm{qp}})}{\sigma(f,T)}\right)^{-\gamma} - 1 \tag{2.19}$$

where $\delta Z_s(\delta n_{\mathrm{qp}}) = Z_s(f,T^*) - Z_s(f,T)$. For small changes, this formula is often rewritten as

$$\frac{\delta Z_s(\delta n_{\mathrm{qp}})}{Z_s(f,T)} \approx -\gamma \frac{\delta\sigma(\delta n_{\mathrm{qp}})}{\sigma(f,T)}. \tag{2.20}$$

If the superconductor is in the dirty limit, but not thick or thin enough to set $\gamma = 1$ or 1/2, $Z_s(f,T)$ can be computed directly from $\sigma(f,T)$ using a transmission line model [69, 95].

2.2.4 Resonance Model

As microwaves pass through our resonator, they are either scattered back toward the signal generator or are transmitted through to the amplifiers. The information about the resonance is encoded the resulting scattering matrix. In particular, we use the forward scattering matrix element, S_{21}, to relate the incident voltage wave to the outgoing voltage wave [96]. The outgoing voltage wave is then down-converted to the frequency range surrounding the original tone at a frequency f_g using the homodyne scheme shown in figure 2.3.

The forward scattering matrix element for an MKID can be described by the following

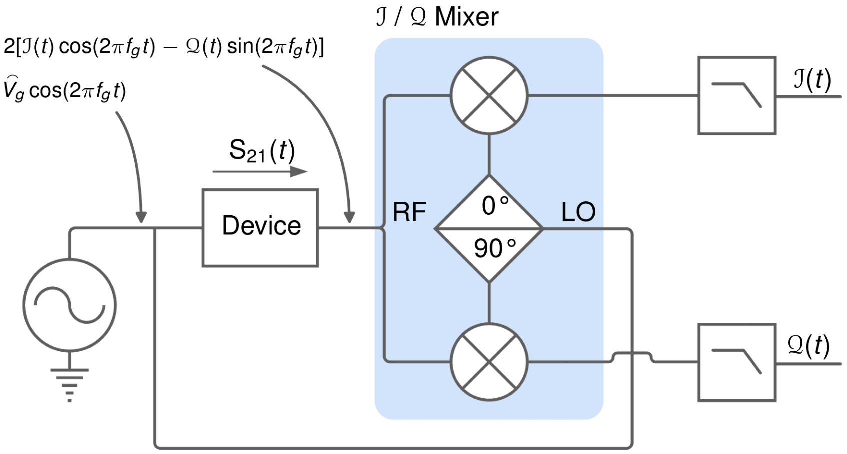

Figure 2.3: MKIDs typically use the homodyne readout scheme, depicted here, to extract slow changes in the forward scattering parameter, S_{21}. The $\mathcal{I}$ / $\mathcal{Q}$ mixer, highlighted in blue, contains two individual mixers which each multiply the signal coming from the device by a copy of the original. The $\mathcal{Q}$ channel is phase shifted by 90° before the multiplication. Low pass filters are included after the $\mathcal{I}$ / $\mathcal{Q}$ mixer to remove frequency components near $2f_g$. In this schematic, the "device" includes the MKID as well as any attenuators and amplifiers in the readout chain between the mixer and signal generator.

equation derived in appendix B.1 [97–99].

$$S_{21} = \left(g_0 + g_1 x_m + g_2 x_m^2\right) e^{i(\phi_0 + \phi_1 x_m)} \frac{Q_c + 2iQ_iQ_c(x_n + x_a)}{Q_i + Q_c + 2iQ_iQ_cx_n} \tag{2.21}$$

$$S_{21} = \left(g_0 + g_1 x_m + g_2 x_m^2\right) e^{i(\phi_0 + \phi_1 x_m)} \bar{S}_{21} \tag{2.22}$$

The normalized forward scattering matrix element, $\bar{S}_{21}$, contains all the information about the resonator properties since the gain, $\{\, g_i \,\}$, and phase, $\{\, \phi_i \,\}$, pre-factors do not depend on the resonance itself. The parameters in Equation 2.21 are defined in detail in appendix B.1, but the most important are the nonlinear fractional frequency detuning, x_n, which represents how far the generator frequency is from the resonance frequency; the asymmetry fractional frequency detuning, x_a, which represents how much the resonance frequency is perturbed due to impedance mismatches; the coupling quality factor, Q_c, which represents how weakly the resonator is coupled to the transmission line; and the internal quality factor, Q_i, which represents how little loss there is in the resonator.

The nonlinear fractional frequency detuning is a result of the quadratic dependence of the kinetic inductance on current density. At high readout powers this term causes the resonance to bifurcate and become multivalued. In appendix B.2 it is shown that x_n is implicitly related to the fractional generator detuning parameter, $x_g = {}^{(f_g - f_r)}/_{f_r}$, by [100]

$$Qx_n = Qx_g + \frac{a}{1 + 4Q^2 x_n^2}. \tag{2.23}$$

f_r is the resonance frequency and a is a constant describing how close the resonance is to bifurcating due to the nonlinearity. Equation 2.23 must be solved first before using x_n in equation 2.21.

However, we don't measure S_{21} directly but only through the $\mathcal{I}$ and $\mathcal{Q}$ mixer values. In appendix B.3, we show that when the system is in equilibrium $S_{21} = \mathcal{Z} = \mathcal{I} + \mathcal{Q}$, so we define the normalized $\bar{\mathcal{I}}$ and $\bar{\mathcal{Q}}$ signals as before.

$$\begin{aligned} \mathcal{Z} &= \left(g_0 + g_1 x_m + g_2 x_m^2\right) e^{i(\phi_0 + \phi_1 x_m)} \bar{\mathcal{Z}} \\ \mathcal{I} + i\mathcal{Q} &= \left(g_0 + g_1 x_m + g_2 x_m^2\right) e^{i(\phi_0 + \phi_1 x_m)} \left(\bar{\mathcal{I}} + i\bar{\mathcal{Q}}\right) \end{aligned} \tag{2.24}$$

Immediately after a photon is absorbed in the resonator, both the inductance and the resistance of the material increase from the excess quasiparticles. We relate these changes to changes the resonance frequency, f_r, and the internal quality factor, Q_i [93].

$$\frac{\delta f_r}{f_r} = -\frac{1}{2}\frac{\delta L}{L} = -\frac{\alpha}{2}\frac{\delta L_k}{L_k} = -\frac{\alpha}{2}\frac{\delta X_s}{X_s} \tag{2.25a}$$

$$\delta Q_i^{-1} = \frac{\delta R}{2\pi f_g L} = \alpha\frac{\delta R_s}{X_s} \tag{2.25b}$$

This event causes the forward scattering matrix element to change and become time dependent: $S_{21} \longrightarrow S_{21} + \delta S_{21}(t)$. In appendix B.4, we show that $\mathcal{I}$ and $\mathcal{Q}$ change accordingly with a slightly different frequency response [42, 73, 93].

$$\widetilde{\delta\mathcal{Z}}(f) = \frac{1 - \bar{S}_{21}(f_g + f)}{1 - \bar{S}_{21}(f_g)}\,\widetilde{\delta S}_{21}(f) \tag{2.26}$$

When $f_g = f_r$,

$$\widetilde{\delta\mathcal{Z}}(f) = \frac{1}{1 + {}^{2iQf}/_{f_r}}\widetilde{\delta S}_{21}(f). \tag{2.27}$$

This equation simply shows that the change in the forward scattering matrix element is low pass filtered with a cutoff frequency of ${}^{f_r}/_{2Q}$. The ring-up time for the resonator, which is the timescale at which we measure the resonator responding to changes, is then

$$\tau_{\text{res}} = \frac{Q}{\pi f_r}. \tag{2.28}$$

τ_{res} must be much less than the quasiparticle lifetime to ensure that the photon response is measurable.

3

Data Analysis

3.1 Phase and Dissipation Coordinates

Tracking the photon signals $^{\delta f_r}/_{f_r}$ and δQ_i^{-1} from chapter 2 in real-time requires complex algorithms and hardware. Moreover, these systems typically do not have the required bandwidth to readout single photon detectors. [35] Instead, the homodyne readout scheme from figure 2.3 is typically used to down-convert the detector response to a finite bandwidth around each readout tone, resulting in an in-phase, $\mathcal{I}$, and quadrature, $\mathcal{Q}$, signal from a mixer. In the adiabatic case, where changes to $\mathcal{I}$ and $\mathcal{Q}$ occur at frequencies $f \ll {}^{f_r}/_{2Q}$, and after calibrating out effects from amplification and cabling, $\bar{\mathcal{Z}} = \bar{\mathcal{I}} + i\bar{\mathcal{Q}}$ is equal to the forward scattering matrix element of the resonator (see appendix B.3).

3.1.1 Coordinate Definition

When analyzing photon events, $\bar{\mathcal{I}}(t)$ and $\bar{\mathcal{Q}}(t)$ are often transformed into a polar coordinate system, referenced to the loop center and radius. Mathematically, they are repre-

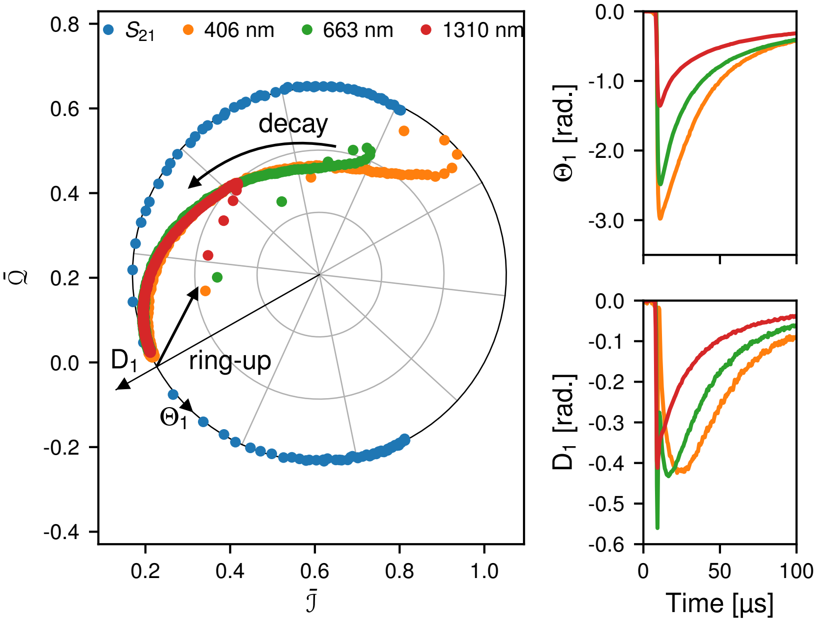

Figure 3.1: The coordinate system used to analyze data is shown with respect to a hafnium MKID, described in detail in reference 67. Averaged response trajectories for three different photon energies are plotted in the $\mathcal{I}$ / $\mathcal{Q}$ plane. Their dependence on time are also shown to the right of the main plot. The Θ_1 and D_1 coordinates work for the smallest response but do not appropriately decompose the larger signals into components that scale with the photon energy.

sented by the following equations:

$$\Theta_1(t) \equiv \arg\left[\frac{1 - \bar{\mathcal{Z}}(t) - {}^{Q}\!/_{2Q_c} + iQx_a}{1 - \bar{S}_{21}(f_g) - {}^{Q}\!/_{2Q_c} + iQx_a}\right] \tag{3.1a}$$

$$D_1(t) \equiv \frac{\left|1 - \bar{\mathcal{Z}}(t) - {}^{Q}\!/_{2Q_c} + iQx_a\right|}{\left|{}^{Q}\!/_{2Q_c} - iQx_a\right|} - 1 \tag{3.1b}$$

Figure 3.1 shows these coordinates with respect to $\bar{S}_{21}$ and an example photon response trajectory.

3.1.2 Small Signal Limit

Θ_1 and D_1 are commonly referred to as phase and dissipation coordinates since in the adiabatic limit they are proportional to the fractional detuning and dissipation perturbations. We can see this by setting $\bar{\mathcal{Z}}(t) = \bar{S}_{21}$ in equations 3.1a and 3.1b where we make the substitutions $x_n \longrightarrow x_n + \delta x_n(t)$ and $Q_i^{-1} \longrightarrow Q_i^{-1} + \delta Q_i^{-1}(t)$ in equation 2.21 for $\bar{S}_{21}$. To first order in the small signals this approximation gives

$$\Theta_1(t) \approx \frac{-4Q}{1 + 4Q^2 x_n^2}\, \delta x_n(t) \tag{3.2a}$$

$$D_1(t) \approx \frac{-2Q}{1 + 4Q^2 x_n^2}\, \delta Q_i^{-1}(t) \tag{3.2b}$$

Note that the parameters x_n and Q are the fit parameters from the original fit to S_{21} and are constant.

However, $\delta x_n(t)$ is not necessarily proportional to ${}^{\delta f_r(t)}/{}_{f_r}$ in this limit since changes to the internal quality factor must be accounted for in the inductive nonlinearity equation 2.23 [42, 100].

$$\delta x_n(t) \approx \frac{-1}{1 + {}^{8aQx_n}/{}_{\left(1+4Q^2x_n^2\right)^2}} \left[\frac{\delta f_r(t)}{f_r} + \frac{2a}{\left(1 + 4Q^2 x_n^2\right)^2} \delta Q_i^{-1}(t)\right] \tag{3.3}$$

Additionally, for larger signals, equations 3.1a and 3.1b are not even close to proportional to ${}^{\delta f_r}/{}_{f_r}$ and δQ_i^{-1}. As can be seen in figure 3.1, the signals mix and saturate as the resonance frequency moves further away from f_g. Even worse, D_1 is not monotonic as a function of δQ_i^{-1}.

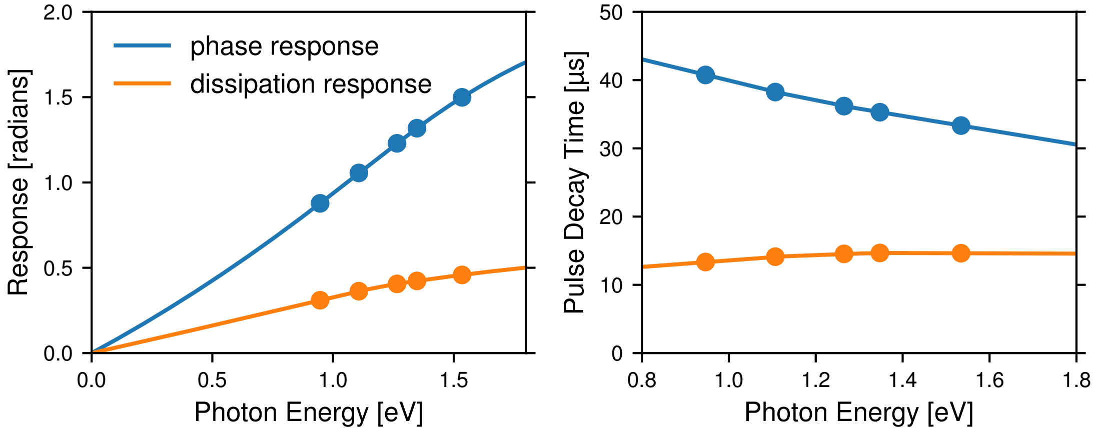

Figure 3.2: *Left:* A PtSi$_x$ detector's phase and dissipation calibration functions are shown, $A_i(E)$. Solid lines correspond to the interpolation constructed from the known energies (shown as points). *Right:* The pulse shape decay time as a function of energy is shown. The decay time here is defined as the integrated area under the normalized pulse shape. For the solid lines, the decay is computed using an interpolated pulse shape.

3.2 Photon Energy Estimation

In principle, the nonideal behavior of the coordinates for large signals or significant inductive nonlinearities can be accounted for by properly modeling the detector response and noise. Our signal in both the phase and dissipation coordinates resembles that of a standard X-ray calorimeter response, so much of the following formalism is adapted from these corresponding techniques generalized to this two-dimensional case [101–103].

3.2.1 Response Model

In an ideal detector, events with the same absorbed energy, E, should have identical detector responses. We model this response as an energy dependent, normalized pulse shape, $s_i(t, E)$, and amplitude, $A_i(E)$, where $i \in \{\theta, d\}$ corresponds to either the phase or dissipation response. In practice, we also don't know the photon arrival time, t_0, or the DC offset of each component, δ_i, ahead of the measurement so they are included as unknown parameters.

$$\vec{m}\left(t;\vec{\xi}\right) = \begin{pmatrix} A_\theta(E)\ s_\theta(t - t_0, E) + \delta_\theta \\ A_d(E)\ s_d(t - t_0, E) + \delta_d \end{pmatrix} \tag{3.4}$$

Even if there is no DC offset, since we can only measure data in finite time intervals, δ_i still needs to be included as a parameter to model noise at frequencies below the dataset's bandwidth. For brevity, we use $\vec{\xi}$ to denote all of the parameters in the model.

The amplitude and shape are separated because the pulse shape is typically only weakly dependent on energy. $A_i(E)$ is also a good indicator of detector linearity. In practice, it is not possible to know these functions over a continuous range of energies, but they can be approximated by averaging many pulse records together for a discrete set of known photon energies. As long as the number of pulse records is large, this averaging procedure gives us noise free estimates of the detector response.

An example amplitude calibration for a $\mathrm{PtSi_x}$ detector is shown in the left of figure 3.2. The detector is linear up to the highest energies tested where saturation effects begin to flatten the response. The pulse decay time is defined as the integrated area under the normalized pulse shape and is shown as a function of energy on the right of figure 3.2. This definition is adopted for it's simplicity and because the pulse shapes do not fit well to an exponential function. The pulse shapes for each energy are plotted in figure 3.3.

By using equation 3.4, we are ignoring the possibility that there may be many different responses for a given energy. In MKIDs the most common cause of this effect is from a nonuniform detector current or from phonon losses, both of which result in an unavoid-

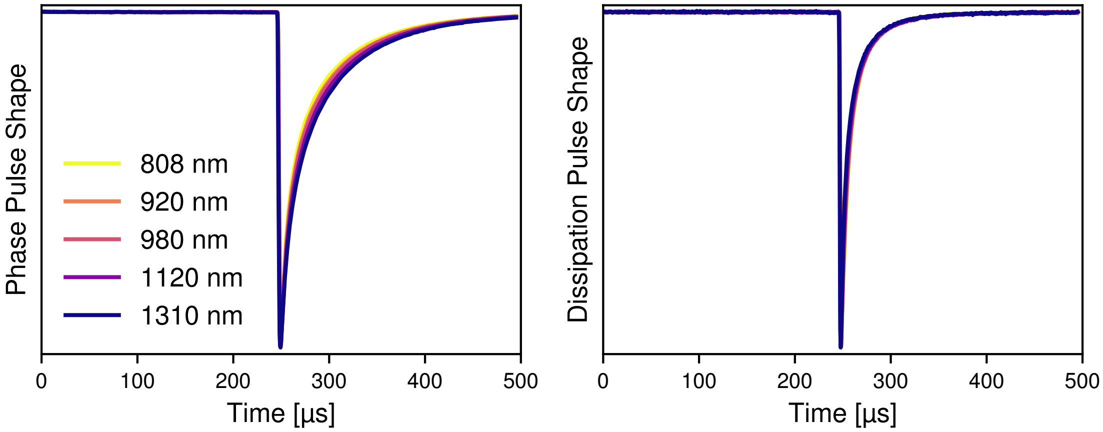

Figure 3.3: The pulse shapes, $s_i(t, E)$ of a $PtSi_x$ detector for various photon energies are shown for the phase response (left) and dissipation response (right). Both shapes are normalized so that the peak height is 1. The majority of the energy dependence for this detector occurs in the phase signal.

able degradation of the detector's resolving power [104, 105]. Since these effects cannot be easily addressed by any analysis technique we do not consider them further in this chapter. Systematic errors like gain and response drifts can also invalidate this model. However, since these variations can be corrected for when they exist [106] and are not present in the data discussed in this dissertation, they are, likewise, not considered here.

3.2.2 Noise Model

Real photon data does not follow the description laid out in section 3.2.1 exactly. All data has some noise associated with it. This noise typically comes from the attenuators, amplifiers, and two-level systems in the detector itself. To incorporate noise into our model of the data, we assume that it is additive, drawn from a gaussian distribution, and stationary. None of these assumptions are strictly true, but they work reasonably well under a wide range of conditions. More comprehensive noise models are possible and may lead to better energy estimations. With these considerations, our data looks like

$$\vec{d}\left(t;\vec{\xi}\right) = \vec{m}\left(t;\vec{\xi}\right) + \vec{n}(t), \tag{3.5}$$

where $\vec{n}(t)$ is a particular realization of the noise described by a zero-mean, 2D Gaussian random variable $\vec{N}(t)$ with an autocovariance function $\mathbf{C}(t,t') = \mathrm{Cov}\left[\vec{N}(t),\vec{N}(t')\right]$. We often assume the noise is stationary, so we can write $\mathbf{C}(t,t') = \bar{\mathbf{C}}(|t-t'|)$. In this case, typically, the Power Spectral Density (PSD) is measured instead of the autocovariance function. These two descriptions of the noise are related by the Fourier transform. For our 2D data,

$$\begin{aligned}\mathbf{S}(f) =& \mathcal{F}_t\left[\bar{\mathbf{C}}(t)\right](f)\\ =& \begin{pmatrix} S_{\theta\theta}(f) & S_{\theta d}(f) \\ S^*_{\theta d}(f) & S_{dd}(f)\end{pmatrix}.\end{aligned} \tag{3.6}$$

Because of our choice of coordinates, $\mathbf{S}(f)$ is very nearly diagonal for all frequencies [93, 107].

It is often useful to generate realizations of $\vec{N}(t)$ to make noise similar to that seen in real data for testing. Most scientific programing languages have built-in routines to draw random samples from a Gaussian distribution with a given covariance matrix. If the PSD is known instead, it is simpler to generate noise directly.

$$\vec{n}(t) = \mathcal{F}_f^{-1}\left[\sqrt{\mathbf{S}(f)\,T}\begin{pmatrix} e^{i\phi_\theta(f)} \\ e^{i\phi_d(f)}\end{pmatrix}\right](t), \tag{3.7}$$

where $\phi_i(f)$ at each frequency is drawn from a uniform distribution between π and $-\pi$

for each $i \in \{\theta, d\}$ and T is the time duration of the signal. Care must be taken to make sure that the phases for the negative frequencies are of opposite sign than the ones for the positive frequencies so that the result is real, $\phi_i(f) = -\phi_i(-f)$. A discrete version of this formula is given in appendix A.

3.2.3 Maximum Likelihood Estimation

Now that we have a model for our data, we can estimate the photon energy for a given pulse record. Since the noise is Gaussian, the maximum likelihood estimate of the model parameters is given by minimizing

$$\begin{aligned}\chi^2\left(\vec{\xi}\right) &= \int_{-\infty}^{\infty} dt \int_{-\infty}^{\infty} dt'\, \vec{x}^{\mathsf{T}}\left(t;\vec{\xi}\right)\, \mathbf{C}^{-1}(t,t')\, \vec{x}\left(t';\vec{\xi}\right) \\ &= \int_{-\infty}^{\infty} df\, \tilde{\vec{x}}^{\dagger}\left(f;\vec{\xi}\right)\, \mathbf{S}^{-1}(f)\, \tilde{\vec{x}}\left(f;\vec{\xi}\right),\end{aligned} \tag{3.8}$$

where $\vec{\xi} = (E, t_0, \delta_\theta, \delta_d)$ and $\vec{x} = \vec{d} - \vec{m}$. The second equality can be proven by using the identity

$$\mathcal{F}_t\left[\bar{\mathbf{C}}^{-1}(t)\right](f) = \mathbf{S}^{-1}(f), \tag{3.9}$$

which follows from equation 3.6, the properties of the covariance matrix, and assuming stationary noise.

Since the DC offsets for each component are not important to analysis of the photon properties, we can simplify the minimization by noting that in the frequency domain the δ_i variables only contribute delta functions at $f = 0$. In the minimization, each $\hat{\delta}_i$ estimate can be tuned to completely cancel the data with the model at $f = 0$, so we can ignore them. A standard nonlinear minimization routine can then be used to find $\hat{E}$ and $\hat{t}_0$ from

$$\hat{E},\ \hat{t}_0 = \underset{E,\ t_0}{\arg\min} \left[\int_{f \neq 0} df\ \vec{x}^{\dagger}\!\left(f; \vec{\xi}_0\right)\ \mathbf{S}^{-1}(f)\ \vec{x}\!\left(f; \vec{\xi}_0\right) \right], \tag{3.10}$$

where $\vec{\xi}_0 = (E, t_0, 0, 0)$. If the noise is not stationary, χ^2 must be minimized with respect to the original covariance matrix and this simplification is not valid.

Under the above assumptions and assuming that all photon events are well isolated in time, this strategy for computing the photon energy results in an unbiased energy estimator with the minimum possible variance even after digitizing to discrete time steps [108, 109]. However, $\vec{m}\left(t; \vec{\xi}\right)$ (and $\mathbf{C}\left(t, t'; \vec{\xi}\right)$ if the noise is not stationary) can be challenging to construct as continuous functions of their parameters. Generative physical models [110, 111], principal component analyses [112–114], and template interpolation [115, 116] have been suggested as ways to properly formulate these functions. Nevertheless, solving equation 3.10 then becomes a nonlinear optimization problem which cannot be solved in real-time.

3.2.4 Filter Estimation

Detector arrays with many pixels and with high count rates require real-time photon energy estimation to reduce the memory required to save a dataset. This condition restricts the analysis to linear algorithms consisting of, for example, filtering operations or matrix multiplications. Tangent filtering has been suggested as one way to linearize a model around a particular energy but also requires several tangent plane calculations to fully cover a detector's bandwidth [103].

To address this issue, we look for an analytic solution of equation 3.10 using a more simple response model. We can remove the energy dependence of the pulse shape and solve for the total detector response, $A(E)$, which can be converted to an energy after the optimization.

$$\begin{aligned}\vec{m}\left(t;\vec{\xi}\right) =& A(E)\ \vec{s}(t-t_0)+\vec{\delta}\\ =& A(E)\begin{pmatrix}\frac{A_\theta}{A_\theta+A_d}\ s_\theta(t-t_0)\\ \frac{A_d}{A_\theta+A_d}\ s_d(t-t_0)\end{pmatrix}+\begin{pmatrix}\delta_\theta\\ \delta_d\end{pmatrix}\end{aligned} \tag{3.11}$$

Here, the fractions involving A_θ and A_d are assumed to be energy independent. Because of the chosen normalization for $\vec{s}$, the amplitude, $A(E)$, represents the sum of the pulse heights in the phase and dissipation direction at a particular energy.

Assuming we know the arrival time, $\hat{t}_0$, we can solve equation 3.10, where we substitute $E \longrightarrow A$ in the minimization, by writing

$$\frac{\partial}{\partial A}\int_{f\neq 0} df\ \vec{\tilde{x}}^\dagger\left(f;\vec{\xi}_0\right)\ \mathbf{S}^{-1}(f)\ \vec{\tilde{x}}\left(f;\vec{\xi}_0\right)\bigg|_{\hat{A},\ \hat{t}_0} = 0. \tag{3.12}$$

The solution to equation 3.12 follows a similar path to that described in reference [117, §B.4] with care taken to properly treat the additional dimensions. The result is conveniently similar.

$$\hat{A} = \frac{\int_{f\neq 0} df\ e^{2\pi f \hat{t}_0}\ \vec{\tilde{s}}^\dagger(f)\ \mathbf{S}^{-1}(f)\ \vec{\tilde{d}}(f)}{\int_{f\neq 0} df\ \vec{\tilde{s}}^\dagger(f)\ \mathbf{S}^{-1}(f)\ \vec{\tilde{s}}(f)} \tag{3.13}$$

If we recast this expression by defining a 2D filter, $\vec{h}(t)$, such that

$$\mathcal{F}_t\left[\vec{h}(t)\right](f) = \begin{cases} \dfrac{\vec{\tilde{s}}^{\dagger}(f)\ \mathbf{S}^{-1}(f)}{\int_{f'\neq 0} df'\ \vec{\tilde{s}}^{\dagger}(f')\ \mathbf{S}^{-1}(f')\ \vec{\tilde{s}}(f')} & f \neq 0 \\ 0 & f = 0 \end{cases}, \tag{3.14}$$

then equation 3.13 can be rewritten as the convolution between the filter and the data at the photon arrival time.

$$\hat{A} = \left[\vec{h}^{\mathsf{T}} * \vec{d}\right]\left(\hat{t}_0\right) \tag{3.15}$$

The photon arrival time, t_0, can be found by noting that at the solution

$$\begin{aligned} 0 &= \left.\frac{\partial \chi^2}{\partial t_0}\right|_{\hat{t}_0} \\ &= \left.\frac{\partial}{\partial t_0}\left[\vec{h}^{\mathsf{T}} * \vec{d}\right](t_0)\right|_{\hat{t}_0}, \end{aligned} \tag{3.16}$$

so the photon arrival time is at the maximum of the continuous convolution of the filter with the data. Using this filter, the detector response at various known energies can be measured and a calibration function, $A(E)$, can be determined to convert from photon energy to pulse amplitude.

$$\hat{E} = A^{-1}\left(\max_t \left[\vec{h}^{\mathsf{T}} * \vec{d}\right](t)\right) \tag{3.17}$$

Despite the simplicity of equation 3.17, the pulse shape often *does* depend on photon energy which can degrade the resolving power slightly when this method is used. Since in this dissertation we will be mostly concerned with the physics limiting the resolving power and less so the implementation of the filtering, we will use different filters tailored to each photon energy when reporting the resolving power to achieve better performance. This procedure is almost as good as the tangent filtering described by Fowler et al. [103] but is much easier to implement and a bit more robust to errors in the pulse template. However, we note explicitly here that a readout system using a single filter per resonator will perform slightly worse than the results shown in the rest of this dissertation where the pulse shape energy dependance is taken into account.

3.2.5 Estimator Variance

To determine if the energy estimators presented in sections 3.2.3 and 3.2.4 are performing correctly, we can compare the expected variance of the estimators to the observed variance when measuring photons with a single, known energy. We start by noting that the variance of an arbitrary estimator, $\hat{\alpha}$, found by minimizing χ^2 is given by

$$\mathrm{Var}\left[\hat{\alpha}\right] = \left[\frac{1}{2}\frac{\partial^2\chi^2}{\partial\alpha^2}\right]^{-1}\Bigg|_{\hat{\alpha}} . \tag{3.18}$$

In the frequency domain, using the χ^2 with no zero-frequency component from equation 3.10, we have

$$\begin{aligned}\mathrm{Var}\left[\hat{E}\right] = \Bigg[\int_{f\neq 0} df\, & \frac{\partial \vec{m}^\dagger\left(f;\vec{\xi}_0\right)}{\partial E}\, \mathbf{S}^{-1}(f)\, \frac{\partial \vec{m}\left(f;\vec{\xi}_0\right)}{\partial E} \\ & - \frac{\partial^2 \vec{m}^\dagger\left(f;\vec{\xi}_0\right)}{\partial E^2}\, \mathbf{S}^{-1}(f)\, \vec{\tilde{x}}\left(f;\vec{\xi}_0\right)\Bigg]^{-1}\Bigg|_{\hat{E}} .\end{aligned} \tag{3.19}$$

For models nonlinear in E, like that in section 3.2.3, this expression still depends on the noise, so we use the expectation value of the variance instead.

$$\mathrm{E}\left[\mathrm{Var}\left[\hat{E}\right]\right] = \left[\int_{f\neq 0} df \, \frac{\partial \vec{\tilde{m}}^{\dagger}\left(f; \vec{\xi}_0\right)}{\partial E} \, \mathbf{S}^{-1}(f) \, \frac{\partial \vec{\tilde{m}}\left(f; \vec{\xi}_0\right)}{\partial E}\right]^{-1} \Bigg|_{\hat{E}} \tag{3.20}$$

The variance estimate can be simplified further for the filtering case from section 3.2.4, which is linear in A.

$$\frac{\partial \vec{\tilde{m}}\left(f; \vec{\xi}_0\right)}{\partial A} = e^{-2\pi i f t_0} \vec{\tilde{s}}(f), \tag{3.21}$$

so from equation 3.19 we have

$$\mathrm{Var}\left[\hat{A}\right] = \left[\int_{f\neq 0} df \, \vec{\tilde{s}}^{\dagger}(f) \, \mathbf{S}^{-1}(f) \, \vec{\tilde{s}}(f)\right]^{-1}. \tag{3.22}$$

To convert to an energy variance, we have to use the inverse calibration function.

$$\mathrm{Var}\left[\hat{E}\right] = \left(\frac{\partial A^{-1}(x)}{\partial x}\bigg|_{\hat{A}}\right)^2 \mathrm{Var}\left[\hat{A}\right] \tag{3.23}$$

Formulas for the variance of these estimators are given in the discrete case in appendix A.

3.3 Correcting Coordinate Saturation

For phase responses greater than ~110°, the coordinates defined by equations 3.1a and 3.1b introduce an energy dependent response shape in violation of the assumptions used to derive equation 3.17. If we could use phase and dissipation coordinates that do not have these artificial effects, energy estimation with the filtering method may become more accurate. With this motivation, we introduce an alternative coordinate system.

3.3.1 Alternative Phase and Dissipation Coordinates

Since we expect $^{\delta f_r}/_{f_r}$ and δQ_i^{-1} to be proportional to the photon energy, these variables are, perhaps, the most obvious choice for the new coordinates. However, the reactive current nonlinearity described by equation 2.23 requires a real-time estimate of the internal quality factor to solve for $^{\delta f_r}/_{f_r}$, amplifying the noise. Instead, we use δx_n as the phase component, which is more linear with photon energy than Θ_1 and approximately equal to $-{}^{\delta f_r}/_{f_r}$ if no reactive nonlinearity exists. δx_n and δQ_i^{-1} can be solved for in terms of $\mathcal{I}$ and $\mathcal{Q}$ by using the adiabatic equivalence between the mixer output, $\mathcal{Z}$, and S_{21}.

$$\begin{aligned}\Theta_2(t) &\equiv \frac{-4Q}{1+4Q^2x_n^2}\,\delta x_n(t) \\ &= \frac{-4Q}{1+4Q^2x_n^2}\left[\frac{\bar{\mathcal{Q}}(t)+2Q_c x_a\left(\bar{\mathcal{I}}(t)-1\right)}{2Q_c\left|1-\bar{\mathcal{Z}}(t)\right|^2}-x_n\right]\end{aligned} \tag{3.24a}$$

$$\begin{aligned}D_2(t) &\equiv \frac{-2Q}{1+4Q^2x_n^2}\,\delta Q_i^{-1}(t) \\ &= \frac{-2Q}{1+4Q^2x_n^2}\left[\frac{\bar{\mathcal{I}}(t)-\left|\bar{\mathcal{Z}}(t)\right|^2+2Q_c x_a\bar{\mathcal{Q}}(t)}{Q_c\left|1-\bar{\mathcal{Z}}(t)\right|^2}-Q_i^{-1}\right]\end{aligned} \tag{3.24b}$$

The prefactor in both equations normalizes Θ_2 and D_2 to the polar coordinates in the small signal limit using equations 3.2a and 3.2b. The normalization facilitates the comparison between the two transformations, shown in figures 3.1 and 3.4, by making them

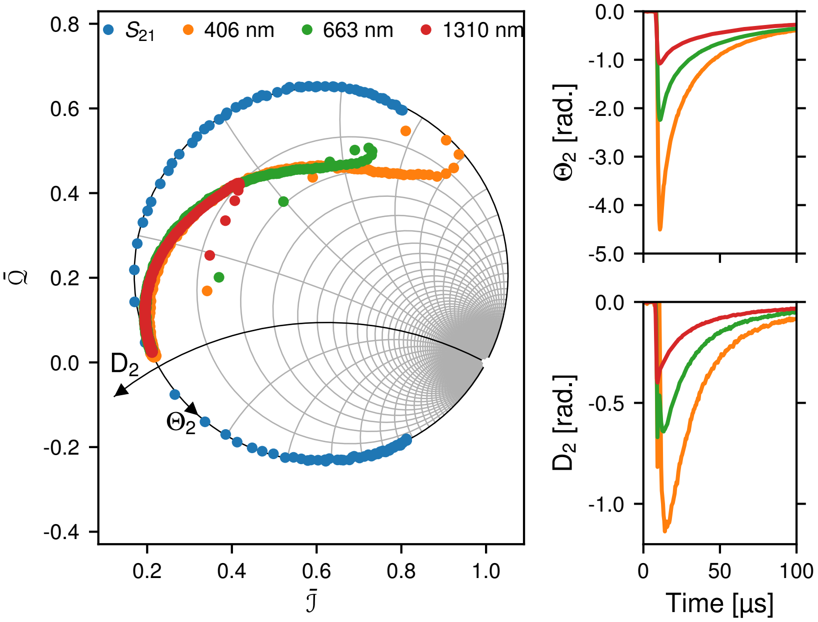

Figure 3.4: The new coordinate transformation is shown in contrast to figure 3.1. Averaged response trajectories for three different photon energies are plotted in the $\mathfrak{I}$ / $\mathfrak{Q}$ plane. Their dependence on time are also shown to the right of the main plot. Both the compression in phase and dissipation are corrected for with the Θ_2 and D_2 coordinates leaving only nonlinearities intrinsic to the detector itself like the energy dependent decay time in Θ_2 and the delayed response in D_2. These coordinates are normalized such that they are approximately equal to the Θ_1 and D_1 coordinates near the resonator's equilibrium point. Their units are written as radians to identify this scaling.

equal near the origin, but it is not critical to the implementation of this method.

This new coordinate system compensates for the saturation in both the phase and dissipation signal, making a linear model for the photon response more valid. Additionally, for MKIDs where the majority of the noise power in the relevant bandwidth comes from two-level systems, the noise becomes stationary. The power spectral density of the noise, $\mathbf{J}(f)$, can then be used in place of the covariance matrix $\mathbf{C}(t, t'; \vec{\xi})$. In contrast, the amplifier noise becomes nonstationary. Care should be taken to properly model the noise if this component limits the resolving power.

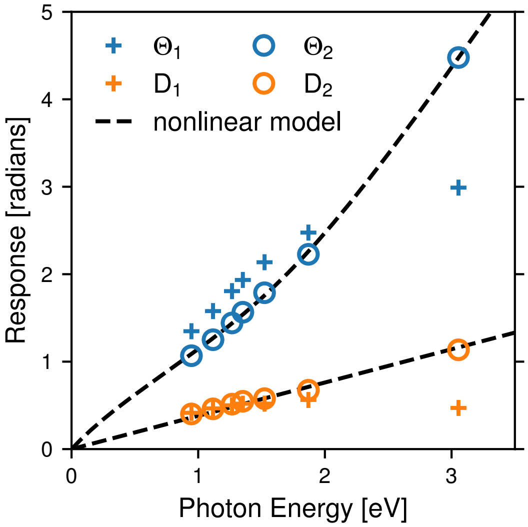

Figure 3.5: The laser calibration energies and detector responses used to construct the calibration functions $A_i(E)$ (equation 3.4) are plotted for both coordinate systems. The responses in the Θ_1 and D_1 coordinates saturate at the higher energies while the Θ_2 and D_2 coordinates undo this effect. Any remaining nonlinear behavior in Θ_2 is well described by equation 2.23 and the fit parameters from equation 2.21 (dashed black line).

3.3.2 Which Coordinates Do We Choose?

The points used to construct the calibration functions, $A_i(E)$, for each coordinate system from equation 3.4 are shown in figure 3.5. As expected the new coordinates significantly improve the detector linearity. The dissipation response becomes completely linear, and the saturation in Θ_1 above 1.6 eV is removed. However, the reactive current nonlinearity in the resonator causes Θ_2 to become nonlinear, resulting in small changes to the response shape across the measured energy range.

The usefulness of these coordinates depends heavily on the type of data being analyzed. Only data where the coordinate saturation is the primary cause of the resolving power degradation will see any benefit. In section 5.2.4 we will show a particular detector where a significant increase in detector performance is observed using this method. In practice, though, it is easiest to just try both coordinate systems to determine which is most useful.

In addition to the detectors presented in this dissertation, other types of single photon counting MKIDs could also benefit from this coordinate transformation. In particular, TKIDs do not have any of the residual response shape nonlinearities seen by optical to near-IR MKIDs and may see all of the response shape energy dependence removed by this method. Any resulting improvement to the resolution of these detectors, however, would depend on the response shape nonlinearity being the primary source of uncertainty in the measured photon energy.

3.4 Attributions

The large signal coordinate transformation and the discussion on pulse filtering from this chapter were developed and published during the course of this dissertation by **N. Zobrist**, N. Klimovich, B. Ho Eom, G. Coiffard, M. Daal, N. Swimmer, S. Steiger, B. Bumble, H. G. LeDuc, P. Day, and B. A. Mazin, "Improving the dynamic range of single photon counting kinetic inductance detectors", Journal of Astronomical Telescopes, Instruments, and Systems **7**, 010501 (2021).

4

Sensor Materials

Each resonator in an ultraviolet to near-infrared MKID array is patterned into a lumped element design since it provides a relatively large photon-sensitive inductor with roughly uniform sensitivity. A microlens array can then be placed on top of the device to focus the light onto the inductor, increasing the fill factor to >90 %. To use this resonator geometry while maintaining a high enough responsivity to detect single photons, the inductors must be made from a high surface impedance and low T_c superconductor. To date, commissioned ultraviolet to near-infrared MKID instruments have used either non-stoichiometric titanium nitride, $\mathrm{TiN_x}$, or platinum silicide, $\mathrm{PtSi_x}$, alloys as the photon-sensitive material in the resonators and have achieved resolving powers of up to 7 at 800 nm [44].

The lowest T_c that can be used in an MKID is determined by the minimum achievable temperature of the employed refrigeration technology since operating the resonators above a temperature of about $T_c/8$ can introduce excess readout noise and reduce the device's internal quality factor, Q_i [76]. Current instruments use adiabatic demagnetization refrigerators because of their relatively low cost, small size, temperature stability, and >10 h hold times. However, the standard base temperature of about 100 mK limits the T_c of an MKID in one of these systems to around 800 mK, near the T_c of $\mathrm{TiN_x}$ and $\mathrm{PtSi_x}$. Dilution refrigerators, in contrast, can reach temperatures of 10 mK and lower. This system enables the use of transition temperatures down to 100 mK as long as the readout frequencies are kept below twice the gap frequency to avoid significant unwanted quasiparticle generation [119]. In practice, it can be difficult to ensure good device thermalization below 40 mK, so a transition temperature above 300 mK may be more desirable.

4.1 Materials in Demonstrated Instruments

There have been three commissioned ultraviolet to near-infrared MKID instruments so far: ARCONS [45, 120, 121], DARKNESS [43, 46, 122], and MEC [47, 123, 124]. Each instrument's detector has a slightly different pixel geometry, is optimized for different photon wavelengths, has a different number of pixels, and is made from different materials. These changes represent a slow evolution towards better detectors as both their primary use case changed and performance improved. The next two subsections focus on the two different materials used to make the resonators in these instruments, comment on why they were chosen, and discuss their characteristics. A more detailed review of potential materials for MKIDs can be found in reference 125.

4.1.1 Titanium Nitride

Titanium nitride was one of the first resistive superconductors with $T_c < 10\,\mathrm{K}$ to be used in superconducting detectors [126]. By varying the relative percentage of nitrogen to titanium, the transition temperature can be tuned from 0.7 to 4.5 K. These films also can have very high internal quality factors $>10^7$.

The ARCONS instrument used $\mathrm{TiN_x}$ detectors with a superconducting transition temperature near 800 mK [45]. 60 nm thick films were measured to have a surface impedance of 25 pH/□. Pixels also had characteristic photon response decay times from 50 to 100 µs. The target wavelength range for this instrument was 400 to 1,000 nm, and the best measured resolving power was 10 at 400 nm and 4 at 1 µm.

One of the main drawbacks of $\mathrm{TiN_x}$ is the sensitivity of T_c to the nitrogen flow rate during the film deposition. For stoichiometric TiN, the films are fairly insensitive to this parameter and the T_c is near 4.5 K. However, for the non-stoichiometric $\mathrm{TiN_x}$ needed for lower transition temperatures, small changes in the flow rate can cause large T_c variations. This behavior results in measurable gradients in the gap energy across a device, which makes it very difficult to accurately design the pixel resonance frequencies.

4.1.2 Platinum Silicide

Platinum silicide was developed for superconducting detectors as a way to make low T_c films that are more uniform than those using $\mathrm{TiN_x}$ [127]. High quality $\mathrm{PtSi_x}$ films are fabricated by first sputter depositing a 30 nm layer of platinum and then 45 nm layer of silicon. The silicide is created by annealing at temperatures over 300 °C. Annealing a bilayer with these thicknesses at 500 °C for 25 min results in roughly a 60 nm thick $PtSi_x$ film. A detector made in this way should have a T_c near 940 mK, a surface inductance of 8.2 pH/□, and response decay times ranging from 30 to 40 μs. Internal quality factors for $PtSi_x$ films can exceed 10^6.

$PtSi_x$ films ended up being almost ten times more uniform than TiN_x films, so both the DARKNESS and MEC instruments use $PtSi_x$ as the sensor material [44]. These detectors are designed for the 800 to 2,000 nm wavelength range, and at 1 μm the best resolving powers achieved with this material were around 7. In practice, though, the excess phase noise in the readout system that these instruments use lowers the resolving power to ~5 [128]. Work is currently being done to correct this issue with the next readout generation.

However, $PtSi_x$ has its disadvantages as well. Films can be expensive because of the required platinum sputter target. Additionally, successful fabrication relies on tightly controlling the deposition rates between the two elements and the annealing temperature, which may require time-consuming readjustment when calibrations drift. These properties make it difficult to consistently deposit these films over long periods of time in a research fabrication environment. In the course of the work performed during this dissertation, our lab has been able to make these films successfully only about half of the time.

4.2 Hafnium

Considering the disadvantages of TiN_x and $PtSi_x$, an ideal sensing material for an ultraviolet to near-infrared MKID, then, is a high surface impedance, low T_c, elemental superconductor which is common, compatible with standard MKID fabrication steps, and whose material properties are easy to control. It is also desirable for the energy resolution of these devices to be less sensitive to phonon-related degradation. Moving to an even lower transition temperature may be helpful for this last consideration since lower T_c films have smaller quasiparticle creation energies and, for a given sensor responsivity, can be made with thicker films. Both of these effects have been shown to suppress phonon escape fluctuations [129]. These aspects provide an important motivation for investigating lower T_c, elemental superconductors as alternative resonator materials for these detectors.

There are several elemental superconductors with transition temperatures below 800 mK. Here, we investigate hafnium as a potential candidate for this application. Its superconducting properties have been probed for use in superconducting tunnel junction detectors [71, 130, 131] and transition edge sensors [132, 133]. Sputtered films have a hexagonal close-packed crystal structure and are in the local superconducting limit with critical temperatures ranging from 140 to 450 mK depending on deposition conditions. Furthermore, the surface impedance and quasiparticle lifetime of hafnium films are similar to those in $PtSi_x$ and TiN_x devices which mean that very little optimization needs to be done to transition detector array designs to this material.

4.2.1 Resonator Properties

A simple test device, shown in figure 4.1, with ten resonators was used to measure the resonator quality and material properties of a 125 nm thick hafnium film without exposing

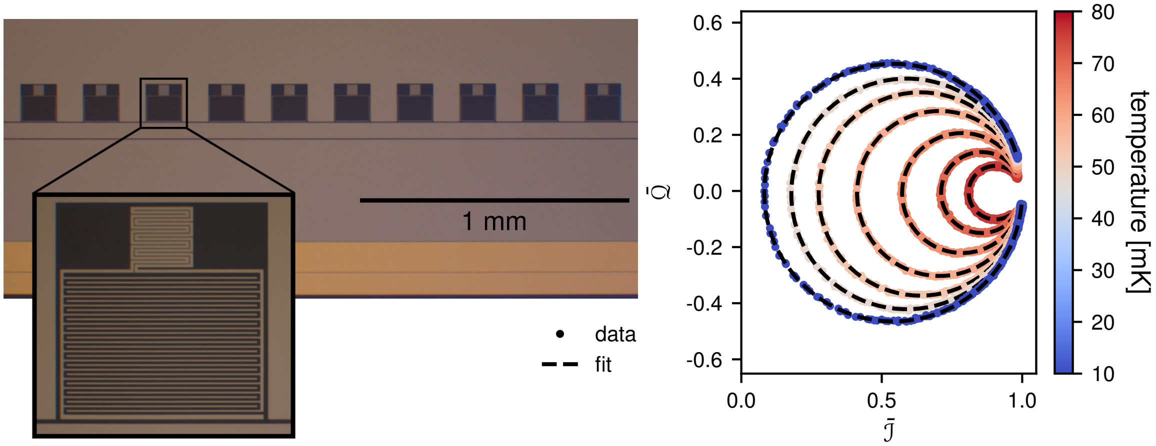

Figure 4.1: The test device is shown on the left. Dark grey, light grey, and yellow areas correspond to the sapphire substrate, hafnium film, and gold bond pad respectively. On the right, the normalized complex transmission of one of these resonators is shown for various temperatures. The fitted gain variations, phase offset, and cable delay are removed from the data in the plots for clarity. This resonator had a coupling and maximum internal quality factor of 17,800 and 203,000 respectively.

it to extra processing steps. The resonators are placed at a 236 µm pitch, and each has a 40 µm × 40 µm inductor and a 100 µm × 130 µm capacitor—a similar design to that used in our current full-scale instruments [44].

The resonance parameters were investigated by fitting the forward scattering parameter, S_{21}, to equation 2.21. Data was taken at temperatures from 10 to 80 mK and with a readout power well below the bifurcation power at about −120 dBm. The readout power is estimated from known attenuations, but an exact calibration does not exist for this system. No significant power dependence was found for Q_i below the bifurcation power. At the lowest temperatures, the average Q_i for these resonators saturates at about 200,000. An example of these fits for various temperatures is shown on the right side of figure 4.1.

This test device was fabricated on a 100 mm diameter a-plane sapphire wafer in a load-locked ultra-high vacuum sputtering system with a typical base pressure of 10^{-7} Pa. To maintain a temperature near 23 °C, the sample was held stationary and backed by an aluminum heat sink. The sputter source was a 150 mm diameter DC magnetron with a hafnium target from Kamis Inc. that has two major impurities: zirconium and oxygen at the <1 wt% and 0.034 wt% level respectively. The film was sputtered at a distance of 10 cm, and the source power was controlled at 500 W, corresponding to a deposition rate of $40\,\mathrm{nm\,min^{-1}}$ with an argon pressure 0.33 Pa. These conditions produce films with a high compressive stress of 1.3 GPa for a 125 nm thick film. By lowering the source power, other test devices have shown higher internal quality factors in excess of 6×10^5 [134].

After deposition, the sample was patterned with a Canon FPA-3000 EX-3 deep-UV stepper with a numerical aperture of 0.65 using 248 nm Cymer laser. GKR-6760 photoresist was used and spun on top of a 100 nm layer of Polymethyl Methacrylate (PMMA) to assist in the removal of the photoresist after the process step. The PMMA layer was oxygen dry etched after developing the resist with AZ MIF-300. The hafnium film was then etched in an Unaxis Shuttleline ICP tool with a BCl_3 + 40 % Cl_2 gas mixture at a pressure of 1.33 Pa, with a 400 W plasma power, and with a 30 W bias power. This system produces vertical sidewall profiles with sub-micron sized features. The chlorine ICP step was followed by oxygen plasma ashing and a deionized water rinse prior to removing the photoresist in solvents. The oxygen plasma ashing was done at relatively high pressure and low power on a graphite electrode in a dedicated RIE system. Gold pads were added to the perimeter of the chip by lift-off e-beam evaporation. Gold wire bonds connect these pads on the perimeter of the 2.5 mm × 16.5 mm chip to its light-tight device box to improve thermalization.

The detectors were designed to have resonance frequencies equally separated in a

500 MHz bandwidth centered around 5 GHz by tuning the capacitor leg lengths slightly between resonators. Assuming $L_s = 16.7\,\mathrm{pH}/\square$ results in the closest agreement between the measured and simulated resonance frequencies [135], so we conclude this value to be the device surface inductance. This surface inductance corresponds to a kinetic inductance fraction, α, of about 0.96 for these resonators.

In addition, the superconducting transition temperature of the device was measured to be $T_c = (395 \pm 5)\,\mathrm{mK}$ using a four-wire measurement on a hafnium sample from the same wafer as the test device. The sample was varnished to an OFHC copper mount on the mixing chamber stage of the refrigerator, and aluminum-silicon wire bonds were used to connect to copper traces on a FR-4 circuit board. Low thermal conductivity, 127 µm diameter, twisted-pair, manganin wires with lengths >30 cm were used to connect the circuit board to a heat sink on the cold plate of the fridge, and a calibrated RX-102A-CD-0.05B thermometer from Lake Shore Cryogenics was bolted next to the sample. Thermometer and sample resistances were simultaneously measured by a Lake Shore 370AC resistance bridge with a model 3716 scanner, and the temperature was controlled using a resistive heater, ramping upward at a rate of $1\,\mathrm{mK\,min^{-1}}$ with the PID controller on the resistance bridge. The error in the T_c measurement is dominated by the thermometer calibration uncertainty.

The sample resistance versus temperature data are displayed in figure 4.2, showing a clear transition from the superconducting to normal state over about 5 mK. The scatter in the resistance measurement is primarily from the thermometer readout. Changing the measurement range to its smallest setting confirms that the resistance at 380 mK is below at least 100 nΩ.

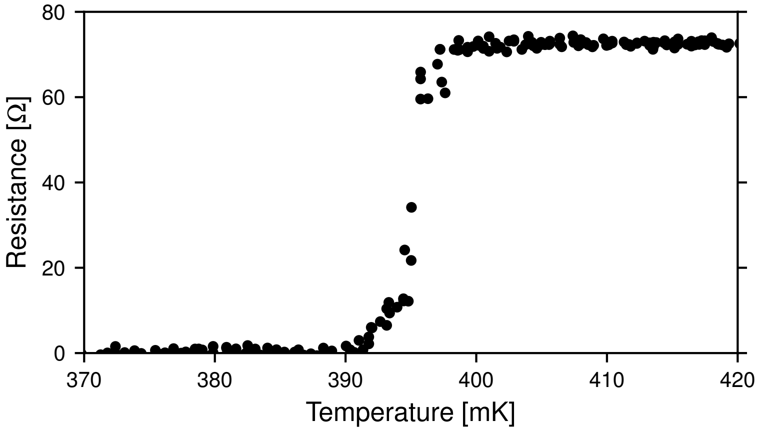

Figure 4.2: Plotted is the resistance of the 125 nm thick hafnium T_c sample as a function of temperature in the region of the superconducting transition.

Non-uniformity in T_c across a wafer is a significant problem for TiN_x MKIDs in large arrays because it yields resonant frequencies different from the design specifications. This hinders frequency multiplexing by depressing the pixel yield due to overlapping resonance frequencies. The film uniformity, therefore, is an important figure of merit for resonator materials used in large arrays. Both $PtSi_x$ [127] and Ti/TiN multilayers [136] have been shown to improve on this problem, so it is important to check that hafnium resonators have similar uniformity. In comparison, the standard deviation of the fractional error between the measured and designed frequencies on the test device was 1.2×10^{-3} which is similar to the measured 7.1×10^{-4} for $PtSi_x$ and compares well to the 1.1×10^{-2} accuracy in TiN_x resonators. The data for $PtSi_x$ and TiN_x are taken from reference 127 in which a line of 9 similar, lumped element resonators was used for each material at a pitch of 444 µm. All of the resonators had kinetic inductance fractions near 1.

The sheet resistance at room temperature can be used to predict T_c uniformity across the whole wafer. We deposited a hafnium film using the process described above, and

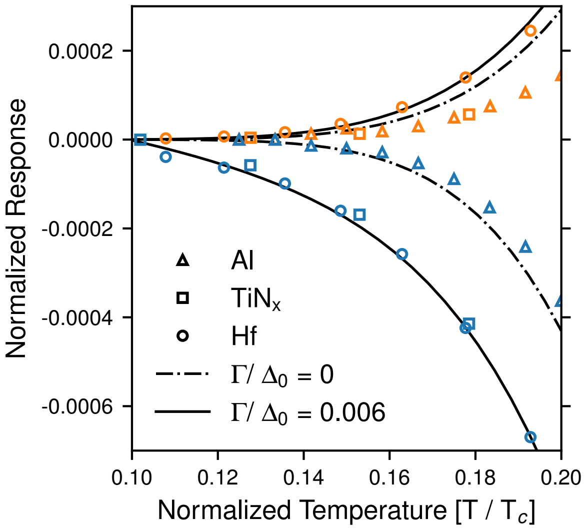

Figure 4.3: The normalized frequency response, $2\delta f_r/(f_r\alpha\gamma)$ (blue), and dissipation response, $\delta Q_i^{-1}/(\alpha\gamma)$ (orange), for different materials are shown. The hafnium data is from the test device described in the text and is fit using the gap-broadened equations for the complex conductivity where the pair breaking parameter and gap energy were varied. The fitted responses with $\Gamma = 0$ are shown for comparison. Data for Al and TiN$_x$ were taken from reference 64.

the sheet resistance was measured at 103 positions on the substrate using a non-contact Lehighton Lei 1510E-SA sheet resistance probe. The average sheet resistance over the 100 mm diameter wafer was (8.11 ± 0.26) Ω/□, corresponding to a resistivity of 97 μΩ cm. We measured a residual resistivity ratio (RRR) of 1.6 between room temperature and 4.2 K with no additional change at temperatures approaching the superconducting transition. The 3 % wafer uniformity is similar to that of PtSi$_x$ and much better than the measured ~20 % for TiN$_x$ [127, 136], matching the expectations set by the frequency placement accuracy in the test mask.

The normalized frequency, $2\delta f_r/(f_r\alpha\gamma)$, and dissipation, $\delta Q_i^{-1}/(\alpha\gamma)$, responses for the test device as a function of temperature are shown in figure 4.3 and compared to those for Al and TiN$_x$ resonators, where γ is a film dependent constant ($^1/_3$ for Al and 1 for TiN$_x$ and Hf) [42]. Typically, the temperature responses are calculated via the complex conductivity using the Mattis Bardeen equations [87], but like resonators made from other superconductors with high disorder, the response of this device is not well described by this theory.

From the measured low temperature resistivity and a Fermi velocity of 1.7×10^6 m/s [137], we calculate a disorder parameter of $k_F l = 13$ using the Drude-Sommerfeld model. This value indicates similar but slightly less disorder than stoichiometric TiN and NbTiN. [65] We therefore use a model for the complex conductivity that has been applied before to these materials [64, 138]. The Mattis-Bardeen equations are extended by adding the Dynes broadening parameter, Γ, to the superconducting density of states as in section 2.1.2 [88]. Physically, this parameter represents a Cooper-pair breaking scattering process caused by impurities in the film, which have the effect of modifying both the temperature dependence of the superconducting gap energy and the complex conductivity [57]. The extended Mattis-Bardeen equations fit well to the hafnium data when we also allow the zero temperature gap energy, Δ_0, to vary. For hafnium, we find $\Gamma/\Delta_0 = 0.006$ and $\Delta_0 = 1.5 k_B T_c$. Other methods have been used to extend the Mattis-Bardeen equations to incorporate gap broadening and may be more or less applicable to hafnium depending on the exact broadening mechanism [66, 139, 140]. Thermal distribution functions are also assumed which do not capture potential non-equilibrium effects [80]. As such, the fit should be interpreted to show a qualitative agreement with this model.

4.2.2 Full Array Measurements

These results show promise for a practical MKID camera, but making a full array of detectors with around 2,000 resonators per feedline requires additional fabrication steps than those used for the test device described above. A lower surface inductance superconductor, like niobium, is used for the transmission line to facilitate better impedance matching, and the ground planes on either side of the transmission line must be electrically connected with crossovers. Typically, we find the lowest Two-Level System (TLS) noise when the resonator metal is deposited first, ensuring a clean interface with the substrate. So, each of these extra steps has the potential to degrade the internal quality factors of the resonators. Unsurprisingly, initial attempts at fabricating a full hafnium MKID array produced unusable resonators with low Q_i.

For $\mathrm{PtSi_x}$, this problem was solved by adding a capping layer of tungsten on top of the resonator material [44]. The capping layer on an MKID array protects the resonator layer from the other fabrication processes and is removed as the final step. A good capping layer, therefore, must etch with the same chemistry as the resonator layer so that the resonator can be patterned, be removable with an etch that stops on the resonator layer, and not degrade the internal quality factor of the resonators. It is also preferable to deposit the capping layer in situ with the resonator layer to ensure a clean interface. Tungsten was unavailable in our deposition system, so we investigated three alternatives: aluminum, niobium, and chromium.

On different portions of the same wafer, resonators were capped with these materials. A section of the wafer was also left uncovered as a control. Each of these materials etch

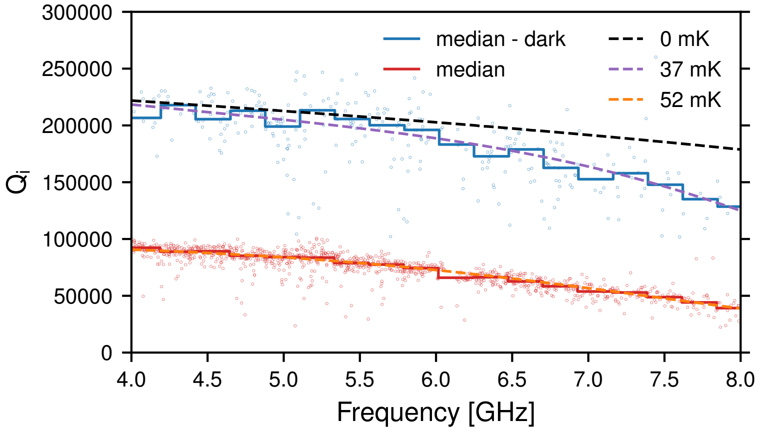

Figure 4.4: The median Q_i of the resonators on this array is shown as a function of binned frequency when the array is either in a light-tight box or exposed to the fridge radiation. The data points represent individual Q_i measurements in each case. The dashed lines show a joint fit to the medians using the model discussed in chapter 2 with an additional constant TLS component. The expected Q_i dependence at zero temperature using this fit is plotted for comparison.

with the same process used for hafnium. After the device was fabricated, the aluminum was removed with a wet etch in MIF-300 resist developer for 1 min; the niobium was removed with a CF_4 + 10 % O_2 ICP etch at 0.933 Pa and low power for 7 min; and the chromium was removed with a wet etch with a standard chrome mask etchant produced by Cyantek. Both the niobium and chromium capping layers had no effect on the measured Q_i when compared to the control device, but the aluminum capping layer reduced the Q_i of the device by over 50 %.

We used chromium as the hafnium capping layer to fabricate a 20,440 pixel MEC-style array [44]. To adjust the film impedance to the MEC design, the hafnium film thickness was also increased to 200 nm. This change also had the effect of better matching the detector sensitivity to the desired 800 to 1,400 nm wavelength range than was done in our test device. Figure 4.4 shows a portion of the microwave transmission amplitude through the device as well as the measured distribution of internal quality factors at 20 mK. We found a median $Q_i = 190{,}000$ across the array when in a light-tight box. Although, when the device box was fitted with a microlens array and exposed to the 4 K radiation environment inside of the fridge, the median Q_i dropped to 77,000.

This behavior deviates from that seen in $\mathrm{PtSi_x}$ arrays where the Q_i does not change when exposed to the same radiation. We can understand this decrease by applying the gap broadened response model to the two data sets, which combines equations 2.14, 2.20 and 2.25 to find the change in Q_i with temperature and frequency. Allowing the TLS loss, device temperature in each case, gap energy, and broadening parameter to vary, we find a joint fit with a TLS component corresponding to $Q_i \sim 260{,}000$, device temperatures of 37 mK and 52 mK, $\Gamma/\Delta_0 = 0.002$, and $\Delta_0 = 1.5 k_B T_c$. The TLS component represents an average, near-constant loss across this frequency and fitted-temperature range.

In both cases, the fitted device temperature is hotter than the measured fridge temperature. The MEC-style arrays are much larger than the test device (24.6 mm × 22.5 mm), and while gold heat sinking is done along the border of the chip, it is possible that this extra area prevents the chip from fully cooling to the fridge temperature. Alternatively, the elevated effective device temperature may also be explained by a non-equilibrium phonon distribution in the superconductor caused by the background radiation [83]. It is unclear which mechanism is occurring, but the 54 mK temperature suggests why this effect was not noticed in $\mathrm{PtSi_x}$ arrays since they are operated near 100 mK. An optical coating on the microlens array may be needed to block this radiation and avoid this effect in future hafnium devices.

Although the Q_i for the full array with the microlens is still significantly lower than in the test device, it is still high enough for this detector application. After probing a typi-

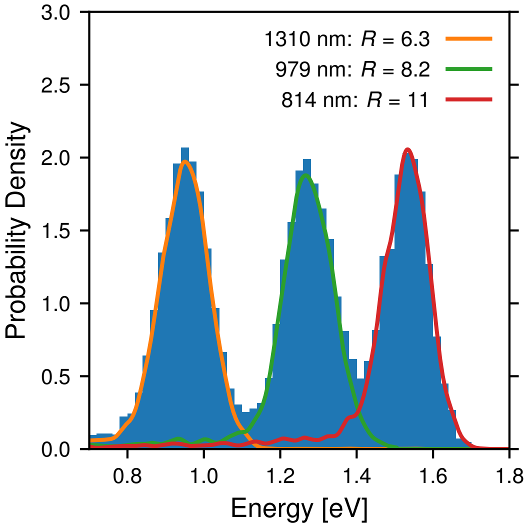

Figure 4.5: A composite spectrum for a resonator in the MEC-style array is plotted. The resonator was at a frequency of 4.99942 GHz, had a Q_i = 66,100, Q_c = 15,700, and was measured at 18 mK. The spectrum was generated by combining data collected with 808 nm, 980 nm, and 1,310 nm wavelength lasers individually. The solid lines correspond to kernel smoothed density estimations of the individual laser distributions and were used to compute the resolving power at each energy. In the inset, an example 808 nm single photon event is shown. We measure average fractional frequency shifts of 3.2×10^{-5} and 1.8×10^{-5} for 808 nm and 1,310 nm events respectively.

cal resonator at around −106 dBm, near the bifurcation power, we illuminated the array with three lasers spanning 800 to 1,300 nm and measured photon absorption events. This data is shown in figure 4.5, and we find that the resolving power of the hafnium MKID slightly exceeds that seen in TiN_x and $PtSi_x$ arrays [44, 45]. For this device and readout, the resolving power is limited by noise coming primarily from two-level systems at low frequencies and from the High Electron Mobility Transistor (HEMT) amplifier at higher frequencies. The pulse decay time in this configuration was 44 µs and 34 µs in the phase and dissipation responses respectively.

4.3 Attributions

The work in this chapter characterizing high quality factor hafnium micro-resonators and their fabrication techniques was developed and published during the course of this dissertation by **N. Zobrist**, G. Coiffard, B. Bumble, N. Swimmer, S. Steiger, M. Daal, G. Collura, A. B. Walter, C. Bockstiegel, N. Fruitwala, I. Lipartito, and B. A. Mazin, "Design and performance of hafnium optical and near-IR kinetic inductance detectors", Applied Physics Letters **115**, 213503 (2019) and G. Coiffard, M. Daal, **N. Zobrist**, N. Swimmer, S. Steiger, B. Bumble, and B. A. Mazin, "Characterization of sputtered hafnium thin films for high quality factor microwave kinetic inductance detectors", Superconductor Science and Technology **33**, 07LT02 (2020). The MKIDs used in this chapter would not be possible without the wonderful device fabrication work done by Grégoire Coiffard, Bruce Bumble, and Miguel Daal.

5

Detector and Readout Noise

The resolving power in any detector is, by definition, limited by noise. However, noise can present itself in many forms and come from many different sources. In this chapter, we discuss additive noise which can be understood as a realization of a random variable with zero mean added to our expected signal. This type of noise is not necessarily stationary since its magnitude can change during the photon response, but it does exist whether or not photons are being absorbed by the detector. We use this property to simplify the noise analysis since we can study it without the detector being illuminated. While not all noise sources are additive, luckily, most of the ones that affect MKIDs fall into this category.

5.1 Types of Noise

Three types of additive noise typically exist in low temperature superconducting systems: thermal, amplifier, and TLS. A fourth kind, generation-recombination noise, which describes noise caused by the constant breaking of Cooper pairs by phonons and their subsequent recombination may also need to be included in this list [42]. Generation-recombination noise can be thought of as a fundamental noise floor for superconducting circuits, and at high temperatures or with large photon fluxes it can be important. However, in the operating state of an ultraviolet to near-infrared MKID the other three sources are much larger.

When considering the magnitude of noise, it is important to be explicit about where the noise is referenced to. Is the noise what is measured at the digitizer? Or, for example, is the noise referred back to the level produced at the source? The latter, also known as input referenced noise, is most commonly used since it is directly related to the physical processes generating the noise. For MKID data, a third option is to refer the noise to the carrier tone. This is equivalent to transforming the noise into the radial coordinates, Θ and D from chapter 3. This representation is most useful for evaluating the signal to noise level and can be derived from the input referred noise by dividing by the square of the resonance loop radius in the $\mathcal{I}$ / $\mathcal{Q}$ plane, noting that the mixer also divides the original voltage PSD by 2. In appendix C.1, we show

$$r = \sqrt{\frac{Z_0 P_f}{2}\left(\left(\frac{Q}{2Q_c}\right)^2 + Q^2 x_a^2\right)} \tag{5.1}$$

P_f is the microwave power on the feedline entering the device, and Z_0 is the transmission line impedance. For low loss devices, $Q_i \gg Q_c$, and minimal impedance mismatches, $2Q_c x_a \ll 1$, we can approximate the loop radius by the simpler formula which is more appropriate when making device independent noise estimates.

$$r \approx \frac{1}{2}\sqrt{\frac{Z_0 P_f}{2}}. \tag{5.2}$$

5.1.1 Thermal Noise

Thermal noise, also known as Johnson-Nyquist noise, arrises from the random thermal motion of electrons and holes in semiconductors and conductors. Johnson was the first to measure this type of noise explicitly [141], and at the same time, Nyquist provided a theoretical explanation using the equipartion theorem [142]. Any lossy transmission line, attenuator, or termination will exhibit this kind of noise. The single-sided voltage noise PSD on a transmission line at temperature, T, is given by

$$S_V(f) = 4k_B T Z_0. \tag{5.3}$$

This formula is often used incorrectly, however, since typically a component emitting thermal noise in a transmission line is connected to more components with the same input impedance of Z_0. In this loaded case, the noise voltage on the transmission line is divided by 2 and the PSD is divided by 4, giving

$$S_V(f) = k_B T Z_0. \tag{5.4}$$

Note that the noise in each quadrature of the signal ($\mathcal{I}$ or $\mathcal{Q}$) is half of this value which may cause some confusion with factors of two. See appendix C.1 for more details.

We include an attenuator in the fridge before the device in our setup to reduce thermal noise coming from the room temperature components. While we can always make the input signal larger to accommodate this attenuation, the input thermal noise will be set by the temperature of the attenuator. Colder is always better, but the amount of attenuation used is an optimization between the amount of heat dissipation and the amount of reduction needed in the room temperature noise.

Following the derivation in appendix C.1, the single-sided PSD referenced to the carrier tone for the input attenuator is written

$$\begin{aligned} S_{\text{rad}}(f) &= \frac{S_V(f)}{2r^2} \\ &= \frac{4k_B T}{P_f\left(\left({}^{Q}\!/_{Q_c}\right)^2 + 4Q^2 x_a^2\right)} \\ &\approx \frac{4k_B T}{P_f} \end{aligned} \tag{5.5}$$

In a real system, the temperature in equation 5.5 will likely be higher than the fridge temperature either because there is some parasitic heating due to the carrier tone or because of the higher temperature noise from warmer attenuators leaking into the system.

5.1.2 Amplifier Noise

All of the amplifiers in the readout chain add noise to the signal which typically comes from a combination of frequency independent thermal and shot noise internal to the amplifier. The similarity between thermal and amplifier noise justifies using the noise temperature formalism. The noise temperature of an amplifier, T_N, is defined as the increase in the source impedance temperature, T, required to produce the observed noise power in the system [143]. The input noise of the amplifier with its source impedance is written as

$$S_\mathrm{V}(f) = k_B(T + T_N)Z_0 \tag{5.6}$$

For an MKID, the source impedance is usually a 50 Ω attenuator on the transmission line at the base temperature of the fridge as discussed in section 5.1.1, and the amplifier is usually a HEMT with $T_N > 2$ K. Since we treat the source impedance separately, the amplifier contribution to the noise is given by

$$S_\mathrm{V}(f) = k_B T_N Z_0. \tag{5.7}$$

The noise temperature of an amplifier is a useful concept in cryogenic electrical engineering because it tends to scale with the temperature of the amplifier and is directly comparable to the temperature of the system, which defines the thermal noise floor. However, it can also depend on the bias settings used to power the amplifier. Usually T_N can be looked up on the amplifier manufacturer's datasheet.

In units of radians, referenced to the carrier tone, the amplifier noise formula is almost identical to that of the thermal noise, but T_N is used instead of the actual temperature.

$$\begin{aligned} S_\mathrm{rad}(f) &= \frac{4k_B T_N}{P_f\left((Q/Q_c)^2 + 4Q^2 x_a^2\right)} \\ &\approx \frac{4k_B T_N}{P_f} \end{aligned} \tag{5.8}$$

5.1.3 Quantum Limited Noise

At $k_BT \ll hf_g$, where f_g is the carrier frequency created by the signal generator, equation 5.4 is no longer valid. The full formula for the single-sided PSD of a loaded resistor at a temperature, T is really given by

$$\begin{aligned} S_{\mathrm{V}}(f) =& hf_gZ_0\left(\frac{1}{e^{hf_g/k_BT}-1}+\frac{1}{2}\right) \\ =& \frac{hf_gZ_0}{2}\coth\left(\frac{hf_g}{2k_BT}\right), \end{aligned} \tag{5.9}$$

where the first term is the standard Plank blackbody radiation law and the second term is the half-quantum of zero-point fluctuations, also known as vacuum noise [144]. Equation 5.9 approaches equation 5.4 for $k_BT \gg hf_g$. Like all of the equations for down-converted signals, this equation is only valid as long as $f \ll f_g$. In this limit, however, the quantum limited thermal noise is still constant in frequency. An interesting point to note, here, is that at 6 GHz, the thermal noise of a 50 Ω resistor at a temperature of ~262 mK is equal to the zero-point fluctuation noise, so operating significantly below 100 mK does not improve thermal noise performance.

It's important to clarify that any attenuation applied to a readout chain does not attenuate the zero-point noise as it is a fundamental property originating from a Heisenberg uncertainty relationship between the bosonic annihilation and creation operators. As such, it plays the role of the lowest possible noise an electronic system can have. Similarly the zero-point noise does not add with that of other sources and should be included only once in a calculation.

Using the same definition of noise temperature as in section 5.1.1, the amplifier noise referenced to the input and including the source impedance is modified to the following:

$$\begin{aligned} S_\mathrm{V}(f) =& \frac{hfZ_0}{2}\coth\left(\frac{hf}{2k_B(T+T_N)}\right) \\ =& \frac{hfZ_0}{2}\left(\coth\left(\frac{hf}{2k_BT}\right)+2A\right), \end{aligned} \tag{5.10}$$

Right away, we see that the definition of noise temperature is less useful at lower temperatures for quantum limited amplifiers. It is no longer linear with respect to the noise, so we can not decouple its definition from the operating temperature of the source impedance. Instead, it is more natural to adopt the added noise number, A, in units of photon quanta as the standard for comparing noise at low temperatures. Quantum mechanics adds a limit to how small A can be for a phase insensitive linear amplifier [144].

$$A \geq \frac{1}{2}\left|1-\frac{1}{G}\right|, \tag{5.11}$$

where G is the power gain of the amplifier. A parametric amplifier operates around this limit, while a HEMT typically has $A \sim 5$ to 20.

The amplifier contribution to the noise, referenced to the carrier tone is then

$$\begin{aligned} S_\mathrm{rad}(f) &= \frac{4hf_g}{P_f\left(({}^{Q}/_{Q_c})^2+4Q^2x_a^2\right)}A \\ &\approx \frac{4hf_g}{P_f}A. \end{aligned} \tag{5.12}$$

Before moving on, we note that the noise temperature of a quantum limited amplifier is often redefined to scale linearly with the noise and is used instead of A because it has more familiar units. Referencing equation 5.8 and equation 5.12, $T_N \equiv \frac{hf_g}{k_B}A$, which is a completely valid way of expressing noise as a temperature as long it is made explicit. Unfortunately, many published works do not clarify that they are using this definition instead of the original.

5.1.4 Two-Level System Noise

TLS noise originates from ensembles of two-level tunneling states that are often present on the surfaces and interfaces of materials or inside of lossy dielectrics [145]. For some systems, the TLS component contributes a measurable amount to the internal quality factor of the resonator, Q_i. However, when it comes to noise, the two-level system noise only effects the phase response of the resonator. Fluctuations in the dissipation signal are suppressed by an extra factor of the power at the device and so are not observed even at the lowest noise levels [107].

A microscopic understanding of these systems is far from the present state of research. Current models fail to predict different aspects of measured results, like the frequency dependence, and the community has not settled on one overarching description. However, one phenomenological model has been successful in explaining the power dependence of experiments with superconducting resonators. Gao et al. [146] developed a geometric model for this noise given by the equation

$$\frac{S_{f_r}(f)}{f_r^2} = k(f, f_r, T)\frac{\int_{V_{\mathrm{TLS}}} \left|\vec{E}(\vec{r})\right|^3 d^3\vec{r}}{4\left(\int_V \epsilon(\vec{r})\left|\vec{E}(\vec{r})\right|^2 d^3\vec{r}\right)^2}. \tag{5.13}$$

Here, $S_{f_r}(f)$ is the resonance frequency power spectral density. The integrals are done over the volume of TLS sources, V_{TLS}, and the total volume containing the fields, V. The $k(\nu, f_r, T)$ term gives the spectral shape of the noise and has not been determined analytically. It has units of $\mathrm{s}^6\ \mathrm{A}^3\ \mathrm{kg}^{-1}\ \mathrm{m}^{-2}$. In most measurements, $k(f, f_r, T) \propto f^{-\beta}$, where $\beta \approx 1$. Since changes in f_r modify S_{21}, at high frequencies the TLS noise is rolled off at the resonator bandwidth according to equation 2.26.

The resonance frequency power spectrum can be converted into a phase response power spectrum referenced to the carrier tone using equations 2.26, 3.2a and 3.3.

$$S_{\mathrm{rad}}(f) = \left|\frac{1 - \bar{S}_{21}(f_g + f)}{1 - \bar{S}_{21}(f_g)}\right|^2 \left(\frac{4Q}{\left(1 + 4Q^2 x_n^2\right)\left(1 + {}^{8aQx_n}/_{(1+4Q^2x_n^2)^2}\right)}\right)^2 \frac{S_{f_r}(f)}{f_r^2} \tag{5.14}$$

On resonance, this equation simplifies to

$$S_{\mathrm{rad}}(f) = \frac{16Q^2}{1 + ({}^{2Qf}/_{f_r})^2} \frac{S_{f_r}(f)}{f_r^2}. \tag{5.15}$$

Putting all of the known scalings together, we arrive at a more practical formula which can be used to fit a power spectrum to k_{TLS} and β given a fit of S_{21} and knowledge of the readout power.

$$\begin{aligned} S_{\mathrm{rad}}(f) &= k_{\mathrm{TLS}} \left|\frac{1 - \bar{S}_{21}(f_g + f)}{1 - \bar{S}_{21}(f_g)}\right|^2 \left(\frac{4Q}{\left(1 + 4Q^2 x_n^2\right)\left(1 + {}^{8aQx_n}/_{(1+4Q^2x_n^2)^2}\right)}\right)^2 \left(\frac{10^{-10}\,\mathrm{mW}}{P_f}\right)^{1/2} \left(\frac{1\,\mathrm{kHz}}{f}\right)^{\beta} \\ &\approx \frac{16Q^2 k_{\mathrm{TLS}}}{1 + ({}^{2Qf}/_{f_r})^2} \left(\frac{10^{-10}\,\mathrm{mW}}{P_f}\right)^{1/2} \left(\frac{1\,\mathrm{kHz}}{f}\right)^{\beta} \end{aligned} \tag{5.16}$$

The last approximation assumes that $f_g = f_r$. k_{TLS} is the magnitude of the noise at −100 dBm and allows for easy comparison between datasets. This equation fits experimental data well, however, we provide no justification for the power law used to express the TLS noise frequency scaling.

5.2 Reducing Amplifier Noise

Photon counting MKIDs operate differently than MKIDs designed for longer wavelength detection in the bolometric regime. Instead of measuring a constant flux of photons, they record individual photon events similarly to an X-ray calorimeter. To achieve a measurable detector response for a single photon event they tend to be smaller and able to handle less signal power than their longer wavelength bolometric counterparts. In these conditions, amplifier noise can be comparable in magnitude to the detector phase noise that originates from microscopic TLS states on the surface or between layers of the device [145]. The TLS noise can be mitigated through careful sample preparation [147], fabrication [148, 149], and device design [150–152] while the effect of amplifier noise can be addressed by designing detectors that can handle higher signal powers [153, 154]. These routes are actively pursued, but, for ultraviolet to near-infrared MKIDs, improving the main readout amplifier's noise floor offers an additional path to lowering the total system noise.

To readout an ultraviolet to near-infrared MKID array, the primary amplifier must have a moderately high saturation power, significant dynamic range, and a large bandwidth. HEMT amplifiers are often used to satisfy these requirements [155, 156]. State of the art commercial HEMT amplifiers operating over 4 to 8 GHz at 5 K typically reach added noise numbers, in units of quanta, as low as $A = 5.0$ [157]. In practice, the observed A

for a HEMT is between 5 and 20 because of the extra attenuation introduced getting the signal from the coldest stage of the fridge to the 4 K stage where the HEMT is mounted due to cooling power requirements. A quantum limited amplifier that could operate in these conditions at the coldest temperature stage of the fridge would reduce the added amplifier noise by a factor of between 10 and 40.

5.2.1 Parametric Amplifiers

Superconducting parametric amplifiers have been shown to perform at or near to the quantum limit and have been used in several experiments with superconducting resonators. A ∼1 MHz, bandwidth format was used to investigate a superconducting resonator's noise properties in the dissipation quadrature [107]. However, only one resonator could be measured at a time, and a carrier suppression tone was needed, which made the amplifier incompatible with single photon measurements. At low signal powers, larger bandwidth formats have been able to read out up to 20 superconducting qubits [158]. This readout system, too, does not have enough dynamic range for an ultraviolet to near-infrared MKID array as the amplifier's saturation power is on the order of the required signal tone's power.

Traveling Wave Parametric Amplifiers (TWPAs) based on a superconductor's nonlinear kinetic inductance were designed to handle this wide-band, high power and dynamic range case [159–161]. In this chapter we show how one of these parametric amplifiers can be integrated with a large MKID array and demonstrate its ability to measure single photon events with quantum limited amplifier noise.

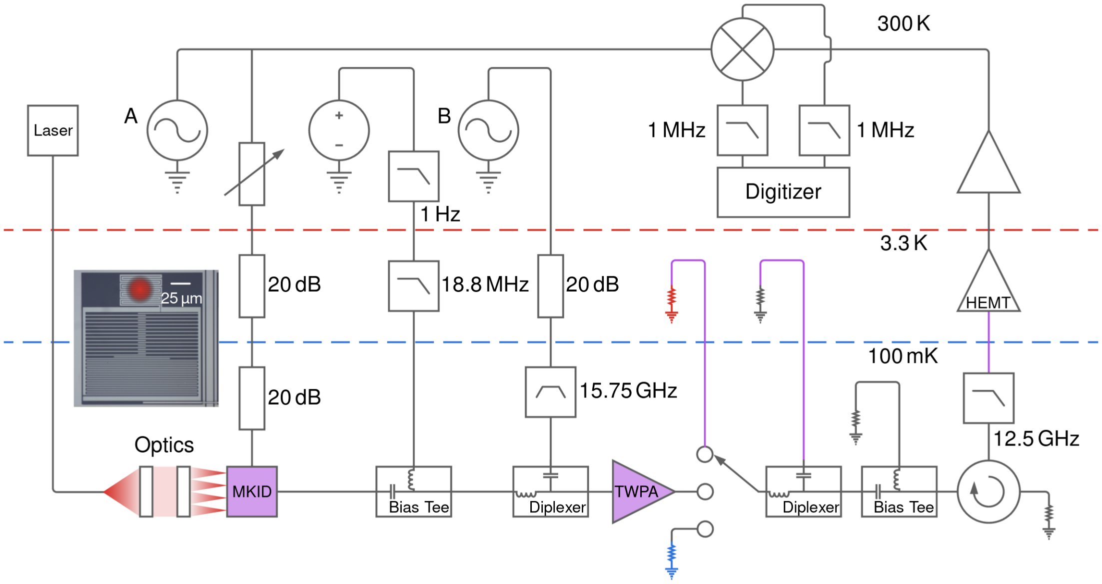

Figure 5.1: Circuit diagram of the readout system. The two synthesizers are labeled A and B for the signal and pump tones respectively. 50 Ω terminations are represented as resistors to ground, and superconducting components are shaded purple. The diagram does not include line losses. The system noise is measured using a cryogenic switch which can connect the HEMT amplifier, to the parametric amplifier, or to one of two matched 50 Ω loads on different temperature stages (shaded red and blue). Light from a laser is directed to the MKID array with an optical fiber and focused onto each inductor with a collimating lens and microlens array. The approximate spot size on one resonator in the array is shown in red in the inset image.

The full readout is divided between three temperature stages with most of the large electronics at room temperature. The rest of the components are cooled to either 3.3 K or 100 mK in a Leiden Cryogenics CF-200 dilution refrigerator with the MKID array and TWPA inside of a Amumetal 4K magnetic shield developed by Amuneal. Outside of the cryostat we employ a homodyne readout system with the signals digitized at a sample rate of 2 MHz after being low pass filtered at 1 MHz to prevent aliasing. Figure 5.1 shows a schematic of the setup used for this experiment.

The parametric amplifier itself is a wide-band, traveling-wave, kinetic inductance amplifier of the general type first described by Eom et al. [161], but is an updated version and differs in several respects. The coplanar wave guide transmission line structure uses finer features (e.g. the center line width and gaps are 320 nm). In order to lower the characteristic impedance to 50 Ω, added capacitance is provided with a interdigitated structure in a similar manner to the amplifier described by Chaudhuri et al. [160]. Additionally, the amplifier is operated in a three-wave mixing mode by applying a DC bias current using the technique shown by Vissers et al. [162].

Operation of the amplifier using three-wave mixing requires the use of both a pump tone and a DC bias current. The pump tone (from synthesizer B in figure 5.1) at 14.765 GHz is attenuated by 20 dB at 3.3 K and filtered using a 14.5 to 17 GHz Marki FB-1575 bandpass filter to ensure that phase noise from the pump generator does not leak into the signal band. The pump tone power at the input of the amplifier is about −23 dBm. The tone is then combined with a DC current of approximately 0.7 mA to produce about 15 dB of gain from 5 to 10 GHz. The two Anritsu K250 bias tees and the two Marki DPX-1114 diplexers isolate the DC current and pump tone from the other components, respectively. The diplexers have over 60 dB of isolation at the pump frequency, and the pump tone is terminated on the cryostat ground at 3.3 K where there is more cooling power. The parametric amplifier is then protected from reflections off of the warmer components with a 3 to 11 GHz Pamtech CTH1365K10 isolator.

Input signal saturation occurs when the amplified signal power at the output of the amplifier is approximately 15 dB below the pump power. At that point, the pump amplitude becomes depleted and the operating point of the amplifier is altered. For 15 dB gain, this results in an input signal saturation power of around −53 dBm. The large saturation power obviates the need for any carrier suppression tones. For this array, even if all of the signal tone power from a simultaneous measurement of a full feedline of resonators reached the amplifier input, it would take −86 dBm of power per tone before reaching saturation, well above the typical operating point of an ultraviolet to near-infrared MKID. In practice, most of the signal tone power is reflected by the MKIDs before reaching the parametric amplifier, so higher signal powers might be usable.

The second low temperature amplification stage is a 4 to 12 GHz CIT412 HEMT amplifier from Cosmic Microwave Technology with about 32 dB of gain and thermalized to the 3.3 K temperature stage with a copper heat strap. A low pass filter is included before the amplifier input to ensure that the pump tone does not leak past the diplexers and saturate the HEMT. This amplifier is required because TWPA does not have enough gain to boost the signal above a standard room temperature amplifier's noise floor.

5.2.2 System Noise Characterization

Since the transmission through the TWPA is near unity when unpowered, we can perform an extended Y-factor measurement of the system. This method allows us to accurately determine the noise components and assign them to different elements in the setup. Table 5.1 shows this breakdown for a signal tone slightly detuned from the MKID resonance frequency. The details of the procedure used to collect this data are laid out in appendix C.

A_I	A_P	A_H	A_{sys}
$0.71^{+0.03}_{-0.03}{}^{+0.08}_{-0.01}$	$0.59^{+0.03}_{-0.03}{}^{+0.08}_{-0.09}$	$19.5^{+0.08}_{-0.08}{}^{+3}_{-1}$	$2.12^{+0.01}_{-0.01}{}^{+0.8}_{-0.1}$

Table 5.1: Maximum likelihood estimates for the input, TWPA, HEMT, and total system noise in units of quanta at 5.675 GHz (from left to right). 1σ statistical errors then systematic errors are reported to the right of the estimates. The HEMT noise level corresponds to a noise temperature of about 5.3 K and is within the manufacturer's specifications for the amplifier. The measurement used to determine these numbers and errors is detailed in appendix C.

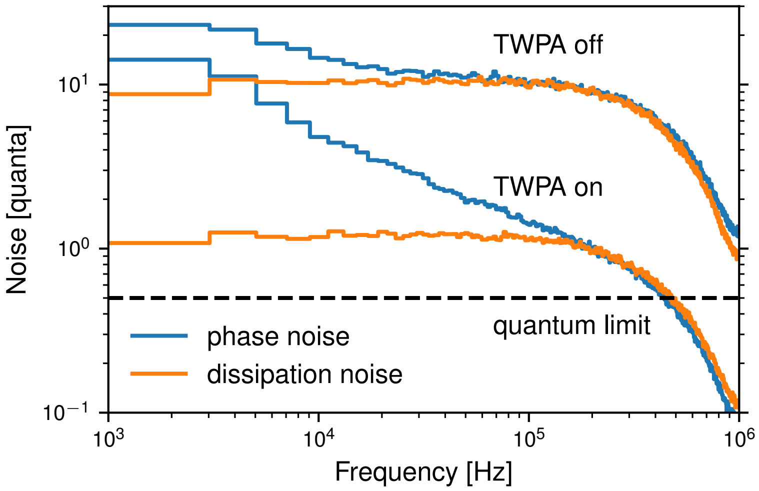

Figure 5.2: Noise on resonance in both signal quadratures with the parametric amplifier's pump tone and DC current on and off. When on, the input referenced white noise level decreases to about a factor of two above the quantum limit of a half photon per quadrature. Each quadrature contributes a quarter of a quanta for the zero-point noise and a quarter of a quanta for the amplifier noise in this limit.

While the TWPA is performing near optimally, some aspects of the system may be improved. The observed system noise is about two times the achievable limit. Almost 75 % of this excess comes from the HEMT amplifier. This effect could be mitigated by either increasing the TWPA's gain or using a lower noise secondary amplifier. Additionally, the input noise is about 0.2 quanta larger than one would expect from a 100 mK termination. It could be brought closer to its lower bound by increasing the lowest temperature attenuation to block more of the thermal noise from the 3.3 K and 300 K stages.

Figure 5.2 shows the noise in the bandwidth of our signal with the signal tone set to the MKID resonance frequency. This state is used for all of the single photon measurements. The flat component of the noise decreased by a factor of 9.6 when the parametric amplifier was powered, with the noise level in the dissipation response quadrature matching the off resonance noise floor for the system. In the phase response quadrature, there is signifi-

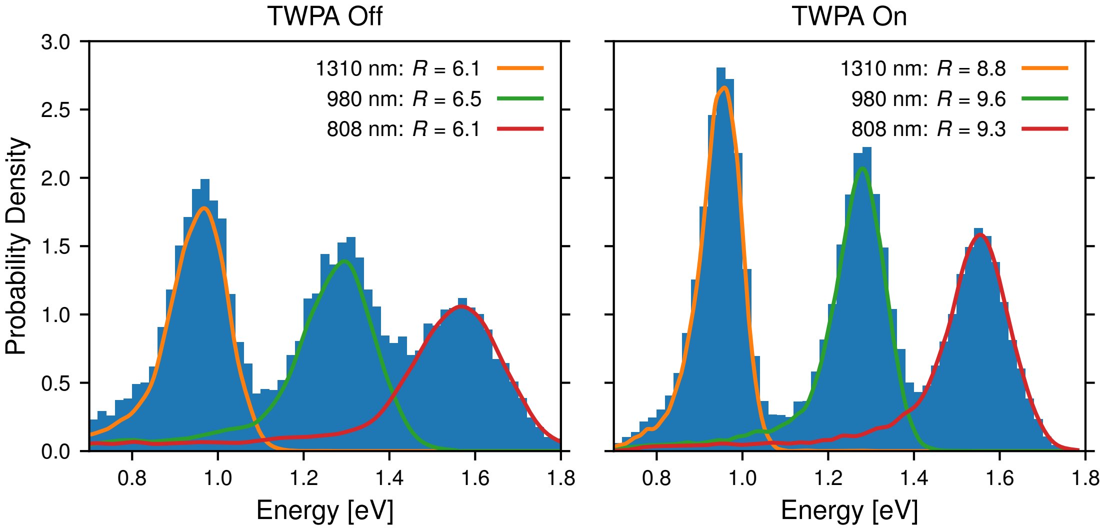

Figure 5.3: The normalized estimated photon energy distributions are plotted for three different laser energies when the TWPA's DC current and pump tone are turned off (left) and on (right). The TWPA clearly improves the spectral widths. The solid lines are kernel density estimations used to calculate the resolving powers listed in table 5.2.

cant low frequency noise which we attribute to TLS noise in the detector.

5.2.3 Platinum Silicide Resolving Power Measurements

The detector that we tested was designed for the MEC instrument at the Subaru telescope on Maunakea in Hawaii [123]. It has ten niobium coplanar waveguide feedlines and a 20,440 pixel platinum silicide MKID array multiplexed over 4 to 8 GHz [44]. Each pixel is a lumped element resonator, capacitively coupled to one of the feedlines. A microscope image of a pixel is shown in the inset of figure 5.1.

For the photon measurements, we used five laser diodes with wavelengths from 808 to 1,310 nm. The 1,120 nm diode was purchased from Eagle Yard, and the others were purchased from Thor Labs. The diode light was coupled into a fiber using an integrating sphere and sent into the fridge. Near the detector, the fiber output was collimated and directed toward

Energy [eV]	Resolving Power [E/ΔE]	
	Measured	Expected
1.52 (814 nm)	6.1 → 9.3	10 → 27
1.35 (917 nm)	6.5 → 9.4	11 → 27
1.27 (979 nm)	6.5 → 9.6	11 → 27
1.12 (1,110 nm)	6.5 → 9.2	10 → 26
0.946 (1,310 nm)	6.1 → 8.8	8.9 → 22

Table 5.2: The measured increase in the resolving power is shown by comparing data with the TWPA unpowered and powered for different photon energies as indicated by the arrows. The expected resolving power based on the noise level, is also specified using equations 3.17 and 3.23. The detector response starts to saturate, as designed, at the highest energies, so the resolving power begins to decrease.

a microlens array on top of the device. The microlens array focused the light onto the inductor of each pixel and was purchased from Advanced Microoptic Systems. It is made from 1 mm thick STIH53 glass with 140 × 146 lenslets at a 150 µm pitch.

We chose a resonator from the array at 5.67446 GHz with a coupling and internal quality factors of 15,100 and 190,000 respectively for this test. All data taken off resonance was captured at a frequency of 5.675 GHz. Near the resonance frequency the parametric amplifier had a constant gain of 13.7 dB, and the resonator was driven almost to saturation at about −106 dBm. When the parametric amplifier is turned on, we see changes in the coupling quality factor of some resonators on the order of ~10 %. More isolation between the parametric amplifier and MKID array could remove this effect, but since this difference is smaller than the variation intrinsic to the design, modifications were unnecessary for this test.

When the detector is illuminated, we measure a two dimensional pulse record for each photon event described in chapter 3. From a record, we can calculate a maximum likelihood estimate of the photon's energy and arrival time. Since the pulse decay time is about

35 µs, care was taken to use low count rates (<200 Hz) and to exclude photons which arrived within 2 ms of each other to ensure clean event records.

Figure 5.3 shows the resolving power measurement for 808 nm photons with the TWPA's pump tone and DC current both on and off, along with the kernel density estimations of the distributions that were used to compute the resolving power. We note that even though the dissipation noise is significantly smaller than the phase noise when the parametric amplifier is on, the smaller dissipation signal for this detector means that roughly 90 % of the expected resolving power can be achieved with the phase signal alone.

Using TWPA clearly improves the resolving power, but the results do not match the expected values for the noise level in the system. Table 5.2 shows this discrepancy over the five measured photon energies. Our noise model does not account for the small, non-stationary decrease in phase noise during a photon event, but we still see this discrepancy when estimating the energy using only the dissipation signal, which has stationary noise. Additionally, since the actual phase noise for a given event is smaller than a stationary noise model predicts, non-stationary noise is unlikely to explain the measured discrepancy in resolving power.

The response of a MKID induced by a uniform distribution of quasiparticles differs from the response from a localized quasiparticle distribution. In the localized case, the detector response is proportional to the square of the current density multiplied by the quasiparticle distribution integrated over each position in the resonator [93]. Therefore, the non-uniform current density in the resonators can also contribute to an uncertainty in pulse height and account for the skewed distribution in figure 5.3. In an ideal lumped element resonator, all of the current is in the inductor and none is in the capacitor, so it is

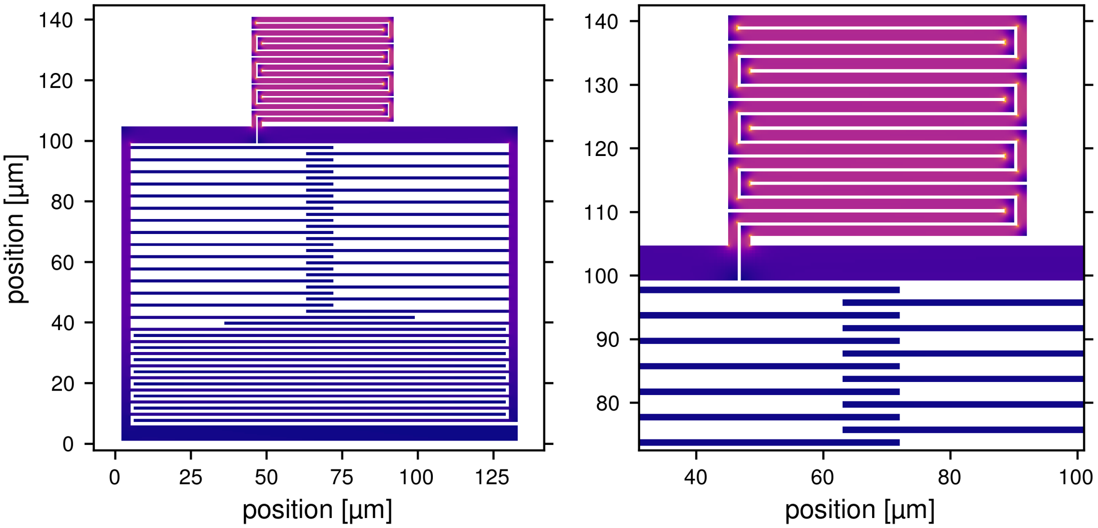

Figure 5.4: The simulated current density for the full resonator used in this section is shown on the left. The photon-sensitive portion of the resonator is shown in more detail on the right. The scale for the current density is arbitrary.

important to ensure a uniform current distribution in the inductor during the design of the sensor. This effect is strongly dependent on the diffusion constant for platinum silicide, which is unknown for our films.

To evaluate the magnitude of this problem, the current distribution was computed in a Sonnet simulation for this resonator and is shown in figure 5.4. It takes the resonator about 1 µs to respond to a photon absorption event, and in that time, the quasiparticles will have diffused an amount determined by the superconductor's diffusion constant. This time scale roughly sets the amplitude of a photon pulse since at longer time scales the quasiparticles begin to recombine. In similar films the diffusion constant has been measured to be ~2 to 8 $\mathrm{cm}^2\,\mathrm{s}^{-1}$ [163], so we use this range for our analysis.

To model the effect of the current non-uniformity, we randomly selected photon absorption locations on the inductor, solved the diffusion equation for each one, and computed the resulting response. Photon strikes in the capacitor have normalized responses

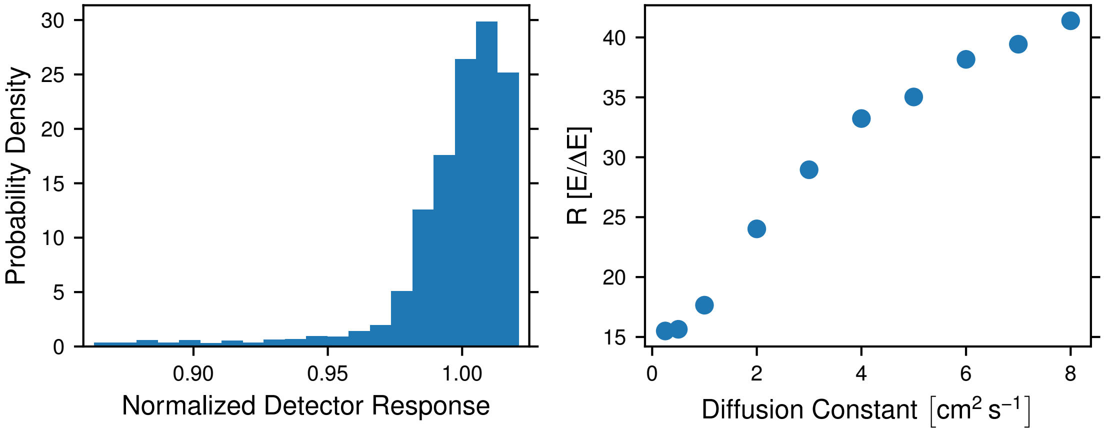

Figure 5.5: The effects of the current non-uniformity on the detector resolving power are shown. All other sources of noise are ignored. For a random photon absorption location on the inductor, the distribution of responses is shown for a diffusion constant of $3\,\mathrm{cm^2\,s^{-1}}$ (left). Larger diffusion constants result in higher resolving powers (right).

$\ll$0.5 and are excluded from the calculation to increase the throughput. The distribution of responses for several different diffusion constants was computed to estimate its effect on the resolving power. The results are shown in figure 5.5 and suggest an expected $R \sim 25$ to 40. Pulse shape variations may also contribute, but we expect them to be small since the quasiparticle distribution averages out the current non-uniformities at time scales on the order of the quasiparticle recombination rate. In our data, we do not see significant variations in the pulse shape for photons of the same energy with different pulse heights. These results suggest that the resolving power limit does not come from the system noise or detector geometry. In chapter 6, we will identify the most likely source and attempt to correct it.

As a note, the results presented in table 5.2 are slightly different than those given in reference 105 despite being from the same dataset. Reference 105 employed a more complicated method than used here to extract the photon energies in an attempt to ensure that the degradation in resolving power was not related to the type of analysis. Since these results

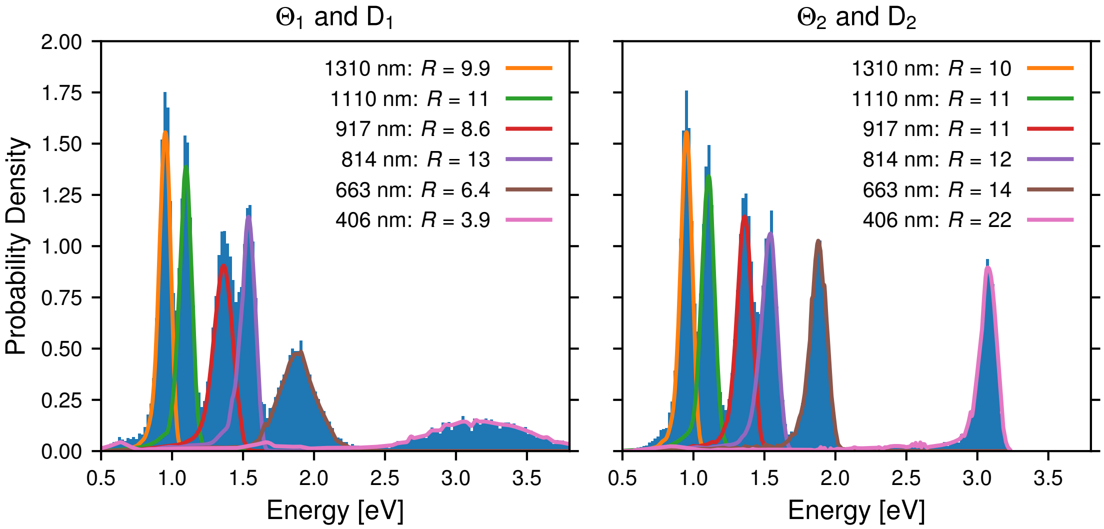

Figure 5.6: The resolving power measurement of a hafnium MKID readout with a TWPA is shown where the original and alternative phase and dissipation coordinates from chapter 3 are used. The Θ_2 and D_2 clearly increase the resolving power of the highest energy photons by removing the unphysical signal compression from the homodyne readout.

turned out to be mostly analysis independent, here we used the simpler photon energy estimation technique discussed in chapter 3 to stay consistent with the rest of the results in this dissertation.

5.2.4 Hafnium Resolving Power Measurements

Hafnium resonators, too, benefit from using a TWPA in their readout chain. As we did for hafnium resonators without a TWPA we see slightly better performance than with $PtSi_x$, primarily because of the longer pulse decay time and higher responsivity. Figure 5.6 shows the measured resolving power of a single pixel in a hafnium detector array designed in the MEC format over a wider energy range than that studied with $PtSi_x$.

Also shown in figure 5.6, is a comparison between the two different phase and dissipation coordinate systems discussed in chapter 3. They both give similar results for the low-

Energy [eV]	Resolving Power [E/ΔE]	
	Measured	Expected
3.03 (406 nm)	22	120
1.87 (663 nm)	14	38
1.52 (814 nm)	12	26
1.35 (917 nm)	11	23
1.27 (979 nm)	11	22
1.12 (1,110 nm)	11	22
0.946 (1,310 nm)	10	18

Table 5.3: The discrepancy between the measured and expected resolving powers for the hafnium detector readout with a TWPA is shown. The expected resolving power based on the noise level is computed using equations 3.17 and 3.23. At the highest energy we see a large increase in the expected R which comes from a boost in the detector responsivity caused by the nonlinear kinetic inductance. This effect is difficult to design detectors around and, as such, should not be taken as a realistic estimate of a typical expected resolving power at this energy. The Θ_2 and D_2 coordinates were used for this analysis.

est energy photons, but at the higher energies a significant amount of signal compression occurs with Θ_1 and D_1. The compression is removed when using the Θ_2 and D_2 coordinates, and the resolving power increases dramatically. For this detector the energy range over which photon energies can be accurately measured was more than doubled by using this coordinate system. These coordinates should be used any time such a wide energy range needs to be measured with an MKID but likely will only work if the noise floor is low enough.

Hafnium detectors also see the same resolving power discrepancy as in platinum silicide. Table 5.3 shows the measured and expected resolving powers across this energy range for the better performing Θ_2 and D_2 coordinates. The difference between our measurements and expectations reach as large as a factor of five at the highest energy tested. The values in table 5.3 differ slightly from those presented in reference 118 even though they are derived from the same dataset. In that paper, a single filter was used for the entire energy range to show that the new coordinate system significantly improves detector linearity. Here, however, we are more interested in the limiting resolving power, so to be consistent with the analyses presented in the rest of this dissertation, we use a different filter for each photon energy.

5.3 Attributions

The TWPA MKID readout and corresponding platinum silicide detector resolving power measurements were the product of work by **N. Zobrist**, B. H. Eom, P. Day, B. A. Mazin, S. R. Meeker, B. Bumble, H. G. LeDuc, G. Coiffard, P. Szypryt, N. Fruitwala, I. Lipartito, and C. Bockstiegel, "Wide-band parametric amplifier readout and resolution of optical microwave kinetic inductance detectors", Applied Physics Letters **115**, 042601 (2019). The subsequent application of this readout scheme to a hafnium detector and the demonstration of the improvement using the alternative coordinate system was done by **N. Zobrist**, N. Klimovich, B. Ho Eom, G. Coiffard, M. Daal, N. Swimmer, S. Steiger, B. Bumble, H. G. LeDuc, P. Day, and B. A. Mazin, "Improving the dynamic range of single photon counting kinetic inductance detectors", Journal of Astronomical Telescopes, Instruments, and Systems **7**, 010501 (2021). Additionally, Neelay Fruitwala's help ensuring that all of the factors of two in the noise equations were in the correct place was invaluable in writing this chapter.

6

Solving the Phonon Problem

The discrepancy between the measured and expected resolving powers for our low noise detectors discussed in chapter 5 must be addressed in order to further improve MKID performance. Based on the superconducting instrumentation community's experience optimizing STJ detectors, it should not be particularly surprising that phonon escape might be the hidden factor limiting MKIDs [39]. We will also present order of magnitude calculations of this effect in this chapter which corroborate that phonon loss is a problem in our detectors. However, an exact theoretical treatment of this form of resolving power degradation is challenging with the materials that we use. Much of the physics that has been developed to describe this effect applies only to BCS superconductors with no gap broadening and requires knowledge of difficult to measure material constants. It will likely be some time before these types of calculations become trustworthy.

In light of these shortcomings, we pursue a more experimental approach to eliminating phonon escape in our detectors. This chapter will focus on one such attempt and show that, despite our ignorance of the exact physics, we need not proceed blindly. We can still remain quantitative about the size of the effect and use that knowledge to further improve our sensors.

6.1 Missing Energy

The phonon limited resolving power of ultraviolet to near-infrared MKIDs is set by the interaction between quasiparticles and phonons in the superconductor. After the energy down-converts from the initial photon absorption event, the leftover phonons that are produced as a side product do not affect the superconductor's surface impedance, so they have effectively disappeared from our measurement system. This missing energy affects the detector's pulse height from which we extract the estimated photon energy, E_{photon}. If the same amount of energy was lost due to phonons during every photon event, we would not take notice. However, since this effect is a statistical process, more missing energy translates into a lower resolving power.

6.1.1 The Fano Limit

The ultimate limiting resolving power for ultraviolet to near-infrared MKIDs is set by the amount of phonons that reach energies lower than 2Δ, at which point they can no longer break Cooper pairs. All other phonons are assumed to eventually convert their energy into quasiparticles and be detected. At the end of this complete downconversion process, roughly 41 % of the initial energy will be contained in these low energy phonons [71]. The exact amount of energy lost in this manner is statistical and sets the maximum achievable resolving power, called the Fano limit [164].

$$R_{\text{Fano}} = \frac{1}{2\sqrt{2\ln(2)}}\sqrt{\frac{\eta_{\text{pb}}E_{\text{photon}}}{\Delta F}} \tag{6.1}$$

Here, η_{pb} and F are the pair breaking efficiency and the Fano factor. We use the standard values 0.59 [71] and 0.2 [165, 166] respectively for each since they are difficult to measure and vary only weakly across most superconductors [71, 164]. The factor of $2\sqrt{2\ln(2)}$ converts the standard deviation to the full-width half-max distribution width. For a detector with a superconducting transition at 500 mK, the Fano limit gives a maximum resolving power of roughly 59 at 2.5 µm and 147 at 400 nm, right in the target range for an exoplanet IFS.

6.1.2 Hot Phonon Escape

In practice, achieving the Fano limit in real detectors has proven difficult. Phonons escaping into the substrate before they fall below the 2Δ energy threshold can significantly reduce the observed resolving power [105, 129, 167]. We account for this excess loss by introducing an extra phonon loss factor, J, into equation 6.1 [168].

$$R_{\text{phonon}} = \frac{1}{2\sqrt{2\ln(2)}}\sqrt{\frac{\eta_{\text{pb}}E_{\text{photon}}}{\Delta(F+J)}} \tag{6.2}$$

After measuring the signal-to-noise contribution to the resolving power, R_{noise}, the total resolving power is given as $1/R^2 = 1/R^2_{\text{noise}} + 1/R^2_{\text{phonon}}$. In this way, J can be estimated for different materials and geometries assuming that there are no other contributions to

R. The photon event absorption position along with a non-uniform current density in the inductor can also contribute to a decreased resolving power, but modeling of these effects suggests that they do not contribute significantly for this design as long as $R \lesssim 40$ [105].

Hafnium has proven to be the best material out of the higher inductance materials tested so far [67, 118]. The breakdown of the noise contributions to R for the hafnium detector from section 5.2.4 shows that athermal phonon escape is the primary factor limiting the resolving power over the tested energy range, corresponding to $J = 13$ and $R_{\text{phonon}} = 13$ at 1 µm. For the platinum silicide results presented in section 5.2.3, we measure $J = 9.3$, giving $R_{\text{phonon}} = 10$ at 1 µm. Although the platinum silicide J value is smaller than that of hafnium, the higher T_c in platinum silicide results in a slightly worse resolving power.

The phonon loss can be partitioned into two contributions, $J = J_{\text{high}} + J_{\text{low}}$, which correspond to the first and subsequent waves of phonons interacting with the substrate boundary respectively. Each of these components can be estimated theoretically, but since both of the formulas for J_{high} and J_{low} are fairly complicated and depend on a lot on hard to estimate parameters, the details of these computations are left to appendix D. We find for hafnium, $J = 6.39$, corresponding to a limiting resolving power of $R_{\text{phonon}} = 18$ at 1 µm. For PtSi_x, $J = 1.89$, which gives $R_{\text{phonon}} = 21$ at 1 µm. These calculated values aren't consistent with our measurements, but they are order of magnitude correct. This level of agreement is to be expected with all of the parameter uncertainties. However, the calculation does indicate that phonon loss is happening in our detectors at levels effecting the resolving power. Even more so, the calculations show that the primary effect is coming from the first wave of phonons near the Debye energy. If we can block those from escaping, we will go a long way toward improving the resolving power.

6.2 Membrane Detectors

The best published MKID resolving powers to-date have been in NbTiN-Al hybrid coplanar waveguide resonators suspended on silicon nitride membranes [167]. Compared to that of a device on a thick substrate, the membrane device had a higher resolving power, corresponding to a decrease in J by a factor of about 8, from 3.1 to 0.38. The much thinner membrane allows partially escaped phonons to be quickly recollected in the sensor before reaching the substrate. The extra chance to down convert into quasiparticles and be detected increases the average time required for phonons to fully escape, τ_{esc}, and results in a higher resolving power. This improvement was shown to be consistent with a simple geometric ray-tracing phonon model, which used the proportionality of J to the ratio between the phonon pair breaking time and the escape time, $\tau_{\mathrm{pb}}/\tau_{\mathrm{esc}}$, to evaluate the expected decrease in J. These values for J are smaller than that for hafnium on sapphire, but because of hafnium's lower gap energy, the limiting resolving power is similar for the non-membrane devices.

While the membrane devices give an impressive increase in R, it introduces significant fabrication complexity. Additionally, the aluminum sensor used in that demonstration is small, highly reflective of ultraviolet to near-infrared photons [169], and has a low kinetic inductance, which makes it difficult to create large arrays with high quantum efficiency. A more realistic detector design for a kilo- or mega-pixel detector requires a more disordered superconductor with a higher kinetic inductance that can be patterned into a compact lumped element circuit like shown in figure 1.3. The lumped element design allows for light to be focused onto the inductor with a microlens array making fill factors of >90 % possible.

Despite being impractical, the achieved resolving powers of 28 at 1 μm and 52 at 400 nm are such a large leap above the performance of previous devices that phonon escape can no longer be ignored as a source of noise in MKIDs. In order to achieve similar performance, we need to emulate this phonon blocking strategy with a detector geometry suitable for astrophysical observations.

6.3 Phonon Blocking Layer

To decrease J without a membrane, some form of phonon blocking layer must be introduced between the photo-sensitive superconductor and substrate. This layer may take the form of a material with an acoustic impedance very different from either the substrate or sensor material. In this case, phonons would preferentially be reflected back into the sensor allowing for more opportunities to break Cooper pairs into quasiparticles before falling below the 2Δ threshold.

6.3.1 Effective Phonon Transmission

To evaluate the performance of this kind of high impedance layer, we use the angle averaged phonon transmission from material i to adjacent material j defined by the appropriate combination of the transmission coefficients for longitudinal and transverse phonons [170].

$$T_{ij} = \left(\frac{2T_{t,ij}}{3c_{t,i}^2} + \frac{T_{l,ij}}{3c_{l,i}^2}\right)\left(\frac{2}{3c_{t,i}^3} + \frac{1}{3c_{l,i}^3}\right)^{-2/3} \tag{6.3}$$

Here c corresponds to the speed of sound and the t and l subscripts specify the corresponding transverse or longitudinal phonon mode. The average reflection coefficient can be found with $R_{ij} = 1 - T_{ij}$.

To compute the effective transmission from material 1, through material 2, and into material 3, we add up all of the transmission and reflection paths that result in a phonon entering material 3, assuming no phonon coherence across the structure. This procedure results in the following formula:

$$T_{13} = T_{12}T_{23}\sum_{i=0}^{\infty}\left(R_{23}R_{21}\right)^i . \tag{6.4}$$

Table 6.1 contains all of the material parameters used to compute the transmission coefficients from the acoustic mismatch model and the effective transmission through an interface defined by equation 6.4. An example of this kind of high impedance layer might be a low density polymer like PMMA, which according to the acoustic mismatch model presented here would reduce the effective phonon transmission coefficient into the sapphire by a factor of 3.1 [170, 171]. Since J is roughly proportional to the transmission coefficient, we might expect as much as a 70 % improvement in R_{phonon} with this method.

Material	density $\left[\mathrm{g\,cm^{-3}}\right]$	c_t $\left[\mathrm{m\,s^{-1}}\right]$	c_l $\left[\mathrm{m\,s^{-1}}\right]$
Hafnium	12.781	2,053	3,786
Indium	7.47	904	2,700
Silicon	2.33	5,340	8,980
Sapphire	3.99	6,450	10,900
PMMA	1.18	1,400	2,757

Table 6.1: Material parameters used in the acoustic mismatch calculations. All data were taken from reference 170 with the exception of those for hafnium and PMMA which were found in reference 172 and 173 respectively and correspond to room temperature measurements.

6.3.2 Low Debye Energy Interfaces

Amorphous-insulating blocking layers like PMMA are another potential source of loss, though, and should be kept away from the MKID capacitor to avoid excess two-level system noise [152]. Since most of the escaping phonons contributing to J have energies near the Debye energy of the sensor material, a potential alternative, then, is to find a metallic, preferably superconducting, layer that has a low enough Debye energy to not have any available phonon states in that energy regime.

Out of the available elemental low Debye energy superconductors, indium and lead stand out as the easiest with which to fabricate devices. Both have effective phonon cutoff energies much lower than that of hafnium: the Debye temperature of indium and lead, 112 K and 105 K respectively, are roughly half of that of hafnium, 252 K [51]. We chose to proceed with indium as it was more readily available at the time.

Unlike with PMMA, adding an indium interface layer would result in only a ~18 % decrease in the effective transmission coefficient according to the acoustic mismatch model. The highest energy phonons produced in the hafnium, though, should be unable to escape into the indium below because of the low Debye energy. These phonons have a wave-

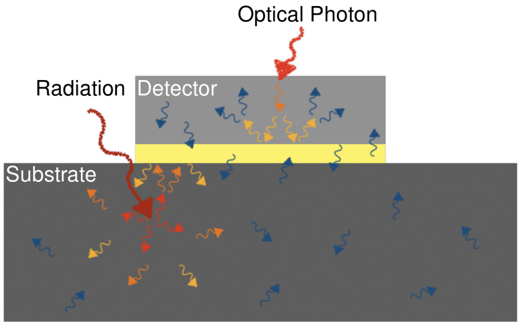

Figure 6.1: A schematic representation is shown of the phonon blocking layer (yellow) employed in this paper. The lack of available phonon states in the blocking layer prohibits high energy phonons (red and orange) generated during a photon absorption from escaping the detector material, allowing all of their energy to be measured. Lower energy phonons (blue) pass through the barrier without significantly more scattering than if the barrier were not present. Similarly, the phonon blocking layer provides some protection to the detector from high energy events in the substrate from high energy radiation.

length on the order of the hafnium lattice spacing, ~0.3 nm, so indium films that are tens of nanometers thick should provide an effective barrier.

Similar types of multilayers with mismatched Debye temperatures have been previously fabricated to produce low thermal conductivity films at room temperature [174]. Because at higher temperatures the contribution of Debye phonons is important, these systems are effective at limiting the quasi-equilibrium heat transfer across the film boundary. Work with these multilayers shows that the simple considerations used here to choose an interface material are likely inadequate for fully describing the phonon transport. The amorphous nature of these films and the presence of the interface, for example, alter the fundamental properties of the phonons [175]. However, we will continue to use these simple models as order of magnitude estimates, noting that the future design of this kind of interface layer would benefit from a more detailed analysis.

This type of interface layer is an interesting tool for manipulating phonon dynamics at low temperatures and may have uses in other types of devices. As shown in figure 6.1, it acts as a selective valve, preventing highly non-equilibrium phonons from crossing the barrier, while allowing passage for low energy phonons which help keep the device in thermal equilibrium with the substrate. We use it here to keep high energy phonons inside of our detector, but the interface layer should also provide protection to the device from absorbing high energy phonons generated in the substrate. One potential source of these phonons is from ionizing radiation, like cosmic rays, which cause detector glitches and lead to a significant increase in dead time in superconducting bolometers [176]. These types of events also pose problems for quantum computers by destroying qubit coherence and increasing error rates [177]. This problem may be partially mitigated by implementing a similar interface layer in the respective devices.

6.3.3 Device Description

To demonstrate the phonon blocking effect, we fabricated a hafnium / indium bilayer MKID on silicon. Silicon was chosen as a substrate to encourage more uniform indium films, but we note that thin layers of indium can be deposited on sapphire if the substrate is cooled to liquid nitrogen temperatures [178]. The tested bilayer was comprised of a 15 nm layer of indium with 220 nm of hafnium on top. The silicon wafer is mounted into the vacuum chamber of a thermal evaporator. Indium drops are placed into a tungsten crucible and the system is pumped down to a base pressure of 3×10^{-6} Torr where the indium is evaporated onto the substrate.

The substrate is then transferred into a ultra high vacuum AJA ATC-2200 sputter deposition chamber and the hafnium is deposited on top of the indium. The hafnium deposition process is described fully in reference 134, but we use a different sputter target. The target is >99.95 % hafnium by weight of the 79 elements sampled excluding zirconium. Zr, O, C, N, Ta, Fe, H, Nb, Al, Si are all 700, 60, 10, <10, <5, 1.5, <0.5, 0.25, 0.24, 0.21 wt% respectively. All other elements are ≤0.14 wt%.

The wafer then goes through a single step of lithography consisting of the definition of the MKID resonators. 80 nm of DUV-42P6 adhesion promoter is spun on the wafer followed by 800 nm of imaging UV6-0.8 photoresist. The MKID geometry is patterned with the same stepper and the indium/hafnium bilayer is etched in a PlasmaTherm SLT 700 reactive ion etcher in a BCL_3/Cl_2 environment (60 sccm / 40 sccm, 5 mTorr, 100 W). Finally, the resist is removed with solvents and gold bond pads are added via a lift off process on the side of the chip to ensure good thermalization of the device. The wafer is then diced into chips of dimension 13 mm × 13 mm.

Between the deposition of indium and hafnium, the sample is exposed to atmosphere. A small uncharacterized oxide layer may form which is not considered in the phonon transport calculations in this chapter. Future work might investigate if removing this layer has a significant impact on the detector resolving power.

6.3.4 Bilayer Proximity Effect and T_c

We measure $T_c = 468$ mK for hafnium on silicon and 786 mK for the bilayer on silicon indicating that the thin indium layer has a strong effect on the superconducting properties of the film. Luckily, 786 mK is still within the sub-Kelvin value range needed for this type of detector, so we should not be too concerned. At most, the detector thickness will

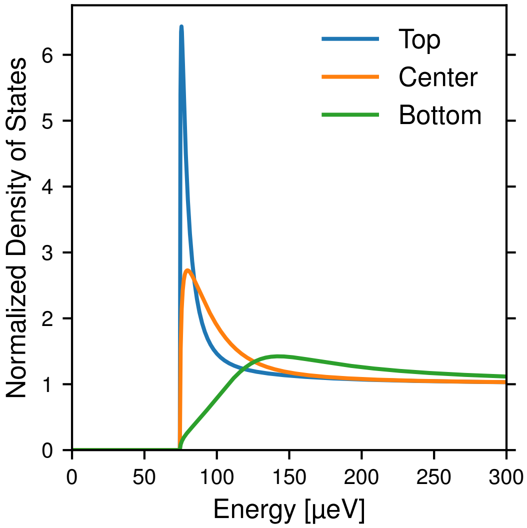

Figure 6.2: The normalized density of states for three vertical positions along the bilayer are plotted. *Top* corresponds to the side of the film furthest from the substrate while *Bottom* refers to the interface between the indium and hafnium. The density of states of the hafnium near the interface and all of the indium is indistinguishable from the *Bottom* curve. The density of states in the *Center* of the bilayer film is also shown for comparison.

need to be tuned in the future to compensate for the slight decrease in responsivity. As the hafnium is already fairly thick, we can be confident that this issue will not constrain detector performance.

To try to explain this variation in T_c we calculate how the density of states in the film changes due to the proximity effect. We use a numerical simulation based on the Usadel equations, discussed in section 2.1.2, to calculate the density of states as a function of vertical position in the film to verify that it has a single gap energy [69]. Figure 6.2 shows the results of this computation using the parameters defined in table 6.2 and assuming zero boundary resistance. The film does have a single gap energy despite significant variation in the density of states. The predicted variation in the density of states does not effect detector performance because the size of the diffusion constant in each material results in a uniform vertical distribution of quasiparticles on µs timescales for this detector thickness. However, the calculation shows that the film transition temperature should only increase by a few mK when adding the thin indium layer which does not match our measurements. This is somewhat expected because of the uncertainty in the hafnium T_c which depends strongly on the film stress and substrate used [134]. We should expect, then, that the bilayer T_c will be as controllable as that of hafnium by changing the deposition parameters.

Material	d [nm]	ρ @ 4 K [$\mu\Omega$ cm]	Θ_D [K]	T_c [K]	N_0 $\left[J^{-1}\,m^{-3}\right]$	D $\left[cm^2\,s^{-1}\right]$
Hafnium	220	60.6	252	0.468	1.23×10^{47}	5.24
Indium	15	0.0973	112	3.3	8.78×10^{46}	4,570

Table 6.2: The layer thicknesses, resistivities, Debye temperatures, transition temperatures, single-spin density of states, and diffusion constants used in the proximity effect numerical simulation are tabulated here. The single-spin density of states includes the phonon enhancement factor and was computed using the data from reference 51 and the densities presented in table 6.1. The diffusion constant was computed using $D={}^{1}/_{\rho N_0 e^2}$ [179]. All other parameters were measured directly from films deposited on silicon wafers with deposition parameters matching those used to make the bilayer.

6.3.5 Resonator Measurements

Resonators patterned out of the bilayer material had internal quality factors of up to 250,000, which are similar to the quality factors achieved in hafnium alone [134]. We also found that the quasiparticle lifetime increased when the indium was added. However, it can be difficult to extract the exact quasiparticle lifetime in a superconductor based on a photon response. The quasiparticle recombination rate is quadratic in the total number of quasiparticles, which results in a pulse shape that transitions from a hyperbolic to exponential decay over time. The functional form for this decay was worked out in reference 180.

$$X(t) = \frac{A}{[1 + {}^{1}/_{x_{\mathrm{qp}}(0)}] \exp\left({}^{t}/_{\tau_{\mathrm{qp}}}\right) - 1} \tag{6.5}$$

Here, X is either the phase or dissipation response. t is time. A is a scaling parameter relating the fractional quasiparticle density at the beginning of the pulse, $x_{\mathrm{qp}}(0)$, to X. τ_{qp} is the quasiparticle lifetime at zero quasiparticle density.

τ_{qp} differs from the pulse decay time presented for hafnium in reference 67, for example, because it is not a time constant representative of the pulse as a whole but rather of the tail end of the pulse. Figure 6.3 shows the fits to the average pulse in each quadrature of the signal to this model. We choose to limit the fit to data less than half of the pulse peak to minimize the effect of the finite resonator ring up time on the results. The fit parameters and their statistical uncertainties are given in table 6.3.

The recombination times and initial fractional quasiparticle densities in each quadrature do not align. This effect indicates that not all quasiparticle states contribute equally to the phase and dissipation response. A similar observation has been made for titanium nitride detectors [64]. The lifetime in the dissipation signal changes the most in our data, which we suspect may be attributable to the larger high energy phonon density inhibiting quasiparticle relaxation into localized, dissipationless states.

Film	Response	τ_{qp}	x_{qp}
Hafnium	Phase	404 ± 6.3	21.6 ± 0.42
	Dissipation	106 ± 1.7	5.6 ± 0.15
Bilayer	Phase	452.4 ± 0.55	1.010 ± 0.0044
	Dissipation	401.3 ± 0.48	1.585 ± 0.0053

Table 6.3: The fitted values for the quasiparticle lifetime and initial quasiparticle fractional density along with their 1-σ uncertainties are tabulated for the phase and dissipation directions.

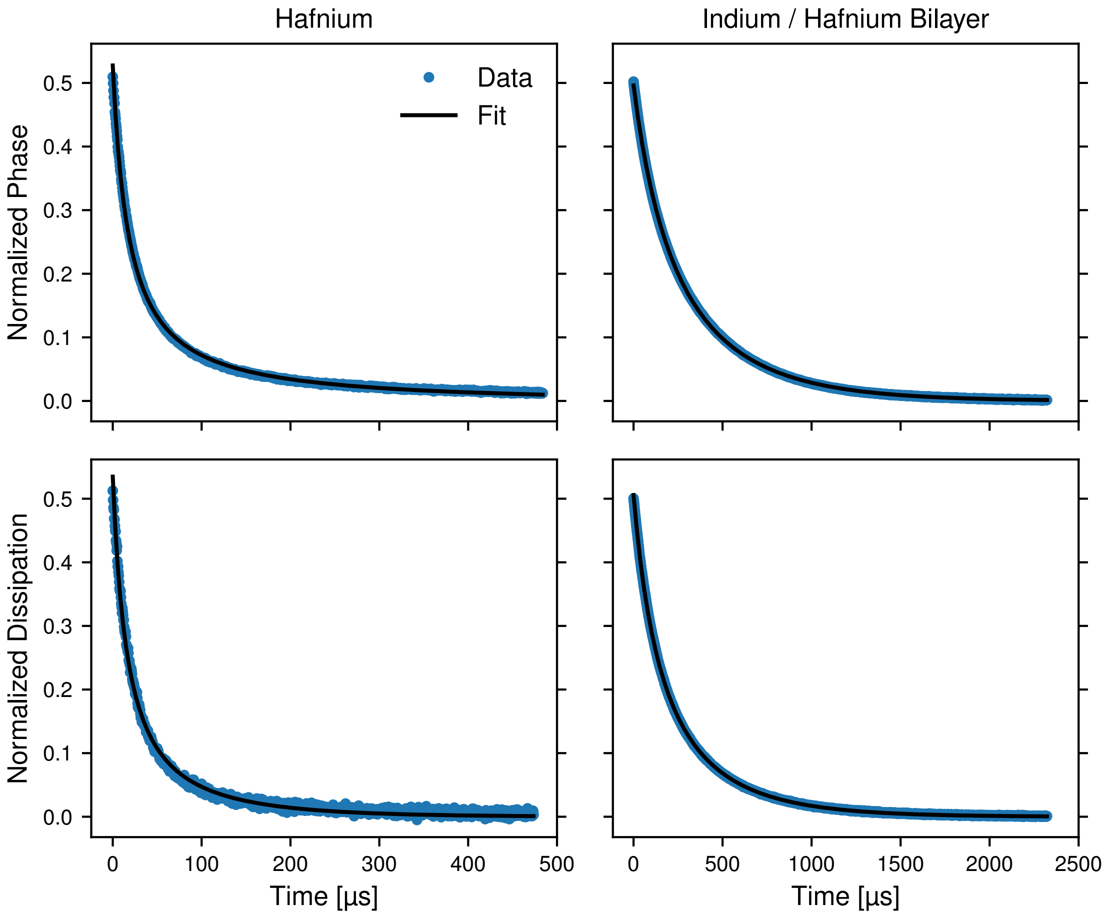

Figure 6.3: Fits to the average pulse decay in the phase and dissipation quadratures are shown for both the hafnium film and hafnium bilayer. Each pulse response is normalized to its pulse height.

Figure 6.4 shows a dramatic improvement in the resolving power from 11 to 20 at 1 μm in the bilayer devices. From this data, we calculate $J = 1.6$ corresponding to a 8 times improvement in phonon trapping over the original device, similar to the improvement seen by suspending an MKID on a membrane. The full noise breakdown of this device and the hafnium device from section 5.2.4 are also shown in figure 6.5 and have been extrapolated to higher and lower wavelengths as a guide to how these detectors are likely to perform outside the tested wavelength range. For the bilayer device above 1 μm, the resolving power is strongly limited by the signal to noise of the photon pulse, while below

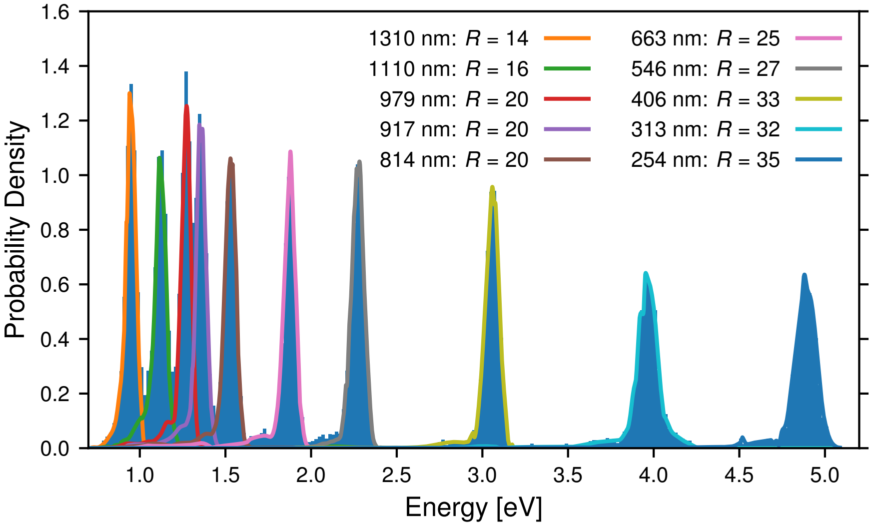

Figure 6.4: The combined spectra are shown for the bilayer device resolving power measurement. We see a large improvement in the resolving power when compared to previous measurements with just hafnium films like in figure 5.6.

1 µm phonon escape becomes the limiting term in the resolving power.

6.3.6 Expected Phonon Trapping Improvement

If the increase in energy resolution were from only the acoustic mismatch introduced by the indium layer, we could compute the expected increase in R using the phonon ray-tracing model developed in reference 167. We employ a similar model to calculate the phonon escape time, τ_{esc}. The geometry is assumed to be a 2 µm wide rectangle with infinite length. The hafnium thickness is 220 nm and the indium thickness is 15 nm. Phonons are emitted in random directions from the top of the film with equal probability for each phonon mode. When a phonon hits an interface it is either transmitted at a new direction determined by Snell's law or reflected. If reflected, diffuse scattering is assumed and a random direction is chosen. Care is taken at the interfaces to calculate the probability of mode conversion between transverse and longitudinal phonons according to the acoustic

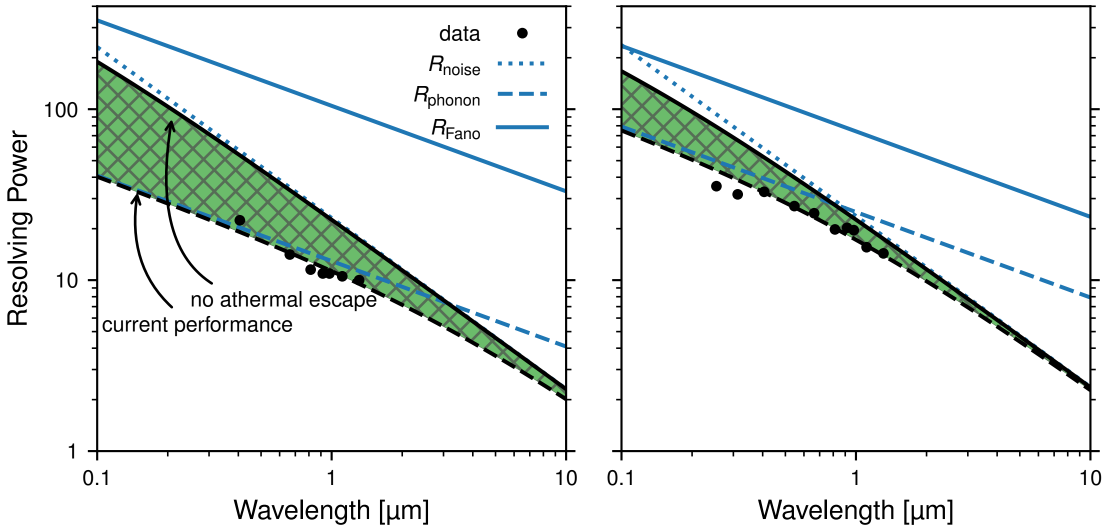

Figure 6.5: *Left:* The noise decomposition for the hafnium device discussed in section 5.2.4 is shown. The filled in green area represents the resolving powers achievable by reducing the phonon loss but keeping the same noise spectrum. *Right:* The same breakdown is shown for the hafnium / indium bilayer device. The phonon component to the resolving power is significantly improved.

mismatch model [170]. τ_esc is computed by keeping track of the time required for each phonon to enter the substrate and averaging that time for 10,000 different starting conditions.

We find that $\tau_\mathrm{esc} \sim 12\,\mathrm{ns}$ for both hafnium on sapphire and the bilayer on silicon. The ratio of J in the hafnium film to that in the bilayer is given by

$$\frac{J_\mathrm{Hf}}{J_\mathrm{Bi}} = \frac{\tau_\mathrm{esc,\,Bi}}{\tau_\mathrm{esc,\,Hf}} \sim 1. \tag{6.6}$$

We expect effectively no change in J, which is consistent with the similar effective transmission to the substrate between the two devices that was computed earlier from the acoustic mismatch model. With the higher gap energy in the bilayer and if the acoustic mismatch were the only effect, these results suggest that the bilayer should have worse resolving power than that of the hafnium device. Since this is not the case, we infer that an alternative mechanism must be preventing phonon transmission.

To investigate the effect of the lower Debye energy of indium, we need to take into account the physics of the full energy down-conversion process. Unfortunately, sputter deposited thin film hafnium differs significantly from bulk hafnium. The thin film transition temperature is a factor of 4 higher than its bulk value [134]. It also is a very disordered material resulting in an anomalously high normal state resistivity [131]. With this in mind, it is unsurprising that the material constants for hafnium provided in reference 71 do not provide sensible answers when calculating the phonon loss factor, J. We do, however, expect that the general picture of the energy down-conversion and phonon loss still apply [129, 168]. Using the formulas from these references, we can put bounds on our expected change in J when the hafnium bilayer is introduced.

Although the calculated value for J in hafnium are not consitent with the measured value, we can estimate the improvement that we expect to see by looking at the dependence of J on the Debye energy. Since we are only looking at phonon energy scaling we can ignore any constant or weakly energy dependent terms in equation D.1 to get the proportionality

$$J_{\text{high}} \propto \int_0^{\Omega_{\text{D}}} d\epsilon \epsilon^3. \tag{6.7}$$

This proportionality becomes exact in the large film thickness limit, $d \gg l_{\text{pb}}(\epsilon)$, which is true over much of the energy range in question. The integral sums up the contributions to the energy uncertainty from phonons with energies between 0 and the Debye energy, Ω_{D}.

Introducing an interface layer would lower the upper bound on this integral to the Debye energy of the interface. However, all other references to the Debye energy in the equation for J_{high} should remain unchanged since the energy scale of the phonon distribution is set by the acoustic properties of the hafnium film. Taking the Debye temperature of indium to be 112 K and the Debye temperature of hafnium to be 252 K [51], we find

$$\frac{J_{\text{high}}^{\text{Hf}}}{J_{\text{high}}^{\text{Hf, In}}} = 26. \tag{6.8}$$

We expect a significant reduction in the amount of energy loss from this first generation of phonons by introducing the indium layer. We should note that because of the power of 4 energy scaling, these results are very sensitive to the exact values used for the Debye energies which may be different from their bulk values in the thin film case.

The effect of successive generations of phonons are more difficult to account for. The energy dependence of J_{low} is contained in the function $g_1\left({}^{\Omega_D}/_{\Omega_1}\right)$ from appendix D. Ω_1 is the transition energy from a phonon dominated down-conversion to a quasiparticle dominated down-conversion. Therefore, the energy scaling can not be disentangled from Ω_1. Using the Ω_1 given in reference 71, we find

$$\frac{J_{\text{low}}^{\text{Hf}}}{J_{\text{low}}^{\text{Hf, In}}} = 1.7. \tag{6.9}$$

This value is consistent with less lower energy phonons being blocked by the difference in Debye temperature.

Since we do not know the relative contributions of J_{high} and J_{low}, these two values put bounds on the improvement to the total phonon loss factor, which is consistent with the measured improvement of 8.

$$1.7 < \frac{J^{\text{Hf}}}{J^{\text{Hf, In}}} < 26. \tag{6.10}$$

This model is consistent with our data. However, more work needs to be done to understand the exact phonon material parameters for these films to make more accurate estimates.

6.4 Attributions

The design of the indium phonon blocking layer and the measurement of the improved resolving power was the product of work by **N. Zobrist**, W. H. Clay, G. Coiffard, M. Daal, N. Swimmer, P. Day, and B. A. Mazin, "Membrane-less phonon trapping and resolution enhancement in optical microwave kinetic inductance detectors", 2022, arXiv:2204.13669 [astro-ph.IM]. W. Hawkins Clay deserves special thanks for his help replicating the acoustic mismatch model from reference 170 and ensuring that the output was consistent with the paper.

7

Conclusions

Current exoplanet IFSs operating in the ultraviolet to near-infrared wavelength range rely on established semiconductor based technologies. EMCCDs are used for the shorter wavelengths while HgCdTe detectors are used for the longer wavelengths. However, both of these technologies suffer from readout noise which would limit our exoplanet detection ability in a potential space-based mission [24]. A true photon counting detector that could simultaneously measure a planet's spectra over this whole wavelength range would greatly expedite and enhance our understanding of exoplanets. In addition to simplifying the required optics needed to support multiple non-energy resolving detectors, photon counting opens the door for powerful new methods which allow us to detect exoplanets in increasingly difficult conditions [27, 28].

To achieve this goal we turn to superconducting detectors, which exhibit exquisite sensitivity and readout speed. STJ and TES detectors, among others, showed promising initial results but lack the ability to scale to mega-pixel instruments. MKIDs solve this problem with their unique frequency multiplexed design and kilo-pixel versions have already

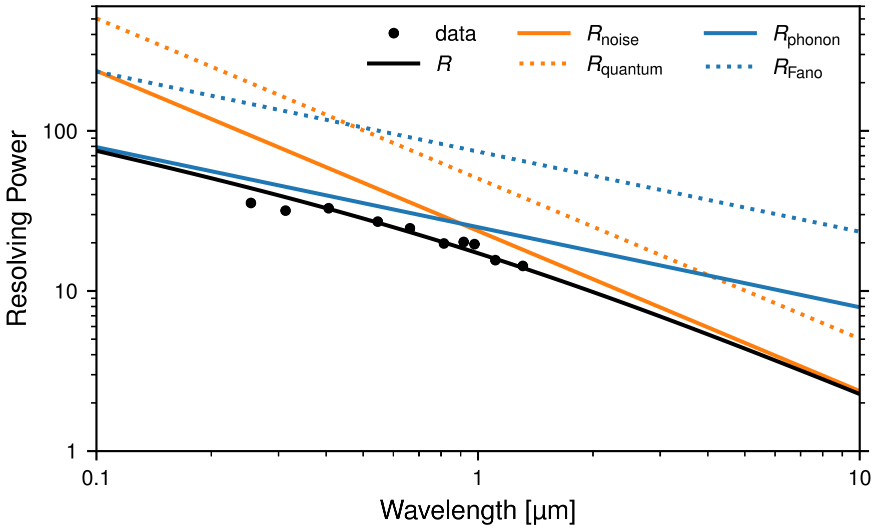

Figure 7.1: The resolving power of the best performing MKID presented in this dissertation is shown with its components broken down into phonon and noise contributions. Were we to make a similar detector with no TLS noise and a fully quantum limited readout, the noise contribution would approach R_{quantum}. Similarly, eliminating all of the excess phonon loss from the device would set the phonon contribution to R_{Fano}

been fielded at several telescopes around the world [45–47]. The primary challenge to prove the utility of this technology is demonstrating resolving powers that are compatible with the exoplanet characterization targets. At a minimum, a resolving power of 20 is required to resolve water in an exoplanet's atmosphere. However, considering all of the different molecules that we would like to search for, $R = 100$ is a sensible target for this type of instrument [23].

This dissertation covered several strategies for improving the resolving power of MKIDs. We paid careful attention to the analysis used to estimate photon energies in chapter 3, changed the resonator material in chapter 4, created a significantly lower noise environment in chapter 5, and introduced a new type of phonon blocking layer in chapter 6. These improvements resulted in increasing the resolving power of these detectors from 7 to 20 at 1 µm, reaching the minimum requirements for an exoplanet IFS.

Figure 7.1 summarizes these results and shows where we need to focus for further improvements. At the shorter wavelengths, the resolving power is still limited by phonon loss. The results of the membrane suspended MKIDs show that we can continue to make progress on this front by investigating new phonon blocking strategies [167]. At the longer wavelengths, detector noise limits the performance. By focusing on fabrication improvements, the two-level system noise can be reduced. Combined with reducing the noise from the parametric amplifier readout, these detectors may be able to reach the quantum-limited noise floor. However, unlike the Fano limit for phonons, this amplifier noise limit is not fundamental since detector designs that can handle higher readout powers may be employed to achieve even lower phase and dissipation noise.

These results predict a bright future for ultraviolet to near-infrared MKIDs, but there is still much to be done before they reach their full potential. In addition to further pushing the resolving power, the readout technologies that we use must be upgraded so that they can take advantage of this extra sensitivity at scale. Array uniformity and increasing pixel yield must also become a priority to ensure that the performance shown here is representative of an entire detector array. As such, the field of MKID development remains an exciting platform for the exploration of low temperature, superconducting physics and microwave electronics.

A

Fourier Transform

The analysis of MKID data often makes use of the Fourier transform. Unfortunately, there exists an ambiguity in its definition, so we need to explicitly state which convention is used here. The distinction between the continuous and discrete versions of the transform is also explained. Throughout this dissertation the continuous version is used to derive and discuss results, while the discrete version is only employed when operating on real data.

Details about Fourier transform algebra and associated theorems will not be covered here as they are throughly discussed in many introductory texts. A good review can be found in reference [117, §B.2].

A.1 Continuous Definitions

The Fourier transform pair will be defined by

$$\begin{aligned} \tilde{y}(f) \equiv \quad \mathcal{F}_t[y(t)](f) &\equiv \int_{-\infty}^{\infty} dt\, e^{-2\pi i f t}\, y(t) \\ y(t) \equiv \mathcal{F}_f^{-1}[\tilde{y}(f)](t) &\equiv \int_{-\infty}^{\infty} df\, e^{2\pi i f t}\, \tilde{y}(f). \end{aligned} \tag{A.1}$$

The convolution operator is related to the Fourier transform and will also be used. It is sometimes taken over different bounds, so we define it explicitly here.

$$[x * y](t) \equiv \int_{-\infty}^{\infty} dt'\, x(t')\, y(t - t') \tag{A.2}$$

A.2 Discrete Definitions

The formulas presented above are valid for continuously sampled functions with infinite extent. In practice, we can only digitize our data at a discrete sample rate, f_s, and for a finite time, T. The Discrete Fourier Transform (DFT) is used as an analog to the continuous version, and all of the results above hold as long as the signal being transformed is T-periodic and continuous over all time. These assumptions are true for long pulse records, but may break down if pulse records get too short. If these conditions are not met, the presented algorithms may underperform significantly [109].

To convert the above equations to the discrete case we make the identifications

$$\begin{aligned} dt &\longrightarrow \Delta t = \frac{1}{f_s} \\ t &\longrightarrow t_m = m\Delta t = \frac{m}{f_s} \\ df &\longrightarrow \Delta f = \frac{f_s \Delta t}{T} = \frac{f_s}{N} \\ f &\longrightarrow f_k = k\Delta f = \frac{k f_s}{N}, \end{aligned} \tag{A.3}$$

where N are the number of data points in the signal. Setting $f_s \longrightarrow 1$, the discrete Fourier transform pair becomes

$$\begin{aligned} \tilde{y}_k \equiv \; \mathcal{F}_m\big[\{\, y_m \,\}_N\big](k) &\equiv \sum_{m=\lceil -N/2 \rceil}^{\lceil N/2-1 \rceil} e^{-2\pi i \frac{mk}{N}} \; y_m \\ y_m \equiv \mathcal{F}_k^{-1}\big[\{\, \tilde{y}_k \,\}_N\big](m) &\equiv \frac{1}{N} \sum_{k=\lceil -N/2 \rceil}^{\lceil N/2-1 \rceil} e^{2\pi i \frac{mk}{N}} \; \tilde{y}_k . \end{aligned} \tag{A.4}$$

$\{\, \cdot \,\}_N$ represents a digitized set of N samples, and the set indices are taken so that t_0 and f_0 are roughly in the middle of the trace. The corresponding convolution is then

$$[x_m * y_m]_N(k) \equiv \sum_{m=\lceil -N/2 \rceil}^{\lceil N/2-1 \rceil} x_m \; y_{k-m} . \tag{A.5}$$

The sample rate is set to unity in equations A.4 and A.5 because it is arbitrary for a discrete signal. This convention conforms to that of most modern programing languages like Python’s Numpy. Unfortunately, the omission leads to problems with units when using the DFT as a direct substitution for the Fourier transform. In particular, when generating noise from a power spectrum with the correct units, equation 3.7 must be modified to

$$\vec{n}_m = \mathcal{F}_k^{-1}\left[\left\{ \sqrt{\mathbf{S}(f_k)\ f_s\ N}\begin{pmatrix} e^{i\phi_{\theta_k}} \\ \\ e^{i\phi_{d_k}} \end{pmatrix}\right\}_N\right](m). \tag{A.6}$$

The equations 3.20 and 3.22 for the variance must also be changed to

$$\mathrm{E}\left[\mathrm{Var}\left[\hat{E}\right]\right] = f_s\ N\left[\sum_{\substack{k=\lceil -N/2\rceil,\\ k\neq 0}}^{\lceil N/2-1\rceil} \frac{\partial\tilde{\vec{m}}_k^{\dagger}\left(\vec{\xi}_0\right)}{\partial E}\ \mathbf{S}^{-1}(f_k)\ \frac{\partial\tilde{\vec{m}}_k\left(\vec{\xi}_0\right)}{\partial E}\right]^{-1}\Bigg|_{\hat{E}} \tag{A.7}$$

and

$$\mathrm{Var}\left[\hat{A}\right] = f_s\ N\left[\sum_{\substack{k=\lceil -N/2\rceil,\\ k\neq 0}}^{\lceil N/2-1\rceil} \tilde{\vec{s}}_k\ \mathbf{S}^{-1}(f_k)\ \tilde{\vec{s}}_k\right]^{-1}. \tag{A.8}$$

B

Resonator Equation Derivations

B.1 Asymmetric Shunt Resonator Equation

The steady state transmission through any two port device can be described by its frequency-dependent forward scattering matrix element $S_{21}(f)$ [96, §4.3]. For a shunt coupled resonator, this function has a standard formula, which we will re-derive here to highlight its universality and to make explicit some results that will be needed later.

Figure B.1 shows the form of the impedances assumed for this circuit. All are allowed to be complex and frequency dependent but must not have any zeros in the considered frequency range—except for a first order zero in the imaginary part of Z_3 at the resonance frequency, $\bar{f}_r$. In practice these assumptions are rarely violated for high-quality-factor superconducting resonators since $\left|f - \bar{f}_r\right| \ll \bar{f}_r$ holds for all relevant frequencies and both $Z_1(f)$ and $Z_2(f)$ vary slowly over this range.

The scattering matrix element can be written down immediately from the circuit's

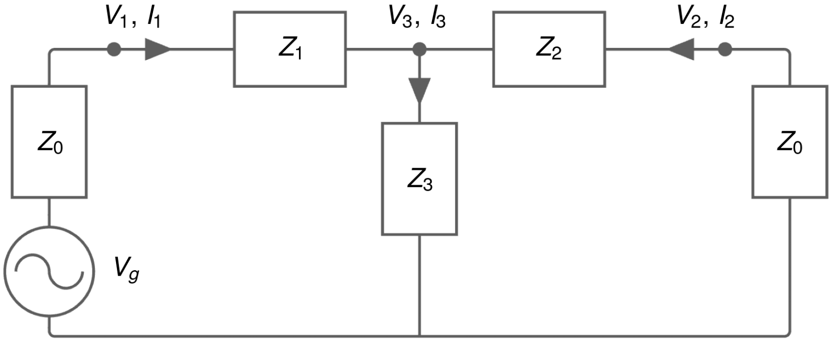

Figure B.1: Shown is a general impedance diagram of resonator (Z_3) shunt coupled to a transmission line (Z_0). Two additional impedances, Z_1 and Z_2, are included to model impedance mismatches caused by imperfect connectors or wire bonds.

ABCD parameters.

$$\begin{aligned} S_{21} =& \frac{2Z_0Z_3}{Z_3(2Z_0 + Z_1 + Z_2) + (Z_0 + Z_1)(Z_0 + Z_2)} \\ =& \frac{2Z_0}{2Z_0 + Z_1 + Z_2}\left(1 - \frac{1}{1 + {}^{2Z_3}/_{\bar{Z}_0}}\right) \end{aligned} \tag{B.1}$$

We have introduced an equivalent characteristic impedance,

$$\bar{Z}_0 = 2\frac{(Z_0 + Z_1)(Z_0 + Z_2)}{2Z_0 + Z_1 + Z_2}, \tag{B.2}$$

that takes into account any impedance mismatch caused by Z_1 and Z_2. The term before the parentheses in equation B.1 is just a scale factor and/or a rotation. Since external components and amplifiers in the readout chain will add their own scaling, we will ignore it for now by defining $\bar{S}_{21}$ to be the term in the parentheses.

Equation B.1 can be written in more useful terms by expanding each term to its lowest order in the generator frequency, f_g, and writing everything in terms of real variables.

$$\begin{aligned} Z_3 =& R_3 + 2\pi i L_3 (f_g - \bar{f}_r) \\ \bar{Z}_0 =& R_0 + iX_0 \end{aligned} \tag{B.3}$$

Now,

$$\bar{S}_{21} = 1 - \frac{\frac{R_0 + iX_0}{2R_3 + R_0}}{1 + 4\pi i \frac{L_3}{2R_3 + R_0}\left(f_g - \bar{f}_r + \frac{X_0}{4\pi L_3}\right)}. \tag{B.4}$$

The imaginary part of $\bar{Z}_0$ has two effects. It slightly modifies the resonance frequency to $f_r = \bar{f}_r + \delta f_a$, where $\delta f_a = {-X_0}/{4\pi L_3}$, and it rotates $\bar{S}_{21}$ around $1 + 0i$ in the complex plane. Neither outcome occurs in the simplest case when $Z_1 = Z_2 = 0$ and Z_0 is real, so it is important to allow for this possibility when using this equation to fit real data.

To bring equation B.4 into a more familiar form, we make the identifications $R_3 \to {2\pi L_3 f_r}/{Q_i}$, $R_0 \to 2\pi L_3 f_r ({1}/{Q_c} - {1}/{Q_i})$, and $X_0 \to -4\pi L_3\, \delta f_a$.

$$\begin{aligned} \bar{S}_{21} =& 1 - \frac{{Q}/{Q_c} - 2iQx_a}{1 + 2iQx_g} \\ =& \frac{Q_c + 2iQ_iQ_c(x_g + x_a)}{Q_i + Q_c + 2iQ_iQ_cx_g} \end{aligned} \tag{B.5}$$

Here, $x_g = {(f_g - f_r)}/{f_r}$ is the fractional detuning of the generator frequency from resonance, and $x_a = {\delta f_a}/{f_r}$ is the fractional detuning of the original resonance frequency due to the asymmetry of the loop.

This equation has been derived by several authors for both specific and more general cases, but they often differ in the exact parameterization used for δf_a [97, 98]. Here, we follow the form used by Geerlings [97, §A.1] since x_a should not depend on Q_i or f_r

which is important for using equation B.5 for modeling the resonator response.

To include the effects of the cabling, attenuators, and amplifiers that are connected to the circuit in figure B.1, we multiply $\bar{S}_{21}$ by an arbitrary gain, $g_0 + g_1 x_m + g_2 x_m^2$, and phase, $\phi_0 + \phi_1 x_m$ [99], where $x_m = {}^{(f_g - f_m)}/_{f_m}$. The generator frequency is referenced to a frequency, f_m, in the middle of the measurement range to make the coefficients unit-less. Both of these terms also absorb the pre-factor to $\bar{S}_{21}$ in equation B.1.

The gain and phase are effectively Taylor expansions, and more or less terms could be included for higher accuracy. In practice, a second degree polynomial works well for the gain. The phase is only expanded to first order since there are few physical processes that can cause a quadratic variation of the phase with frequency. The first order coefficient is often explained by introducing the cable delay, $\tau = {}^{-\phi_1}/_{2\pi f_m}$, which takes into account the changing electrical length of the cabling with frequency. Typically, τ ranges from 10 to 100 ns depending on the setup.

Including this rescaling, we can write the forward scattering matrix element as

$$S_{21} = \left(g_0 + g_1 x_m + g_2 x_m^2\right) e^{i(\phi_0 + \phi_1 x_m)} \frac{Q_c + 2iQ_iQ_c(x_g + x_a)}{Q_i + Q_c + 2iQ_iQ_c x_g}. \tag{B.6}$$

B.2 Nonlinear Resonance

The equations for the forward scattering matrix element presented in appendix B.1 assume the impedance diagram shown in figure B.1. Each impedance must behave linearly with generator voltage, V_g. However, all superconductors display some nonlinear behavior in their surface impedance at high enough drive powers [80, 100, 182, 183]. For disordered superconductors with high normal-state resistivity the primary effect is an intrinsic current nonlinearity in their kinetic inductance.

$$L_k(I) = L_k(0)\left(1 + \left(\frac{I}{I^*}\right)^2 + ...\right) \tag{B.7}$$

Equation B.7 implies that the resonator's resonance frequency will depend on its internal current. Since a frequency closer to f_r results in a larger current flowing through the resonator, this nonlinearity can be incorporated into S_{21} by noting that equation B.7 dynamically modifies the resonance frequency depending on the generator frequency. For the symmetric case, $Z_1 = Z_2 = 0$, Swenson et al. [100] show that this effect is equivalent to setting $x_g \rightarrow x_n$ in equation B.6, where x_n is defined by the implicit equation

$$Qx_n = Qx_g + \frac{a}{1 + 4Q^2x_n^2}. \tag{B.8}$$

a parameterizes the nonlinearity and is proportional to the generator power. In this model, the onset of the resonance bifurcation occurs at $a = a_{\text{sat}} \equiv {}^{4\sqrt{3}}/_{9} \sim 0.77$. Equation B.8 can be solved by reducing it to a cubic polynomial equation, so, although complicated, an exact algebraic expression exists for x_n in terms of x_g.

A similar result holds for the asymmetric case. For the proof, we must first find an expression for the power dissipated in the resonator, P_d, as a function of the current flowing through it, I_3.

$$P_d(f) = \frac{1}{2}\text{Re}[Z_3(f)]\left|\int_{-\infty}^{\infty} \tilde{I}_3(f)df\right|^2 \tag{B.9}$$

Working with the currents, voltages, and impedances in figure B.1, we use Kirchoff's current and voltage laws to find an expression for the current flowing through the resonator.

$$\tilde{I}_3 = (Z_0 + Z_1)^{-1}\left(\tilde{V}_g - \frac{2Z_0 + Z_1 + Z_2}{2Z_0}2\tilde{V}_2\right) \tag{B.10}$$

The generator voltage is at a single frequency, and since we are ignoring harmonics introduced by the nonlinearity, we can write

$$V_g(t) = \mathrm{Re}\left[\hat{V}_g e^{2\pi i f_g t}\right] \tag{B.11a}$$

$$V_2(t) = \mathrm{Re}\left[\hat{V}_2 e^{2\pi i f_g t}\right] \tag{B.11b}$$

Using this notation, the Fourier transforms of V_g and V_2 are given by the following equations:

$$\tilde{V}_g = \frac{1}{2}\left[\hat{V}_g \delta(f_g - f) + \hat{V}_g^* \delta(f_g + f)\right] \tag{B.12a}$$

$$\tilde{V}_2 = \frac{1}{2}\left[\hat{V}_2 \delta(f_g - f) + \hat{V}_2^* \delta(f_g + f)\right]. \tag{B.12b}$$

In these conditions we can simplify by introducing the complex incident, V_n^+, and reflected, V_n^-, voltage waves at the nth port:

$$\begin{aligned} V_n^+(t) &\equiv \mathcal{F}_f^{-1}\left[\left(\tilde{V}_n(f) + Z_0\tilde{I}_n(f)\right)\theta(f)\right](t) \\ V_n^-(t) &\equiv \mathcal{F}_f^{-1}\left[\left(\tilde{V}_n(f) - Z_0\tilde{I}_n(f)\right)\theta(f)\right](t), \end{aligned} \tag{B.13}$$

where $\theta(\cdot)$ is the Heaviside step function.

Using $\tilde{V}_2 = -Z_0\tilde{I}_2$ and $\tilde{V}_1 = \tilde{V}_g - Z_0\tilde{I}_1$, the forward scattering matrix and the power sent into the device from the generator can then be written as

$$\begin{aligned} S_{21} \equiv & \left.\frac{V_2^-}{V_1^+}\right|_{V_2^+=0} \\ = & \frac{2\hat{V}_2}{\hat{V}_g}, \end{aligned} \tag{B.14}$$

and

$$\begin{aligned} P_g \equiv & \frac{\left|V_1^+\right|^2}{2Z_0} \\ = & \frac{\left|\hat{V}_g\right|^2}{8Z_0}. \end{aligned} \tag{B.15}$$

Putting together the results from appendix B.1 and equations B.9, B.14 and B.15,

$$\begin{aligned} P_d = & \frac{Z_0 R_0}{|Z_0 + Z_1|^2} \frac{2Q_c}{Q_i} \left|1 - \bar{S}_{21}\right|^2 P_g \\ = & \frac{Z_0 R_0}{|Z_0 + Z_1|^2} \frac{2Q^2}{Q_i Q_c} \frac{1 + 4Q_c^2 x_a^2}{1 + 4Q^2 x_g^2} P_g. \end{aligned} \tag{B.16}$$

With equation B.16, we follow the steps laid out by Swenson et al. [100] to find

$$Qx_n = Qx_g + \frac{Z_0 R_0}{|Z_0 + Z_1|^2} \frac{1 + 4Q_c^2 x_a^2}{1 + 4Q^2 x_n^2} a, \tag{B.17}$$

which is functionally the same as equation B.8. The saturation condition for the resonance is then $\bar{a} = a_{\text{sat}}$ with

$$\bar{a} = \frac{Z_0 R_0}{|Z_0 + Z_1|^2} (1 + 4Q_c^2 x_a^2) a. \tag{B.18}$$

An important consequence of equations B.16 and B.17 is that in the asymmetric case the power dissipated in the resonator depends on the order of Z_1 and Z_2 in the circuit: the impedances cannot be interchanged without changing the result. This leads to $S_{21} \neq S_{12}$

for a constant P_g when the current nonlinearity in Z_3 is introduced. However, the nonlinearity in an asymmetric resonator can be completely described by the symmetric equations under the following conditions: $\mathrm{Im}[Z_1] = \mathrm{Im}[Z_2]$ and $\mathrm{Re}[Z_1] = \mathrm{Re}[Z_2] = \mathrm{Im}[Z_0] = 0$. This case could correspond, for example, to Z_1 and Z_2 describing two identical, lossless wire bond inductances on a lossless transmission line. With these assumptions, $\bar{a}$ is exactly equal to a and doesn't depend on x_a or Q_c.

B.3 $\mathcal{I}$ / $\mathcal{Q}$ Mixer Measurement and Calibration

Once the generator signal passes through the circuit shown in figure B.1, it travels along a transmission line with impedance Z_0, through various amplifiers and attenuators, and finally to an $\mathcal{I}$ / $\mathcal{Q}$ mixer. The mixer is used to down-convert the signal into the frequency band around the generator frequency, f_g. Ideally, the $\mathcal{I}$ and $\mathcal{Q}$ signals follow the relations

$$\mathcal{I}(t) = \int_{-\infty}^{t} G_m(t-t')V_m(t')\cos\bigl(2\pi f_g t'\bigr)dt' \tag{B.19a}$$

$$\mathcal{Q}(t) = -\int_{-\infty}^{t} G_m(t-t')V_m(t')\sin\bigl(2\pi f_g t'\bigr)dt', \tag{B.19b}$$

where G_m is a transfer function that takes into account any conversion loss or phase shifts that occur in the mixer and V_m is the voltage at the mixer's RF port.

In the frequency domain, for $|f| \ll f_g$, these equations become

$$\tilde{\mathcal{I}}(f) = \frac{1}{2}\tilde{G}_m(f)\left[\tilde{V}_m(f_g+f)+\tilde{V}_m^*(f_g-f)\right] \tag{B.20a}$$

$$\tilde{\mathcal{Q}}(f) = -\frac{i}{2}\tilde{G}_m(f)\left[\tilde{V}_m(f_g+f)-\tilde{V}_m^*(f_g-f)\right]. \tag{B.20b}$$

We can also write the mixer input voltage in terms of the output voltage from the circuit in figure B.1 by defining a transfer function, G_a, that takes into account all of the amplifiers and other circuit components between the circuit and the mixer.

$$\tilde{V}_m(f) = \tilde{G}_a(f)\tilde{V}_2(f) \tag{B.21}$$

In the steady state case, where $f = 0$, the $\mathcal{I}$ and $\mathcal{Q}$ DC signal is proportional to the real and imaginary part of the forward scattering matrix element, S_{21}.

$$\tilde{\mathcal{I}}(0) = \frac{1}{2}\mathrm{Re}\left[\tilde{G}_m(0)\tilde{G}_a(f_g)S_{21}(f_g)\tilde{V}_g(f_g)\right] \tag{B.22a}$$

$$\tilde{\mathcal{Q}}(0) = \frac{1}{2}\mathrm{Im}\left[\tilde{G}_m(0)\tilde{G}_a(f_g)S_{21}(f_g)\tilde{V}_g(f_g)\right] \tag{B.22b}$$

Therefore, we can treat $\mathcal{Z} \equiv \mathcal{I} + i\mathcal{Q} = S_{21}(f_g)$ when in the steady state conditions if we absorb the extra gain and phase factors into the gain and phase polynomials in equation B.6.

In reality, an $\mathcal{I}$ / $\mathcal{Q}$ mixer is made from two standard mixers. For equation B.19 to be valid, the two mixers must be identical, which is never exactly the case. We can model the imperfections by introducing an imbalance in the amplitude, α, and phase, β. There will also always be some DC signal from the $\mathcal{I}$ / $\mathcal{Q}$ mixer even when $V_m = 0$, so we introduce the offsets γ and δ. Each of these parameters is frequency dependent but typically does not vary strongly over several MHz, which allows us to treat them as constants. These considerations transform equations B.19a and B.19b to

$$\mathcal{I}'(t) = \int_{-\infty}^{t} G_m(t-t')V_m(t')\cos\left(2\pi f_g t'\right)dt' + \gamma \tag{B.23a}$$

$$\mathcal{Q}'(t) = -\alpha \int_{-\infty}^{t} G_m(t-t')V_m(t')\sin\left(2\pi f_g t' - \beta\right)dt' + \delta. \tag{B.23b}$$

Equations B.19 and B.23 can be written in terms of each other with a matrix relation, allowing us to transform between the measured mixer output, ($\mathcal{I}'$, $\mathcal{Q}'$), and the ideal mixer output, ($\mathcal{I}$, $\mathcal{Q}$), which is related to the forward scattering matrix element, S_{21}.

$$\begin{pmatrix} \mathcal{I}(t) \\ \mathcal{Q}(t) \end{pmatrix} = \begin{pmatrix} 1 & 0 \\ -\tan(\beta) & \alpha^{-1}\sec(\beta) \end{pmatrix} \begin{pmatrix} \mathcal{I}'(t) - \gamma \\ \mathcal{Q}'(t) - \delta \end{pmatrix} \tag{B.24a}$$

$$\begin{pmatrix} \mathcal{I}'(t) \\ \mathcal{Q}'(t) \end{pmatrix} = \begin{pmatrix} 1 & 0 \\ \alpha\sin(\beta) & \alpha\cos(\beta) \end{pmatrix} \begin{pmatrix} \mathcal{I}(t) \\ \mathcal{Q}(t) \end{pmatrix} + \begin{pmatrix} \gamma \\ \delta \end{pmatrix} \tag{B.24b}$$

To make use of this transformation, the parameters α, β, γ, and δ must be measured before taking data. There are many techniques for making this measurement. The simplest, if two frequency synthesizers are available, is to put a signal with frequency f_g into the mixer's LO port and a signal with frequency $f_g + \Delta f$ into the RF port. Δf must be inside the measurement bandwidth for the system and much smaller than the expected scale at which α, β, γ, and δ are expected to vary. Then, up to an arbitrary phase and ignoring terms with frequencies much larger than f_g, equations B.23a and B.23b give

$$\mathcal{I}'(t) = A\cos(2\pi\Delta f t) + \gamma \tag{B.25a}$$

$$\mathcal{Q}'(t) = \alpha A\sin(2\pi\Delta f t + \beta) + \delta, \tag{B.25b}$$

where A is the output signal amplitude.

By averaging these signals over many periods, $\langle\cdot\rangle_T$, we can extract the imbalance and offset parameters with the following equations:

$$\gamma = \langle \mathcal{I}'(t)\rangle_T \tag{B.26a}$$

$$\delta = \langle \mathcal{Q}'(t)\rangle_T \tag{B.26b}$$

$$A = \sqrt{2\left\langle(\mathcal{I}'(t)-\gamma)^2\right\rangle_T} \tag{B.26c}$$

$$\alpha = \frac{1}{A}\sqrt{2\left\langle(\mathcal{Q}'(t)-\delta)^2\right\rangle_T} \tag{B.26d}$$

$$\sin(\beta) = \frac{2}{\alpha A^2}\langle(\mathcal{I}'(t)-\gamma)(\mathcal{Q}'(t)-\delta)\rangle_T. \tag{B.26e}$$

B.4 Varying Circuit Parameters

Up until now, the circuit components in figure B.1 have been assumed to be constant over time. However, if they vary at frequencies much smaller than f_g, we can still use the impedance formalism. In this section, we will derive how those changes effect the $\mathcal{I}$ / $\mathcal{Q}$ mixer output.

The results presented here are not new and have been discussed by several other authors [42, 73, 93]. However, while all authors agree on the conclusion, the derivation is either glossed over or presented for a particular circuit configuration. The rotation of S_{21} introduced by impedance mismatches is also not included. Here, care was taken to use the most general circuit definition possible and include the loop asymmetry in the analysis. This way, we can be certain of the derivation's full generality.

In the steady state case, where the circuit components aren't changing, the impedance formalism implies that there exists a linear operator, $\hat{F}$, which relates the current going through the resonator and the generator voltage.

$$\hat{F} I_3(t) = V_g(t) \tag{B.27}$$

Assuming the generator voltage is at a single frequency, as in equations B.11a and B.12a, we already know the solution to equation B.27 from appendix B.2. In the Fourier domain,

$$\tilde{I}_3(f) = [Z_0 + Z_1]^{-1} \left[1 - \bar{S}_{21}(f)\right] \tilde{V}_g(f). \tag{B.28}$$

We can use this knowledge to determine the complex wave response of the operator.

$$\int_{-\infty}^{\infty} df \tilde{I}_3(f) \hat{F} e^{2\pi i f t} = \int_{-\infty}^{\infty} df \tilde{V}_g(f) e^{2\pi i f t}, \tag{B.29}$$

which gives

$$\hat{F} e^{2\pi i f t} = [Z_0 + Z_1] \left[1 - \bar{S}_{21}(f)\right]^{-1} e^{2\pi i f t}. \tag{B.30}$$

We will need this relationship later since it allows us to evaluate $\hat{F}$ acting on any function by substituting that function's Fourier transform.

To incorporate changes in the impedance, Z_3, we note that there is a one-to-one correspondence between Z_3 and $\bar{S}_{21}$. Therefore, the changes to the $\mathcal{I}$ and $\mathcal{Q}$ signals can be parameterized in terms of changes to the forward scattering parameter, where

$$\bar{S}_{21} \longrightarrow \bar{S}_{21} + \overline{\delta S}_{21}(t) \tag{B.31a}$$

$$I_3(t) \longrightarrow I_3(t) + \delta I_3(t) \tag{B.31b}$$

$$\hat{F} \longrightarrow \hat{F} + \overline{\delta S}_{21}(t) \left. \frac{\partial \hat{F}}{\partial \bar{S}_{21}} \right|_{\bar{S}_{21}} \tag{B.31c}$$

Introducing these substitutions, equation B.27 becomes

$$\left[\hat{F} + \overline{\delta S}_{21}(t) \left. \frac{\partial \hat{F}}{\partial \bar{S}_{21}} \right|_{\bar{S}_{21}} \right] [I_3(t) + \delta I_3(t)] = V_g(t). \tag{B.32}$$

The largest possible change in the scattering parameter is given by $\left|\overline{\delta S}_{21}\right| = \sqrt{1 + 4Q^2 x_a^2}$, which is achieved only if $Q_c \delta Q_i^{-1} \gg 1$ or $2Q^{\delta f_r}/f_r \gg 1$ for a low loss resonator. Most changes aren't that large, so we can restrict our analysis to $\left|\overline{\delta S}_{21}\right| < 1$ without much difficulty. Similarly, on resonance I_3 has it's largest amplitude, if $\overline{\delta S}_{21}$ is at it's maximum then $\delta I_3 = -I_3$ since no current flows through the resonator. Therefore, $\delta I_3 < I_3$. We are justified in dropping the second order term, and using the fact that I_3 already satisfies equation B.27, we have

$$\hat{F} \delta I_3(t) = -\overline{\delta S}_{21}(t) \left. \frac{\partial \hat{F}}{\partial \bar{S}_{21}} \right|_{\bar{S}_{21}} I_3(t). \tag{B.33}$$

Since I_3 is a solution to equation B.27, we can use the product rule to evaluate the first derivative of $\hat{F}$.

$$\left.\frac{\partial \hat{F}}{\partial \bar{S}_{21}}\right|_{\bar{S}_{21}} I_3(t) + \hat{F}\left.\frac{\partial I_3(t)}{\partial \bar{S}_{21}}\right|_{\bar{S}_{21}} = 0 \tag{B.34}$$

Simplifying equation B.33 using our expression for the Fourier transform of I_3 in equation B.28, we have

$$\begin{aligned}
\hat{F}\delta I_3(t) &= \overline{\delta S}_{21}(t)\ \hat{F}\left.\frac{\partial I_3(t)}{\partial \bar{S}_{21}}\right|_{\bar{S}_{21}} \\
&= \overline{\delta S}_{21}(t)\ \hat{F}\mathcal{F}_f^{-1}\left[\left.\frac{\partial \tilde{I}_3(f)}{\partial \bar{S}_{21}}\right|_{\bar{S}_{21}}\right](t) \\
&= -[Z_0 + Z_1]^{-1}\overline{\delta S}_{21}(t)\ \hat{F}V_g(t).
\end{aligned} \tag{B.35}$$

Equation B.30 allows us to act $\hat{F}$ on both sides.

$$\begin{gathered}
\int_{-\infty}^{\infty} df\widetilde{\delta I}_3(f)\hat{F}e^{2\pi i f t} = -[Z_0 + Z_1]^{-1}\overline{\delta S}_{21}(t)\int_{-\infty}^{\infty} df\tilde{V}_g(f)\hat{F}e^{2\pi i f t} \\
\mathcal{F}_f^{-1}\Big[[Z_0 + Z_1]\big[1 - \bar{S}_{21}(f)\big]^{-1}\widetilde{\delta I}_3(f)\Big](t) = -\overline{\delta S}_{21}(t)\mathcal{F}_f^{-1}\Big[\big[1 - \bar{S}_{21}(f)\big]^{-1}\tilde{V}_g(f)\Big](t)
\end{gathered} \tag{B.36}$$

Finally, taking the Fourier transform and using convolution theorem gives us an expression for the current perturbation in the frequency domain.

$$\widetilde{\delta I}_3(f) = [Z_0 + Z_1]^{-1}\big[1 - \bar{S}_{21}(f)\big]\int_{-\infty}^{\infty} df e^{2\pi i f t}\int_{-\infty}^{\infty} df'\big[1 - \bar{S}_{21}(f')\big]^{-1}\tilde{V}_g(f')\widetilde{\overline{\delta S}}_{21}(f - f') \tag{B.37}$$

We can simplify by inserting equation B.12a and integrating.

$$\widetilde{\delta I}_3(f) = -\frac{1}{2}[Z_0 + Z_1]^{-1}\big[1 - \bar{S}_{21}(f)\big]\left[\frac{\hat{V}_g\widetilde{\overline{\delta S}}_{21}(f - f_g)}{1 - \bar{S}_{21}(f_g)} + \frac{\hat{V}_g^{*}\widetilde{\overline{\delta S}}_{21}(f + f_g)}{1 - \bar{S}_{21}^{*}(f_g)}\right] \tag{B.38}$$

Writing our result in terms of the output voltage,

$$\begin{aligned}\widetilde{\delta V}_2(f) &= \frac{1}{2}\frac{Z_0}{2Z_0 + Z_1 + Z_2}\left[1 - \bar{S}_{21}(f)\right]\left[\frac{\hat{V}_g \widetilde{\widetilde{\delta S}}_{21}(f - f_g)}{1 - \bar{S}_{21}(f_g)} + \frac{\hat{V}_g^* \widetilde{\widetilde{\delta S}}_{21}(f + f_g)}{1 - \bar{S}_{21}^*(f_g)}\right] \\ &= \frac{1}{4}\left[1 - \bar{S}_{21}(f)\right]\left[\frac{\hat{V}_g \widetilde{\delta S}_{21}(f - f_g)}{1 - \bar{S}_{21}(f_g)} + \frac{\hat{V}_g^* \widetilde{\delta S}_{21}(f + f_g)}{1 - \bar{S}_{21}^*(f_g)}\right].\end{aligned} \tag{B.39}$$

In the last line we combined the extra impedance factors with $\widetilde{\widetilde{\delta S}}_{21}$ to give $\widetilde{\delta S}_{21}$.

We can then write the voltage perturbation in terms of $\delta\mathcal{Z}(t) \equiv \delta\mathcal{I}(t) + i\delta\mathcal{Q}(t)$, absorbing the total signal amplitude and phase into S_{21}. In equations B.20a, B.20b and B.21, this corresponds to setting $G_m \rightarrow 2$ and $\tilde{G}_a \rightarrow {}^1/_{\hat{V}_g}$.

$$\widetilde{\delta\mathcal{I}}(f) = \frac{1}{2}\left[\frac{1 - \bar{S}_{21}(f_g + f)}{1 - \bar{S}_{21}(f_g)}\,\widetilde{\delta S}_{21}(f) + \frac{1 - \bar{S}_{21}^*(f_g - f)}{1 - \bar{S}_{21}^*(f_g)}\,\widetilde{\delta S}_{21}^*(f)\right] \tag{B.40a}$$

$$\widetilde{\delta\mathcal{Q}}(f) = -\frac{i}{2}\left[\frac{1 - \bar{S}_{21}(f_g + f)}{1 - \bar{S}_{21}(f_g)}\,\widetilde{\delta S}_{21}(f) - \frac{1 - \bar{S}_{21}^*(f_g - f)}{1 - \bar{S}_{21}^*(f_g)}\,\widetilde{\delta S}_{21}^*(f)\right] \tag{B.40b}$$

$$\widetilde{\delta\mathcal{Z}}(f) = \frac{1 - \bar{S}_{21}(f_g + f)}{1 - \bar{S}_{21}(f_g)}\,\widetilde{\delta S}_{21}(f) \tag{B.40c}$$

Terms where $\widetilde{\delta S}_{21}$ is evaluated at frequencies above f_g are ignored since we require that the circuit parameters vary at slower time scales than the voltage.

For $f_g = f_r$,

$$\widetilde{\delta\mathcal{Z}}(f) = \frac{1}{1 - {}^{2iQf}/_{f_r}}\,\widetilde{\delta S}_{21}(f). \tag{B.41}$$

Therefore, when the generator is tuned to the resonance frequency, changes in the $\mathcal{I}$ and $\mathcal{Q}$ signals originating from changes in the resonator's impedance are lowpass filtered at the resonator bandwidth, $\Delta f = {}^{f_r}/_{2Q}$.

C

Y-Factor Measurement

Measuring the absolute magnitude of the noise in a microwave system can be difficult since it requires a very detailed knowledge of the gains and attenuations in the system. Unfortunately, these values always change slightly when you measure them individually. To resolve this issue, a Y-factor measurement is a common solution where the gains and attenuations in the system are calibrated by measuring two sources with a known noise magnitude [96, §10.1]. Here, we expand on this method to analyze the magnitudes of noise sources coming from the different components in our TWPA system.

C.1 Noise in Different Coordinates

In order to do an accurate noise measurement, the relationship between noise in different coordinate systems must be understood. There are many places for factor-of-two errors, so this section explicitly relates the PSDs between voltage data, $\mathcal{I}$ or $\mathcal{Q}$ data, and phase or dissipation data.

To start, we define the signal going into the mixer as

$$V(t) \equiv A\cos\big(2\pi f_g t + \phi\big) + n_V(t), \tag{C.1}$$

where $n_V(t)$ is a realization of the voltage noise. Using equation B.20, we can relate $n_V(t)$ to the noise in the $\mathcal{I}$ coordinate in the frequency domain.

$$\tilde{n}_{\mathcal{I}}(f) = \frac{1}{2}\big(\tilde{n}_V(f_g + f) + \tilde{n}_V^*(f_g - f)\big) \tag{C.2}$$

where we have referenced the signal and noise in the $\mathcal{I}$ coordinate to the input of the mixer to avoid using $\tilde{G}_m(f)$. This gain factor cancels out in the radial noise case and we lump it in with the total system gain otherwise, so it is not important to include it.

The voltage PSD is defined by

$$\big\langle \tilde{n}_V(f)\tilde{n}_V^*(f')\big\rangle \equiv S_V(f)\delta(f - f'). \tag{C.3}$$

Using equation C.2 to relate the voltage and $\mathcal{I}$ coordinate, we have

$$\big\langle \tilde{n}_{\mathcal{I}}(f)\tilde{n}_{\mathcal{I}}^*(f')\big\rangle = \frac{1}{2}S_V(f)\bigg(\delta(f - f') + \frac{1}{2}\delta(f - f' - 2f_g) + \frac{1}{2}\delta(f + f' + 2f_g)\bigg). \tag{C.4}$$

Since we are only interested in frequencies closer together than $2f_g$, we can drop the last two terms. We can then relate the voltage PSD to that in the $\mathcal{I}$ coordinate.

$$S_{\mathcal{I}}(f) = \frac{1}{2}S_V(f) \tag{C.5}$$

The relationship and derivation for the $\mathcal{Q}$ coordinate is the same.

To relate the voltage noise to the phase or dissipation coordinates, we first write the signal in the $\mathcal{I}$ coordinate as a function of our parameterization for $V(t)$.

$$\begin{aligned}\langle \mathcal{I}(t)\rangle &\equiv \left\langle V(t)\cos\left(2\pi f_g t\right)\right\rangle \\ &= \left\langle \frac{A}{2}\left(\cos(\phi) + \cos\left(4\pi f_g t + \phi\right)\right)\right\rangle \\ &= \frac{A}{2}\cos(\phi)\end{aligned} \tag{C.6}$$

Similarly, $\langle \mathcal{Q}(t)\rangle = {}^{A\sin(\phi)}/_{2}$. Ignoring the resonance, $\mathcal{I}$ and $\mathcal{Q}$ trace out a circle of radius ${}^{A}/_{2}$ centered at the origin as the generator frequency is swept and ϕ changes with the cable delay. The resonance loop radius, r, is then given by

$$r = \frac{A}{2}\sqrt{\left(\frac{Q}{2Q_c}\right)^2 + Q^2 x_a^2}, \tag{C.7}$$

where we've included a factor corresponding to the loop radius in the normalized $\bar{\mathcal{I}}$ and $\bar{\mathcal{Q}}$ coordinates.

We can further relate A to the microwave power entering the mixer, P.

$$\begin{aligned}P &\equiv \frac{\left\langle V(t)^2\right\rangle}{Z_0} \\ &= \frac{A^2}{2Z_0},\end{aligned} \tag{C.8}$$

which gives

$$r = \sqrt{\frac{Z_0 P}{2}\left(\left(\frac{Q}{2Q_c}\right)^2 + Q^2 x_a^2\right)}. \tag{C.9}$$

The noise in radial coordinates is then

$$
\begin{aligned}
S_{\text{rad}}(f) &= \frac{S_{\mathcal{I}}(f)}{r^2} \\
&= \frac{S_V(f)}{2r^2} \\
&= \frac{S_V(f)}{Z_0 P\left(\left(\frac{Q}{2Q_c}\right)^2 + Q^2 x_a^2\right)}.
\end{aligned}
\tag{C.10}
$$

We should briefly note here that equation C.10 is only valid for noise sources that are agnostic to the orientation of the $\mathcal{I}$ and $\mathcal{Q}$ coordinates. TLS noise is a classic example of when this is not the case where the noise only shows up in the phase quadrature. To account for this effect, one needs to think about how much of the phase noise translates into $\mathcal{I}$ or $\mathcal{Q}$ by looking at the rotation matrix which connects the two coordinate systems.

C.2 Noise Measurement

The noise figures presented in table 5.1 are determined by the following measurement, which consists of taking four noise data sets using a microwave switch to change the input to the HEMT. From each noise data set, the single-sided PSD is computed for each quadrature and averaged. Superconducting coaxes are used between the HEMT and the switch and between the switch and the terminations to ensure an accurate calibration.

- $S_0(f)$: The input of the HEMT is terminated at $T_{\text{hot}} \sim 3.3\,\text{K}$.
- $S_1(f)$: The input of the HEMT is terminated at $T_{\text{cold}} \sim 100\,\text{mK}$.
- $S_2(f)$: The HEMT is connected to the TWPA and MKID with the pump tone and DC

current off.

- $S_3(f)$: The HEMT is connected to the TWPA and MKID with the pump tone and DC current on.

The average of the single-sided PSDs for each quadrature, $\mathcal{I}$ and $\mathcal{Q}$ around a frequency f, on a terminated transmission line with impedance Z_0, and at an equilibrium temperature T is given by

$$S(f) = \frac{h f_g Z_0}{2}\left(\frac{1}{e^{h f_g / k_B T} - 1} + \frac{1}{2}\right), \tag{C.11}$$

where the first component comes from the thermal Johnson noise and the second from the zero-point fluctuations [144]. Note the factor of two difference between this noise for $\mathcal{I}$ or $\mathcal{Q}$ and equation 5.9 for the total voltage noise which was derived in appendix C.1. Equation C.11 holds for $f \ll f_g$ and shows that the noise is independent of spectral frequency.

The noise added by the two different temperature terminations is calculated using equation C.11 and is labeled $S_{\text{hot}}(f)$ and $S_{\text{cold}}(f)$ for T_{hot} and T_{cold} respectively. The four measurements can then be written in terms of their components, where $S_{\text{I}}(f)$ is the noise at the input of the TWPA, $S_{\text{P}}(f)$ is the noise added by the TWPA, and $S_{\text{H}}(f)$ is the noise added by the HEMT amplifier.

$$\begin{aligned}
S_0(f) &= G_{\text{H}}(f)(S_{\text{hot}}(f) + S_{\text{H}}(f)) \\
S_1(f) &= G_{\text{H}}(f)(S_{\text{cold}}(f) + S_{\text{H}}(f)) \\
S_2(f) &= G_{\text{H}}(f)(S_{\text{I}}(f) + S_{\text{H}}(f)) \\
S_3(f) &= G_{\text{H}}(f)(G_{\text{P}}(S_{\text{I}}(f) + S_{\text{P}}(f)) + S_{\text{H}}(f))
\end{aligned} \tag{C.12}$$

$G_\mathrm{H}(f)$ is the total gain of the system excluding the TWPA and must be calculated. Frequency rolloffs from the anti-aliasing filter will be included in this function, for example. G_P is the gain of the TWPA and can be accurately determined by measuring the amplitude of a probe tone tuned off resonance with the TWPA turned on and off. This system of equations can be solved for the unknown parameters.

$$\begin{aligned}
G_\mathrm{H}(f) &= \frac{S_0(f) - S_1(f)}{S_\mathrm{hot}(f) - S_\mathrm{cold}(f)} \\
S_\mathrm{H}(f) &= \frac{S_1(f)S_\mathrm{hot}(f) - S_0(f)S_\mathrm{cold}(f)}{S_0(f) - S_1(f)} \\
S_\mathrm{I}(f) &= \frac{(S_2(f) - S_1(f))S_\mathrm{hot}(f) + (S_0(f) - S_2(f))S_\mathrm{cold}(f)}{S_0(f) - S_1(f)} \\
S_\mathrm{P}(f) &= \frac{\begin{array}{r}[S_3(f) - S_1(f) - G_\mathrm{P}(S_2(f) - S_1(f))]S_\mathrm{hot}(f) + \\ [S_0(f) - S_3(f) - G_\mathrm{P}(S_0(f) - S_2(f))]S_\mathrm{cold}(f)\end{array}}{G_\mathrm{P}(S_0(f) - S_1(f))}
\end{aligned} \tag{C.13}$$

The added noise in units of photon quanta for the components of the system are given in equation C.14, where we have defined $A_\mathrm{sys}(f)$ to be the total noise of the system off resonance.

$$\begin{aligned}
A_\mathrm{I}(f) &= \frac{2S_\mathrm{I}(f)}{hfZ_0} \\
A_\mathrm{P}(f) &= \frac{2S_\mathrm{P}(f)}{hfZ_0} \\
A_\mathrm{H}(f) &= \frac{2S_\mathrm{H}(f)}{hfZ_0} \\
A_\mathrm{sys}(f) &\equiv A_\mathrm{I}(f) + A_\mathrm{P}(f) + \frac{A_\mathrm{H}(f)}{G_\mathrm{P}}
\end{aligned} \tag{C.14}$$

C.3 Statistical and Systematic Errors

As written in appendix C.2, $S_\mathrm{H}(f)$, $A_\mathrm{H}(f)$, $S_\mathrm{P}(f)$, $A_\mathrm{P}(f)$, $S_\mathrm{I}(f)$, $A_\mathrm{I}(f)$, $A_\mathrm{sys}(f)$ are all functions of f. However, they should be frequency independent. We can look for this characteristic to check for any unexpected properties of the data. It also allows us to easily determine the statistical uncertainties from the marginal likelihood distribution for the mean.

$$\mathcal{L}\left(\bar{X}|X(f)\right) = \text{StudentT}\left(\frac{\bar{X} - \mathrm{E}\left[X(f)\right]}{\sqrt{\frac{\mathrm{Var}\left[X(f)\right]}{N_f}}}, N_f - 1\right), \tag{C.15}$$

where $X(f)$ is one of the above parameters, $\mathrm{E}\left[\cdot\right]$ is the mean of the values over frequency, $\mathrm{Var}\left[\cdot\right]$ is the variance of the values over frequency, and N_f is the number of frequency bins. For the amplifier and thermal added noise numbers, an additional prior can be included for only allowing physical values, $\bar{X} \geq {}^1\!/_2$.

We also account for any systematic errors which affect the noise measurement. Error terms are estimated and a Monte Carlo simulation is done to compute a posterior distribution for the noise numbers.

Losses at the 100 mK stage are small but they may exist. We introduce two loss parameters. l_P represents losses between the parametric amplifier and switch, and l_H represents losses between the switch and HEMT. We expect these losses to be not much greater than 1 dB, so we draw random samples from the following exponential distribution:

$$f(x) = \begin{cases} \frac{1}{\beta-1} e^{-\frac{x-1}{\beta-1}} & x \geq 1 \\ 0 & x < 1 \end{cases} \tag{C.16}$$

with $\beta = 1\,\mathrm{dB} \approx 1.26$.

We also consider thermometer calibration errors which we do not expect to be more than 10 %. The temperatures for $S_\mathrm{cold}(f)$ and $S_\mathrm{hot}(f)$ are drawn from the normal distribution, $\mathcal{N}(T, {}^{T}\!/_{10})$, for their respective temperatures, where the second value is the standard deviation.

The resulting equations representing our measurement are modified from equation C.12 to

$$\begin{aligned}
S_0(f) =& G_\mathrm{H}(f)\left(\frac{S'_\mathrm{hot}(f) - S_\mathrm{Z}(f)}{l_\mathrm{H}} + S_\mathrm{Z}(f) + S_\mathrm{H}(f)\right)\\
S_1(f) =& G_\mathrm{H}(f)\left(\frac{S'_\mathrm{cold}(f) - S_\mathrm{Z}(f)}{l_\mathrm{H}} + S_\mathrm{Z}(f) + S_\mathrm{H}(f)\right)\\
S_2(f) =& G_\mathrm{H}(f)\left(\frac{S_\mathrm{I}(f) - S_\mathrm{Z}(f)}{l_\mathrm{H} l_\mathrm{P}} + S_\mathrm{Z}(f) + S_\mathrm{H}(f)\right)\\
S_3(f) =& G_\mathrm{H}(f)\left(\frac{G_\mathrm{P}}{l_\mathrm{H} l_\mathrm{P}}(S_\mathrm{I}(f) + S_\mathrm{P}(f) - 2S_\mathrm{Z}(f)) + 2G_\mathrm{P}S_\mathrm{Z}(f) + S_\mathrm{H}(f)\right).
\end{aligned} \tag{C.17}$$

$S'_\mathrm{hot}(f)$ and $S'_\mathrm{cold}(f)$ are from the calibration terminations if their temperatures were different than our expectation. $S_\mathrm{Z}(f) \equiv {}^{hfZ_0}\!/_2$ is the zero-point noise contribution. The solution to equation C.17 for many different samples of the loss and temperature distributions give the second set of confidence intervals presented in table 5.1. In the original published version of equation C.17, the attenuation factors, l_H and l_P were misplaced and $S_\mathrm{Z}(f)$ was not properly accounted for since it does not get attenuated [105, 184]. This oversight resulted in an overestimate of the systematic error confidence interval size for the TWPA and input noise numbers.

D

Phonon Loss Calculations

To use equation 6.2 to estimate the phonon loss contribution to the resolving power, we need to estimate the phonon loss factor, J. The phonon loss can be partitioned into two contributions, $J = J_{\text{high}} + J_{\text{low}}$. J_{high} represents the initial wave of phonons created as the hot electron plasma cools to the Debye temperature of the superconductor. There are relatively few of these phonons and they each carry a significant fraction of the original photon's energy. J_{low} represents the quasi-equilibrium phonons propagating through the superconductor as they down convert in energy and eventually drop below the 2Δ threshold for breaking new Cooper pairs. Each contribution requires knowledge of different material constants, most of which are fairly uncertain for hafnium and platinum silicide. As such, the calculations presented below should be considered order of magnitude estimates instead of rigorous theoretical results.

D.1 Determining J_{high}

The formula for J_{high} is given in reference 168 in equation 25. If the film is thin with respect to the optical depth in the film, a simpler form may be found in reference 185 in equation 10. We will use the full form here since our films can be quite thick.

$$J_{\text{high}} = 4\eta_{\text{pb}} \frac{\Omega_{\text{D}}}{\Delta} \sum_{m=0}^{\infty} \left\{ \frac{e^{-m^2\zeta^2} \sinh\left(m^2\zeta^2\right)(-1)^{2m}\left(1 - e^{im\pi - d/L}\right)}{m^2\zeta^2(1+\delta_{m,0})\left(1 - e^{-d/L}\right)\left(1 + m^2\pi^2L^2/d^2\right)} \int_0^{\Omega_{\text{D}}} \left[\frac{d\epsilon}{\Omega_{\text{D}}} \left(\frac{\epsilon}{\Omega_{\text{D}}}\right)^4 \frac{l_{\text{pb}}(\epsilon)}{d} \right.\right.$$
$$\left.\left. \times \int_{\cos\left(\theta_{c,l}\right)}^{1} d\xi \xi T_l(\xi) \left(\frac{1 - e^{im\pi - \xi d/l_{\text{pb}}(\epsilon)}}{1 + m^2\pi^2 l_{\text{pb}}^2(\epsilon)\xi^2/d^2} - T_l(\xi)\left(1 - \cos\left(\theta_{c,l}\right)\right) \frac{1 - e^{im\pi - 2\xi d/l_{\text{pb}}(\epsilon)}}{4 + m^2\pi^2 l_{\text{pb}}^2(\epsilon)\xi^2/d^2} \right) \right] \right\} \tag{D.1}$$

Since longitudinal phonons have the highest cutoff energy for most materials, they are preferentially created during this stage of the down conversion. Therefore, we use the angle dependent longitudinal transmission coefficient, $T_l(\cos(\theta))$, to incorporate the acoustic mismatch at the boundary between detector and substrate. This parameter is calculated with the densities and speed of sounds presented in this appendix using the acoustic mismatch model discussed in detail in reference 170.

ζ is a placeholder parameter given in reference 168.

$$\zeta^2 = \frac{\pi^2 D}{6d^2} \left(\frac{4E_1}{\Omega_{\text{D}}}\right)^{2/3} \tau_s \tag{D.2}$$

In this equation, the first characteristic down-conversion energy, E_1, can sometimes be looked up in tables, but it should also never be greater than the incident photon energy. If E_1 is unknown, E_{photon} can be used instead as a reasonable proxy. The diffusion constant in equation D.2, D, can be estimated from the normal state conductivity, σ_n and the single-spin density of states, N_0 [179].

$$D = \frac{\sigma_n}{N_0 e^2}, \tag{D.3}$$

where here e is the electron charge.

$l_{\mathrm{pb}}(\epsilon)$ is the phonon mean free path with respect to pair breaking. The phonon mean-free-path can either be calculated from the lifetime and the appropriate speed of sound, $l_{\mathrm{pb}}(\epsilon) = c_s \tau_{\mathrm{pb}}(\epsilon)$. In this case, the speed of sound is the speed for longitudinal waves. For $\epsilon, \Delta \gg k_B T$, we can simplify equation 27 in reference 63 and see that the phonon lifetime is inversely related to the phonon energy.

$$\tau_{\mathrm{pb}}(\epsilon) = \frac{\hbar N}{4\pi N_0 \langle \alpha^2 \rangle \epsilon} \tag{D.4}$$

This equation allows us to reference the phonon mean-free-path or lifetime to the value at the Debye energy which can sometimes be found in published tables.

$$l_{\mathrm{pb}}(\epsilon) = \frac{\Omega_{\mathrm{D}}}{\epsilon} l_{\mathrm{pb,\,D}} \tag{D.5}$$

$$\tau_{\mathrm{pb}}(\epsilon) = \frac{\Omega_{\mathrm{D}}}{\epsilon} \tau_{\mathrm{pb,\,D}} \tag{D.6}$$

L is the $^1/_e$ absorption depth of photons in the superconductor. We use the skin depth for this value which can be calculated from the normal state conductivity and photon energy, E_{photon}. This is an order of magnitude estimate and is not particularly accurate.

$$L = \sqrt{\frac{h}{\pi \mu_0 \sigma_n E_{\text{photon}}}} \tag{D.7}$$

All other parameters used for this calculation are listed and described in tables D.1 and D.2.

D.2 Determining J_{low}

The formula for J_{low} is given in reference 129. With the correction from reference 167, we have

$$J_{\text{low}} = \eta_{\text{pb}} T_{\text{avg}} \left(1 - \cos(\theta_c)^2\right) \frac{\Omega_{\text{D}}}{\Delta} \frac{l_{\text{pb, D}}}{d} \frac{3(1+\lambda)}{11(1+\lambda)+3} g_1\left(\frac{\Omega_{\text{D}}}{\Omega_1}\right), \tag{D.8}$$

where $g_1(x)$ is given by

$$\begin{aligned} g_1(x) = \int_{1/x}^{1} dz f(z) \Bigg(& \text{Ei}\left[1, z(x-1)\right] - \text{Ei}\left[1, 1-z\right] + \ln\left[\frac{(x-1)z}{1-z}\right] \\ & - \frac{1}{4} T_{\text{avg}} (1 - \cos(\theta_c)) \left\{ \text{Ei}\left[1, 2z(x-1)\right] - \text{Ei}\left[1, 2(1-z)\right] + \ln\left[\frac{(x-1)z}{1-z}\right] \right\} \Bigg) \end{aligned} \tag{D.9}$$

and $f(x)$ is given by

$$f(x) = 1 - x - \frac{1}{12} x \left\{ x^2 \left[\cos\left(\sqrt{2} \ln x\right) - 7\sqrt{2} \sin\left(\sqrt{2} \ln x\right) \right] - 1 \right\}. \tag{D.10}$$

In the equations used to calculate J_{low}, there are several extra parameters that we need that were not present in the J_{high} calculation. We use the average transmission probability, T_{avg} across all phonon modes since the phonons in this stage do not have a preferred mode.

$$T_{\text{avg}} = \left(\frac{2T_t}{3c_t^2} + \frac{T_l}{3c_l^2}\right)c_{\text{avg}}^2, \tag{D.11}$$

where the average speed of sound is given by

$$c_{\text{avg}} = \left(\frac{1}{3c_l^3} + \frac{2}{3c_t^3}\right)^{-1/3}. \tag{D.12}$$

T_l and T_t are the angle averaged transmission coefficients computed from the acoustic mismatch model [170]. Similarly, the average speed of sound is used to compute the mean-free-path for these phonons and the critical angle, θ_c.

The second characteristic down conversion energy, Ω_1, can be found in tables for several materials [71]. When it is not available it can be calculated using [129]

$$\Omega_1 = \Omega_{\text{D}}\sqrt{\frac{2}{3}(1+\lambda)\Omega_{\text{D}}\frac{N_0}{N}}, \tag{D.13}$$

where N is the ion density. The electron-phonon coupling constant, λ, is also sometimes given in tables for different materials. When it is not available, it can be calculated from the transition temperature and the Coulomb pseudo-potential, $\mu^* \sim 0.13$, which is fairly constant among superconductors [51].

$$\lambda = \frac{1.04 + \mu^* \ln\left({}^{\Omega_{\text{D}}}/_{1.45 k_B T_c}\right)}{(1 - 0.62\mu^*)\ln\left({}^{\Omega_{\text{D}}}/_{1.45 k_B T_c}\right) - 1.04} \tag{D.14}$$

For both platinum silicide and hafnium, we find that the contribution from J_{low} is about two orders of magnitude lower than that from J_{high}. A similar trend is seen in reference 167 with aluminum resonators. This result indicates that blocking the first wave of phonons near the Debye energy should significantly improve the resolving power for either of these materials.

Symbol	Value	Description
F	0.2[c]	Fano factor [165, 166]
η_{pb}	0.59[c]	Pair breaking efficiency [71]
T_c	395 mK[a]	Superconducting transition temperature [67]
d	200 nm[a]	Hf film thickness [67]
Ω_D	21.7 meV[b]	Debye energy [51]
$\tau_{\text{pb, D}}$	14.7 ps[b]	Phonon lifetime [71]
E_1	586 meV[b]	Down conversion energy 1 [71]
Ω_1	5.12 meV[b]	Down conversion energy 2 [71]
τ_s	85 fs[b]	Electron-phonon scattering time [71]
σ_n	1.649×10^{6} S m^{-1} [a]	Normal state conductivity at 4 K [67]
ρ	12.871 g cm^{-3}[a]	Density [172]
c_l	3,786 m s^{-1}[b]	Longitudinal speed of sound [172]
c_t	2,053 m s^{-1}[b]	Transverse speed of sound [172]
N_0	1.965×10^{10} eV^{-1} μm^{-3}[b]	Single spin density of states [51]
λ	0.34[b]	Electron-phonon coupling [51]
E_{photon}	1.24 eV[a]	Photon energy at 1 μm
Δ	60 μeV	Superconducting gap $\sim 1.764 k_B T_c$
c_{avg}	2,291 m s^{-1}	Average speed of sound: equation D.12
T_{avg}	0.09	Average phonon transmission: equation D.11
$l_{\text{pb, D}}$	55.7 nm or 44.1 nm	Using $c_l \tau_{\text{pb, D}}$ for J_{high} or $c_{\text{avg}} \tau_{\text{pb, D}}$ for J_{low}
D	5.24 cm^2 s^{-1}	Diffusion constant: equation D.3
ζ	0.204	Equation D.2
L	22.6 nm	Optical penetration depth: equation D.7
$\theta_{c,l}$	35.9°	Longitudinal critical angle: reference 170
θ_c	18.7°	Average critical angle: reference 170
J_{high}	6.38	Equation D.1
J_{low}	0.0105	Equation D.8
R_{phonon}	18.3	Equation 6.2 at E_{photon}

[a] Measured
[b] Typical for hafnium
[c] Typical for superconductors

Table D.1: The parameters used in the evaluation of the phonon loss parameters, J_{high} and J_{low}, for hafnium on sapphire are tabulated here. The top half corresponds to known or estimated values. Parameters computed from those given above are listed on the bottom half. For the phonon transmission parameters, the speed of sound and density of the substrate are also needed for the calculation and can be found in table 6.1.

Symbol	Value	Description
F	0.2^{c}	Fano factor [165, 166]
η_{pb}	0.59^{c}	Pair breaking efficiency [71]
T_c	930 mK^{a}	Superconducting transition temperature [44]
d	50 nm^{a}	PtSi film thickness [44]
Ω_D	31 meV^{d}	Debye energy [186]
$\langle\alpha^2\rangle$	1.5 meV^{c}	Mean squared electron phonon interaction [63]
τ_s	66.4 fs^{c}	Electron-phonon scattering time [71]
σ_n	3.425 S m$^{-1\,b}$	Normal state conductivity at 4 K [127]
ρ	12.36 g cm$^{-3\,b}$	Density [187]
c_l	5,262.37 m s$^{-1\,d}$	Longitudinal speed of sound [186]
c_t	2,678.76 m s$^{-1\,d}$	Transverse speed of sound [186]
N_0/N	1 eV^{-1} ion^{-1} ^{d}	Single spin density of states per ion [186]
E_{photon}	1.24 eV^{a}	Photon energy at 1 μm
Δ	141 μeV	Superconducting gap $\sim 1.764 k_B T_c$
c_{avg}	3,002 m s^{-1}	Average speed of sound: equation D.12
T_{avg}	0.15	Average phonon transmission: equation D.11
N	3.34×10^{10} μm^{-3}	Number density: density and atomic weight
N_0	3.34×10^{10} eV^{-1} μm^{-3}	Single spin density of states
$\tau_{\mathrm{pb,\,D}}$	1.1 ps	Phonon lifetime: equation D.4
$l_{\mathrm{pb,\,D}}$	5.8 nm or 3.3 nm	Using $c_l\tau_{\mathrm{pb,\,D}}$ for J_{high} or $c_{\mathrm{avg}}\tau_{\mathrm{pb,\,D}}$ for J_{low}
D	6.41 cm^2 s	Diffusion constant: equation D.3
λ	0.43	Electron-phonon coupling: equation D.14
E_1	1.24 eV	Down conversion energy 1: E_{photon}
Ω_1	5.4 meV	Down conversion energy 2: equation D.13
ζ	1.01	Equation D.2
L	15.7 nm	Optical penetration depth: equation D.7
$\theta_{\mathrm{c,\,l}}$	54.7°	Longitudinal critical angle: reference 170
θ_c	26.5°	Average critical angle: reference 170
J_{high}	1.88	Equation D.1
J_{low}	0.0116	Equation D.8
R_{phonon}	21.1	Equation 6.2 at E_{photon}

[a] Measured
[b] Typical for platinum silicide
[c] Typical for superconductors
[d] Theory calculation

Table D.2: The parameters used in the evaluation of the phonon loss parameters, J_{high} and J_{low}, for platinum silicide on sapphire are tabulated here. The top half corresponds to known or estimated values. Parameters computed from those given above are listed on the bottom half. For the phonon transmission parameters, the speed of sound and density of the substrate are also needed for the calculation and can be found in table 6.1.

Bibliography

[1] K. Niwa, T. Numata, K. Hattori, and D. Fukuda, “Few-photon color imaging using energy-dispersive superconducting transition-edge sensor spectrometry”, Scientific Reports **7**, 45660 (2017) (Cited on pages 1, 11).

[2] M. Baryakhtar, J. Huang, and R. Lasenby, “Axion and hidden photon dark matter detection with multilayer optical haloscopes”, Physical Review D **98**, 035006 (2018) (Cited on page 1).

[3] J. J. Lissauer and J. Eisberg, “New Astronomy Reviews special issue: History of Kepler’s major exoplanet “firsts””, New Astronomy Reviews **83**, 1–4 (2018) (Cited on page 2).

[4] S. B. Howell, C. Sobeck, M. Haas, M. Still, T. Barclay, F. Mullally, J. Troeltzsch, S. Aigrain, S. T. Bryson, D. Caldwell, W. J. Chaplin, W. D. Cochran, D. Huber, G. W. Marcy, A. Miglio, J. R. Najita, M. Smith, J. D. Twicken, and J. J. Fortney, “The K2 Mission: Characterization and Early Results”, Publications of the Astronomical Society of the Pacific **126**, 398–408 (2014) (Cited on page 2).

[5] G. Basri, W. J. Borucki, and D. Koch, “The Kepler Mission: A wide-field transit search for terrestrial planets”, New Astronomy Reviews **49**, Wide-Field Imaging from Space, 478–485 (2005) (Cited on page 2).

[6] NASA Exoplanet Science Institute, *Planetary Systems Composite Table*, (2022) https://doi.org/10.26133/NEA13 (visited on 02/02/2022) (Cited on page 3).

[7] J. Chilcote, Q. Konopacky, R. J. D. Rosa, R. Hamper, B. Macintosh, C. Marois, M. D. Perrin, D. Savransky, R. Soummer, J.-P. Véran, G. Agapito, A. Aleman, S. M. Ammons, M. Bonaglia, M.-A. Boucher, M. Curliss, J. Dunn, S. Esposito, G. Filion, J. Fitzsimmons, I. Kain, D. Kerley, J.-T. Landry, O. Lardiere, M. Lemoine-Busserolle, D. Li, M. A. Limbach, A. Madurowicz, J. Maire, M. N’Diaye, E. L. Nielsen, L. Poyneer, L. Pueyo, K. Summey, and C. Thomas, “GPI 2.0: upgrading the Gemini Planet Imager”, in Ground-based and Airborne Instrumentation for Astronomy VIII, Vol. 11447, edited by C. J. Evans, J. J. Bryant, and K. Motohara (International Society for Optics and Photonics, 2020), pp. 394–407 (Cited on page 4).

[8] B. Macintosh, J. R. Graham, P. Ingraham, Q. Konopacky, C. Marois, M. Perrin, L. Poyneer, B. Bauman, T. Barman, A. S. Burrows, A. Cardwell, J. Chilcote, R. J. De Rosa, D. Dillon, R. Doyon, J. Dunn, D. Erikson, M. P. Fitzgerald, D. Gavel, S. Goodsell, M. Hartung, P. Hibon, P. Kalas, J. Larkin, J. Maire, F. Marchis, M. S. Marley, J. McBride, M. Millar-Blanchaer, K. Morzinski, A. Norton, B. R. Oppenheimer, D. Palmer, J. Patience, L. Pueyo, F. Rantakyro, N. Sadakuni, L. Saddlemyer, D. Savransky, A. Serio, R. Soummer, A. Sivaramakrishnan, I. Song, S. Thomas, J. K. Wallace, S. Wiktorowicz, and S. Wolff, "First light of the Gemini Planet Imager", Proceedings of the National Academy of Sciences **111**, 12661–12666 (2014) (Cited on page 4).

[9] Beuzit, J.-L., Vigan, A., Mouillet, D., Dohlen, K., Gratton, R., Boccaletti, A., Sauvage, J.-F., Schmid, H. M., Langlois, M., Petit, C., Baruffolo, A., Feldt, M., Milli, J., Wahhaj, Z., Abe, L., Anselmi, U., Antichi, J., Barette, R., Baudrand, J., Baudoz, P., Bazzon, A., Bernardi, P., Blanchard, P., Brast, R., Bruno, P., Buey, T., Carbillet, M., Carle, M., Cascone, E., Chapron, F., Charton, J., Chauvin, G., Claudi, R., Costille, A., De Caprio, V., de Boer, J., Delboulbé, A., Desidera, S., Dominik, C., Downing, M., Dupuis, O., Fabron, C., Fantinel, D., Farisato, G., Feautrier, P., Fedrigo, E., Fusco, T., Gigan, P., Ginski, C., Girard, J., Giro, E., Gisler, D., Gluck, L., Gry, C., Henning, T., Hubin, N., Hugot, E., Incorvaia, S., Jaquet, M., Kasper, M., Lagadec, E., Lagrange, A.-M., Le Coroller, H., Le Mignant, D., Le Ruyet, B., Lessio, G., Lizon, J.-L., Llored, M., Lundin, L., Madec, F., Magnard, Y., Marteaud, M., Martinez, P., Maurel, D., Ménard, F., Mesa, D., Möller-Nilsson, O., Moulin, T., Moutou, C., Origné, A., Parisot, J., Pavlov, A., Perret, D., Pragt, J., Puget, P., Rabou, P., Ramos, J., Reess, J.-M., Rigal, F., Rochat, S., Roelfsema, R., Rousset, G., Roux, A., Saisse, M., Salasnich, B., Santambrogio, E., Scuderi, S., Segransan, D., Sevin, A., Siebenmorgen, R., Soenke, C., Stadler, E., Suarez, M., Tiphène, D., Turatto, M., Udry, S., Vakili, F., Waters, L. B. F. M., Weber, L., Wildi, F., Zins, G., and Zurlo, A., "SPHERE: the exoplanet imager for the Very Large Telescope", Astronomy & Astrophysics **631**, A155 (2019) (Cited on page 4).

[10] K. Ahn, O. Guyon, J. Lozi, S. Vievard, V. Deo, N. Skaf, R. Belikov, S. P. Bos, M. Bottom, T. Currie, R. Frazin, K. V. Gorkom, T. D. Groff, S. Y. Haffert, N. Jovanovic, H. Kawahara, T. Kotani, J. R. Males, F. Martinache, B. Mazin, K. Miller, B. Norris, A. Rodack, and A. Wong, "SCExAO: a testbed for developing high-contrast imaging technologies for ELTs", in Techniques and Instrumentation for Detection of Exoplanets X, Vol. 11823, edited by S. B. Shaklan and G. J. Ruane (International Society for Optics and Photonics, 2021), pp. 9–21 (Cited on page 4).

[11] N. Jovanovic, F. Martinache, O. Guyon, C. Clergeon, G. Singh, T. Kudo, V. Garrel, K. Newman, D. Doughty, J. Lozi, J. Males, Y. Minowa, Y. Hayano, N. Takato, J. Morino, J. Kuhn, E. Serabyn, B. Norris, P. Tuthill, G. Schworer, P. Stewart, L. Close, E. Huby, G. Perrin, S. Lacour, L. Gauchet, S. Vievard, N. Murakami, F. Oshiyama, N. Baba, T. Matsuo, J. Nishikawa, M. Tamura, O. Lai, F. Marchis, G. Duchene, T. Kotani, and J. Woillez, "The Subaru Coronagraphic Extreme Adaptive Optics System: Enabling High-Contrast Imaging on Solar-System Scales", Publications of the Astronomical Society of the Pacific **127**, 890–910 (2015) (Cited on page 4).

[12] S. Hinkley, B. R. Oppenheimer, N. Zimmerman, D. Brenner, I. R. Parry, J. R. Crepp, G. Vasisht, E. Ligon, D. King, R. Soummer, A. Sivaramakrishnan, C. Beichman, M. Shao, L. C. Roberts, A. Bouchez, R. Dekany, L. Pueyo, J. E. Roberts, T. Lockhart, C. Zhai, C. Shelton, and R. Burruss, "A New High Contrast Imaging Program at Palomar Observatory", Publications of the Astronomical Society of the Pacific **123**, 74–86 (2011) (Cited on page 4).

[13] M. Bottom, J. C. Shelton, J. K. Wallace, R. Bartos, J. Kuhn, D. Mawet, B. Mennesson, R. Burruss, and E. Serabyn, "Stellar Double Coronagraph: A Multistage Coronagraphic Platform at Palomar Observatory", Publications of the Astronomical Society of the Pacific **128**, 075003 (2016) (Cited on page 4).

[14] J.-R. Delorme, N. Jovanovic, D. Echeverri, D. P. Mawet, J. K. Wallace, R. D. Bartos, S. Cetre, P. L. Wizinowich, S. Ragland, S. J. Lilley, E. Wetherell, G. Doppmann, J. J. Wang, E. C. Morris, J.-B. Ruffio, E. C. Martin, M. P. Fitzgerald, G. J. Ruane, T. Schofield, N. Suominen, B. Calvin, E. Wang, K. G. Magnone, C. A. Johnson, J. M. Sohn, R. A. Lopez, C. Z. Bond, J. Pezzato, J. Llop-Sayson, M. R. Chun, and A. J. Skemer, "Keck Planet Imager and Characterizer: a dedicated single-mode fiber injection unit for high-resolution exoplanet spectroscopy", Journal of Astronomical Telescopes, Instruments, and Systems **7**, 1–25 (2021) (Cited on page 4).

[15] J. R. Males, L. M. Close, O. Guyon, A. D. Hedglen, K. Van Gorkom, J. D. Long, M. Y. Kautz, J. Lumbres, L. Schatz, A. T. Rodack, K. L. Miller, D. S. Doelman, F. Snik, J. M. Knight, K. M. Morzinski, V. Gasho, C. U. Keller, S. Y. Haffert, and L. Pearce, "MagAO-X first light", in Adaptive Optics Systems VII, edited by D. Schmidt, L. Schreiber, and E. Vernet (Dec. 2020), p. 218 (Cited on page 4).

[16] F. Martinache, O. Guyon, N. Jovanovic, C. Clergeon, G. Singh, T. Kudo, T. Currie, C. Thalmann, M. McElwain, and M. Tamura, "On-Sky Speckle Nulling Demon-

stration at Small Angular Separation with SCExAO", Publications of the Astronomical Society of the Pacific **126**, 565–572 (2014) (Cited on page 4).

[17] M. Bottom, B. Femenia, E. Huby, D. Mawet, R. Dekany, J. Milburn, and E. Serabyn, "Speckle nulling wavefront control for Palomar and Keck", in Adaptive Optics Systems V, Vol. 9909, edited by E. Marchetti, L. M. Close, and J.-P. Véran (International Society for Optics and Photonics, 2016), pp. 1507–1522 (Cited on page 4).

[18] B. S. Gaudi, S. Seager, B. Mennesson, A. Kiessling, K. Warfield, K. Cahoy, J. T. Clarke, S. Domagal-Goldman, L. Feinberg, O. Guyon, J. Kasdin, D. Mawet, P. Plavchan, T. Robinson, L. Rogers, P. Scowen, R. Somerville, K. Stapelfeldt, C. Stark, D. Stern, M. Turnbull, R. Amini, G. Kuan, S. Martin, R. Morgan, D. Redding, H. P. Stahl, R. Webb, O. Alvarez-Salazar, W. L. Arnold, M. Arya, B. Balasubramanian, M. Baysinger, R. Bell, C. Below, J. Benson, L. Blais, J. Booth, R. Bourgeois, C. Bradford, A. Brewer, T. Brooks, E. Cady, M. Caldwell, R. Calvet, S. Carr, D. Chan, V. Cormarkovic, K. Coste, C. Cox, R. Danner, J. Davis, L. Dewell, L. Dorsett, D. Dunn, M. East, M. Effinger, R. Eng, G. Freebury, J. Garcia, J. Gaskin, S. Greene, J. Hennessy, E. Hilgemann, B. Hood, W. Holota, S. Howe, P. Huang, T. Hull, R. Hunt, K. Hurd, S. Johnson, A. Kissil, B. Knight, D. Kolenz, O. Kraus, J. Krist, M. Li, D. Lisman, M. Mandic, J. Mann, L. Marchen, C. Marrese-Reading, J. McCready, J. McGown, J. Missun, A. Miyaguchi, B. Moore, B. Nemati, S. Nikzad, J. Nissen, M. Novicki, T. Perrine, C. Pineda, O. Polanco, D. Putnam, A. Qureshi, M. Richards, A. J. E. Riggs, M. Rodgers, M. Rud, N. Saini, D. Scalisi, D. Scharf, K. Schulz, G. Serabyn, N. Sigrist, G. Sikkia, A. Singleton, S. Shaklan, S. Smith, B. Southerd, M. Stahl, J. Steeves, B. Sturges, C. Sullivan, H. Tang, N. Taras, J. Tesch, M. Therrell, H. Tseng, M. Valente, D. V. Buren, J. Villalvazo, S. Warwick, D. Webb, T. Westerhoff, R. Wofford, G. Wu, J. Woo, M. Wood, J. Ziemer, G. Arney, J. Anderson, J. Maíz-Apellániz, J. Bartlett, R. Belikov, E. Bendek, B. Cenko, E. Douglas, S. Dulz, C. Evans, V. Faramaz, Y. K. Feng, H. Ferguson, K. Follette, S. Ford, M. García, M. Geha, D. Gelino, Y. Götberg, S. Hildebrandt, R. Hu, K. Jahnke, G. Kennedy, L. Kreidberg, A. Isella, E. Lopez, F. Marchis, L. Macri, M. Marley, W. Matzko, J. Mazoyer, S. McCandliss, T. Meshkat, C. Mordasini, P. Morris, E. Nielsen, P. Newman, E. Petigura, M. Postman, A. Reines, A. Roberge, I. Roederer, G. Ruane, E. Schwieterman, D. Sirbu, C. Spalding, H. Teplitz, J. Tumlinson, N. Turner, J. Werk, A. Wofford, M. Wyatt, A. Young, and R. Zellem, "The Habitable Exoplanet Observatory (HabEx) Mission Concept Study Final Report", 2020, arXiv:2001.06683 [astro-ph.IM] (Cited on pages 4, 8).

[19] The LUVOIR Team, "The LUVOIR Mission Concept Study Final Report", 2019, arXiv:1912.06219 [astro-ph.IM] (Cited on pages 4, 8).

[20] National Academies of Sciences, Engineering, and Medicine, "Pathways to Discovery in Astronomy and Astrophysics for the 2020s" (The National Academies Press, Washington, DC, 2021) (Cited on page 4).

[21] M. C. Turnbull, W. A. Traub, K. W. Jucks, N. J. Woolf, M. R. Meyer, N. Gorlova, M. F. Skrutskie, and J. C. Wilson, "Spectrum of a Habitable World: Earthshine in the Near-Infrared", The Astrophysical Journal **644**, 551–559 (2006) (Cited on pages 5, 6).

[22] L. Kaltenegger, W. A. Traub, and K. W. Jucks, "Spectral Evolution of an Earth-like Planet", The Astrophysical Journal **658**, 598–616 (2007) (Cited on page 6).

[23] B. J. Rauscher, E. R. Canavan, S. H. Moseley, J. E. Sadleir, and T. Stevenson, "Detectors and cooling technology for direct spectroscopic biosignature characterization", Journal of Astronomical Telescopes, Instruments, and Systems **2**, 041212 (2016) (Cited on pages 7, 8, 109).

[24] C. C. Stark, A. Roberge, A. Mandell, M. Clampin, S. D. Domagal-Goldman, M. W. McElwain, and K. R. Stapelfeldt, "LOWER LIMITS ON APERTURE SIZE FOR AN EXOEARTH DETECTING CORONAGRAPHIC MISSION", The Astrophysical Journal **808**, 149 (2015) (Cited on pages 7, 108).

[25] L. K. Harding, R. T. Demers, M. Hoenk, P. Peddada, B. Nemati, M. Cherng, D. Michaels, L. S. Neat, A. Loc, N. Bush, D. Hall, N. Murray, J. Gow, R. Burgon, A. Holland, A. Reinheimer, P. R. Jorden, and D. Jordan, "Technology advancement of the CCD201-20 EMCCD for the WFIRST coronagraph instrument: sensor characterization and radiation damage", Journal of Astronomical Telescopes, Instruments, and Systems **2**, 011007 (2015) (Cited on page 8).

[26] K. Karatsu, A. Dominjon, T. Fujino, T. Funaki, M. Hazumi, F. Irie, H. Ishino, Y. Kida, T. Matsumura, K. Mizukami, M. Naruse, T. Nitta, T. Noguchi, N. Oka, S. Sekiguchi, Y. Sekimoto, M. Sekine, S. Shu, Y. Yamada, and T. Yamashita, "Radiation Tolerance of Aluminum Microwave Kinetic Inductance Detector", Journal of Low Temperature Physics **184**, 540–546 (2016) (Cited on page 9).

[27] N. Fruitwala, "Readout and Calibration of Large Format Optical / IR MKID Arrays and Applications to Focal Plane Wavefront Control", PhD thesis (UC Santa Barbara, 2021) (Cited on pages 10, 108).

[28] A. B. Walter, C. Bockstiegel, T. D. Brandt, and B. A. Mazin, “Stochastic Speckle Discrimination with Time-tagged Photon Lists: Digging below the Speckle Noise Floor”, Publications of the Astronomical Society of the Pacific **131**, 114506 (2019) (Cited on pages 10, 108).

[29] P. L. Richards, “Bolometers for infrared and millimeter waves”, Journal of Applied Physics **76**, 1–24 (1994) (Cited on page 10).

[30] K. D. Irwin and G. C. Hilton, “Transition-edge sensors”, in *Topics in Applied Physics: Cryogenic Particle Detection*, Vol. 99 (2005) Chap. 3, pp. 63–152 (Cited on page 10).

[31] T. May, V. Zakosarenko, E. Kreysa, W. Esch, S. Anders, H.-P. Gemuend, E. Heinz, and H.-G. Meyer, “Design, realization, and characteristics of a transition edge bolometer for sub-millimeter wave astronomy”, Review of Scientific Instruments **83**, 114502 (2012) (Cited on page 11).

[32] J. N. Ullom and D. A. Bennett, “Review of superconducting transition-edge sensors for x-ray and gamma-ray spectroscopy”, Superconductor Science and Technology **28**, 084003 (2015) (Cited on page 11).

[33] B. Cabrera, R. M. Clarke, P. Colling, A. J. Miller, S. Nam, and R. W. Romani, “Detection of single infrared, optical, and ultraviolet photons using superconducting transition edge sensors”, Applied Physics Letters **73**, 735–737 (1998) (Cited on page 11).

[34] D. Fukuda, K. Niwa, K. Hattori, S. Inoue, R. Kobayashi, and T. Numata, “Confocal Microscopy Imaging with an Optical Transition Edge Sensor”, Journal of Low Temperature Physics **193**, 1228–1235 (2018) (Cited on page 11).

[35] S. A. Kernasovskiy, S. E. Kuenstner, E. Karpel, Z. Ahmed, D. D. Van Winkle, S. Smith, J. Dusatko, J. C. Frisch, S. Chaudhuri, H. M. Cho, B. J. Dober, S. W. Henderson, G. C. Hilton, J. Hubmayr, K. D. Irwin, C. L. Kuo, D. Li, J. A. B. Mates, M. Nasr, S. Tantawi, J. Ullom, L. Vale, and B. Young, “SLAC Microresonator Radio Frequency (SMuRF) Electronics for Read Out of Frequency-Division-Multiplexed Cryogenic Sensors”, Journal of Low Temperature Physics **193**, 570–577 (2018) (Cited on pages 11, 32).

[36] J. Burney, T. Bay, J. Barral, P. Brink, B. Cabrera, J. Castle, A. Miller, S. Nam, D. Rosenberg, R. Romani, and A. Tomada, “Transition-edge sensor arrays for UV-optical-IR astrophysics”, Nuclear Instruments and Methods in Physics Research Section A: Accelerators, Spectrometers, Detectors and Associated Equipment **559**, 525–527 (2006) (Cited on page 11).

[37] E. Burstein, D. N. Langenberg, and B. N. Taylor, “Superconductors as quantum detectors for microwave and sub-millimeter-wave radiation”, Physical Review Letters **6**, 92–94 (1961) (Cited on page 11).

[38] A. Peacock, P. Verhoeve, N. Rando, A. van Dordrecht, B. G. Taylor, C. Erd, M. A. C. Perryman, R. Venn, J. Howlett, D. J. Goldie, J. Lumley, and M. Wallis, “Single optical photon detection with a superconducting tunnel junction”, Nature **381**, 135–137 (1996) (Cited on page 11).

[39] D. D. E. Martin, P. Verhoeve, A. Peacock, A. G. Kozorezov, J. K. Wigmore, H. Rogalla, and R. Venn, “Resolution limitation due to phonon losses in superconducting tunnel junctions”, Applied Physics Letters **88**, 123510 (2006) (Cited on pages 11, 88).

[40] P. Verhoeve, D. Martin, R. Hijmering, J. Verveer, A. van Dordrecht, G. Sirbi, T. Oosterbroek, and A. Peacock, “S-Cam 3: Optical astronomy with a STJ-based imaging spectrophotometer”, Nuclear Instruments and Methods in Physics Research Section A: Accelerators, Spectrometers, Detectors and Associated Equipment **559**, 598–601 (2006) (Cited on page 11).

[41] P. K. Day, H. G. LeDuc, B. A. Mazin, A. Vayonakis, and J. Zmuidzinas, “A broadband superconducting detector suitable for use in large arrays”, Nature **425**, 817–821 (2003) (Cited on pages 12, 23).

[42] J. Zmuidzinas, “Superconducting Microresonators: Physics and Applications”, Annual Review of Condensed Matter Physics **3**, 169–214 (2012) (Cited on pages 12, 25, 31, 34, 58, 66, 125).

[43] S. R. Meeker, B. A. Mazin, R. Jensen-Clem, A. B. Walter, P. Szypryt, M. J. Strader, and C. Bockstiegel, “Design and Development Status of MKID Integral Field Spectrographs for High Contrast Imaging Design and Development Status of MKID Integral Field Spectrographs for High Contrast Imaging”, in Adaptive Optics for Extremely Large Telescopes 4, Vol. 1, 1 (2015) (Cited on pages 13, 50).

[44] P. Szypryt, S. R. Meeker, G. Coiffard, N. Fruitwala, B. Bumble, G. Ulbricht, A. B. Walter, M. Daal, C. Bockstiegel, G. Collura, **N. Zobrist**, I. Lipartito, and B. A. Mazin, “Large-format platinum silicide microwave kinetic inductance detectors for optical to near-IR astronomy”, Optics Express **25**, 25894 (2017) (Cited on pages 13, 49, 52, 54, 60, 61, 63, 80, 145).

[45] B. A. Mazin, S. R. Meeker, M. J. Strader, P. Szypryt, D. Marsden, J. C. van Eyken, G. E. Duggan, A. B. Walter, G. Ulbricht, M. Johnson, B. Bumble, K. O'Brien, and C. Stoughton, "ARCONS: A 2024 Pixel Optical through Near-IR Cryogenic Imaging Spectrophotometer", Publications of the Astronomical Society of the Pacific **125**, 1348–1361 (2013) (Cited on pages 13, 50, 51, 63, 109).

[46] S. R. Meeker, B. A. Mazin, A. B. Walter, P. Strader, N. Fruitwala, C. Bockstiegel, P. Szypryt, G. Ulbricht, G. Coiffard, B. Bumble, G. Cancelo, T. Zmuda, K. Treptow, N. Wilcer, G. Collura, R. Dodkins, I. Lipartito, **N. Zobrist**, M. Bottom, J. C. Shelton, D. Mawet, J. C. van Eyken, G. Vasisht, and E. Serabyn, "DARKNESS: A Microwave Kinetic Inductance Detector Integral Field Spectrograph for High-contrast Astronomy", Publications of the Astronomical Society of the Pacific **130**, 065001 (2018) (Cited on pages 13, 50, 109).

[47] A. B. Walter, N. Fruitwala, S. Steiger, J. I. Bailey, **N. Zobrist**, N. Swimmer, I. Lipartito, J. P. Smith, S. R. Meeker, C. Bockstiegel, G. Coiffard, R. Dodkins, P. Szypryt, K. K. Davis, M. Daal, B. Bumble, G. Collura, O. Guyon, J. Lozi, S. Vievard, N. Jovanovic, F. Martinache, T. Currie, and B. A. Mazin, "The MKID Exoplanet Camera for Subaru SCExAO", Publications of the Astronomical Society of the Pacific **132**, 125005 (2020) (Cited on pages 14, 50, 109).

[48] J. Bardeen, L. N. Cooper, and J. R. Schrieffer, "Theory of superconductivity", Physical Review **108**, 1175–1204 (1957) (Cited on page 15).

[49] G. M. Éliashberg, "Interactions between electrons and lattice vibrations in a superconductor", translated by R. T. Beyer, Journal of Experimental and Theoretical Physics **11**, 696–702 (1960), [Zhurnal Eksperimental'noi i Teoreticheskoi Fiziki **38**, 966 (1960)] (Cited on page 16).

[50] G. Grimvall, "The electron-phonon interaction in normal metals", Physica Scripta **14**, 63–78 (1976) (Cited on page 17).

[51] W. L. McMillan, "Transition Temperature of Strong-Coupled Superconductors", Physical Review **167**, 331–344 (1968) (Cited on pages 17, 95, 100, 106, 142, 144).

[52] S. B. Nam, "Theory of electromagnetic properties of superconducting and normal systems. I", Physical Review **156**, 470–486 (1967) (Cited on pages 18, 25).

[53] S. Gueron, "Quasiparticles in a diffusive conductor: interaction and pairing", PhD thesis (Université Pierre et Marie Curie - Paris VI, 1997) (Cited on pages 19, 22).

[54] A. A. Abrikosov and L. P. Gor'kov, "Contribution to the theory of superconducting alloys with paramagnetic impurities", Zhurnal Eksperimental'noi i Teoreticheskoi Fiziki **39** (1960) (Cited on page 20).

[55] R. C. Dynes, J. P. Garno, G. B. Hertel, and T. P. Orlando, "Tunneling study of superconductivity near the metal-insulator transition", Physical Review Letters **53**, 2437–2440 (1984) (Cited on page 20).

[56] A. Mikhailovsky, S. Shulga, A. Karakozov, O. Dolgov, and E. Maksimov, "Thermal pair-breaking in superconductors with strong electron-phonon interaction", Solid State Communications **80**, 511–515 (1991) (Cited on page 20).

[57] F. Herman and R. Hlubina, "Microscopic interpretation of the Dynes formula for the tunneling density of states", Physical Review B **94**, 144508 (2016) (Cited on pages 20, 59).

[58] J. Rammer and H. Smith, "Quantum field-theoretical methods in transport theory of metals", Reviews of Modern Physics **58**, 323–359 (1986) (Cited on pages 20, 22).

[59] K. D. Usadel, "Generalized diffusion equation for superconducting alloys", Physical Review Letters **25**, 507–509 (1970) (Cited on page 20).

[60] I. Kellett, "Circuit Theory of Mesoscopic Superconducting Components", Master's Thesis (Chalmers University of Technology, 2011) (Cited on page 21).

[61] J. A. Ouassou, "Density of States and Critical Temperature in Superconductor / Ferromagnet Structures with Spin-Orbit Coupling", Master's Thesis (Norwegian University of Science and Technology, 2015) (Cited on page 21).

[62] B. Mitrović and L. A. Rozema, "On the correct formula for the lifetime broadened superconducting density of states", Journal of Physics Condensed Matter **20**, 3–7 (2008) (Cited on page 21).

[63] S. B. Kaplan, C. C. Chi, D. N. Langenberg, J. J. Chang, S. Jafarey, and D. J. Scalapino, "Quasiparticle and phonon lifetimes in superconductors", Physical Review B **14**, 4854–4873 (1976) (Cited on pages 21, 140, 145).

[64] J. Gao, M. R. Vissers, M. O. Sandberg, F. C. S. da Silva, S. W. Nam, D. P. Pappas, D. S. Wisbey, E. C. Langman, S. R. Meeker, B. A. Mazin, H. G. Leduc, J. Zmuidzinas, and K. D. Irwin, "A titanium-nitride near-infrared kinetic inductance photon-counting detector and its anomalous electrodynamics", Applied Physics Letters **101**, 142602 (2012) (Cited on pages 22, 58, 59, 101).

[65] E. F. C. Driessen, P. C. J. J. Coumou, R. R. Tromp, P. J. de Visser, and T. M. Klapwijk, “Strongly Disordered TiN and NbTiN s-Wave Superconductors Probed by Microwave Electrodynamics”, Physical Review Letters **109**, 107003 (2012) (Cited on pages 22, 59).

[66] T. Noguchi, A. Dominjon, and Y. Sekimoto, “Analysis of Characteristics of Al MKID Resonators”, IEEE Transactions on Applied Superconductivity **28**, 1–6 (2018) (Cited on pages 22, 59).

[67] **N. Zobrist**, G. Coiffard, B. Bumble, N. Swimmer, S. Steiger, M. Daal, G. Collura, A. B. Walter, C. Bockstiegel, N. Fruitwala, I. Lipartito, and B. A. Mazin, “Design and performance of hafnium optical and near-IR kinetic inductance detectors”, Applied Physics Letters **115**, 213503 (2019) (Cited on pages 22, 33, 64, 91, 101, 144).

[68] G. Brammertz, A. Poelaert, A. A. Golubov, P. Verhoeve, A. Peacock, and H. Rogalla, “Generalized proximity effect model in superconducting bi- and trilayer films”, Journal of Applied Physics **90**, 355–364 (2001) (Cited on page 22).

[69] S. Zhao, D. J. Goldie, S. Withington, and C. N. Thomas, “Exploring the performance of thin-film superconducting multilayers as kinetic inductance detectors for low-frequency detection”, Superconductor Science and Technology **31**, 015007 (2018) (Cited on pages 22, 28, 99).

[70] A. Wallraff, D. I. Schuster, A. Blais, L. Frunzio, R. S. Huang, J. Majer, S. Kumar, S. M. Girvin, and R. J. Schoelkopf, “Strong coupling of a single photon to a superconducting qubit using circuit quantum electrodynamics”, Nature **431**, 162–167 (2004) (Cited on page 23).

[71] A. G. Kozorezov, A. F. Volkov, J. K. Wigmore, A. Peacock, A. Poelaert, and R. den Hartog, “Quasiparticle-phonon downconversion in nonequilibrium superconductors”, Physical Review B **61**, 11807–11819 (2000) (Cited on pages 24, 53, 89, 90, 105, 106, 142, 144, 145).

[72] W. Eisenmenger, “Nonequilibrium phonons”, in *Nonequilibrium Superconductivity, Phonons, and Kapitza Boundaries*, edited by K. E. Gray (Springer US, Boston, MA, 1981), pp. 73–109 (Cited on page 24).

[73] C. N. Thomas, S. Withington, and D. J. Goldie, “Electrothermal model of kinetic inductance detectors”, Superconductor Science and Technology **28**, 045012 (2015) (Cited on pages 24, 25, 31, 125).

[74] J. Aumentado, M. W. Keller, J. M. Martinis, and M. H. Devoret, “Nonequilibrium Quasiparticles and $2e$ Periodicity in Single-Cooper-Pair Transistors”, Physical Review Letters **92**, 066802 (2004) (Cited on page 24).

[75] A. J. Ferguson, N. A. Court, F. E. Hudson, and R. G. Clark, “Microsecond Resolution of Quasiparticle Tunneling in the Single-Cooper-Pair Transistor”, Physical Review Letters **97**, 106603 (2006) (Cited on page 24).

[76] P. J. de Visser, J. J. A. Baselmans, P. Diener, S. J. C. Yates, A. Endo, and T. M. Klapwijk, “Number Fluctuations of Sparse Quasiparticles in a Superconductor”, Physical Review Letters **106**, 167004 (2011) (Cited on pages 24, 49).

[77] J. M. Martinis, M. Ansmann, and J. Aumentado, “Energy Decay in Superconducting Josephson-Junction Qubits from Nonequilibrium Quasiparticle Excitations”, Physical Review Letters **103**, 097002 (2009) (Cited on page 24).

[78] O. Naaman and J. Aumentado, “Narrow-Band Microwave Radiation from a Biased Single-Cooper-Pair Transistor”, Physical Review Letters **98**, 227001 (2007) (Cited on page 24).

[79] B. S. Palmer, C. A. Sanchez, A. Naik, M. A. Manheimer, J. F. Schneiderman, P. M. Echternach, and F. C. Wellstood, “Steady-state thermodynamics of nonequilibrium quasiparticles in a Cooper-pair box”, Physical Review B **76**, 054501 (2007) (Cited on page 24).

[80] P. J. De Visser, D. J. Goldie, P. Diener, S. Withington, J. J. Baselmans, and T. M. Klapwijk, “Evidence of a nonequilibrium distribution of quasiparticles in the microwave response of a superconducting aluminum resonator”, Physical Review Letters **112**, 1–5 (2014) (Cited on pages 24, 59, 118).

[81] I. Nsanzineza and B. L. T. Plourde, “Trapping a Single Vortex and Reducing Quasiparticles in a Superconducting Resonator”, Physical Review Letters **113**, 117002 (2014) (Cited on page 24).

[82] F. Henriques, F. Valenti, T. Charpentier, M. Lagoin, C. Gouriou, M. Martínez, L. Cardani, M. Vignati, L. Grünhaupt, D. Gusenkova, J. Ferrero, S. T. Skacel, W. Wernsdorfer, A. V. Ustinov, G. Catelani, O. Sander, and I. M. Pop, “Phonon traps reduce the quasiparticle density in superconducting circuits”, Applied Physics Letters **115**, 212601 (2019) (Cited on page 24).

[83] W. H. Parker, “Modified heating theory of nonequilibrium superconductors”, Physical Review B **12**, 3667–3672 (1975) (Cited on pages 25, 62).

[84] M. A. Lindeman, “Resonator-bolometer theory, microwave read out, and kinetic inductance bolometers”, Journal of Applied Physics **116**, 024506 (2014) (Cited on page 25).

[85] S. Agrawal, B. Steinbach, J. J. Bock, C. Frez, L. Minutolo, H. Nguyen, R. O’Brient, A. Turner, and A. Wandui, “Strong negative electrothermal feedback in thermal kinetic inductance detectors”, Journal of Applied Physics **130**, 124503 (2021) (Cited on page 25).

[86] R. M. J. Janssen, A. Endo, P. J. de Visser, T. M. Klapwijk, and J. J. A. Baselmans, “Equivalence of optical and electrical noise equivalent power of hybrid NbTiN-Al microwave kinetic inductance detectors”, Applied Physics Letters **105**, 193504 (2014) (Cited on page 25).

[87] D. C. Mattis and J. Bardeen, “Theory of the Anomalous Skin Effect in Normal and Superconducting Metals”, Physical Review **111**, 412–417 (1958) (Cited on pages 25, 59).

[88] F. Herman and R. Hlubina, “Electromagnetic properties of impure superconductors with pair-breaking processes”, Physical Review B **96**, 014509 (2017) (Cited on pages 26, 59).

[89] C. S. Owen and D. J. Scalapino, “Superconducting State under the Influence of External Dynamic Pair Breaking”, Physical Review Letters **28**, 1559–1561 (1972) (Cited on page 26).

[90] J. Gao, J. Zmuidzinas, A. Vayonakis, P. Day, B. Mazin, and H. Leduc, “Equivalence of the Effects on the Complex Conductivity of Superconductor due to Temperature Change and External Pair Breaking”, Journal of Low Temperature Physics **151**, 557–563 (2008) (Cited on page 26).

[91] G. A. Sai-Halasz, C. C. Chi, A. Denenstein, and D. N. Langenberg, “Effects of Dynamic External Pair Breaking in Superconducting Films”, Physical Review Letters **33**, 215–219 (1974) (Cited on page 26).

[92] P. Hu, R. C. Dynes, and V. Narayanamurti, “Dynamics of quasiparticles in superconductors”, Physical Review B **10**, 2786–2788 (1974) (Cited on page 26).

[93] J. Gao, “The Physics of Superconducting Microwave Resonators”, PhD thesis (California Institute of Technology, 2008) (Cited on pages 27, 31, 38, 82, 125).

[94] S. B. Nam, “Theory of Electromagnetic Properties of Strong-Coupling and Impure Superconductors. II”, Physical Review **156**, 487–493 (1967) (Cited on page 27).

[95] A. R. Kerr, “Surface Impedance of Superconductors and Normal Conductors in EM Simulators”, ALMA Memos (1999) (Cited on page 28).

[96] D. Pozar, "Microwave Engineering", 4th (John Wiley & Sons, Hoboken, NJ, 2012) (Cited on pages 28, 115, 130).

[97] K. L. Geerlings, "Improving Coherence of Superconducting Qubits and Resonators", PhD thesis (Yale, 2013) (Cited on pages 29, 117).

[98] M. S. Khalil, M. J. A. Stoutimore, F. C. Wellstood, and K. D. Osborn, "An analysis method for asymmetric resonator transmission applied to superconducting devices", Journal of Applied Physics **111**, 054510 (2012) (Cited on pages 29, 117).

[99] F. W. Carter, T. S. Khaire, V. Novosad, and C. L. Chang, "scraps: An Open-Source Python-Based Analysis Package for Analyzing and Plotting Superconducting Resonator Data", IEEE Transactions on Applied Superconductivity **27**, 1–5 (2017) (Cited on pages 29, 118).

[100] L. J. Swenson, P. K. Day, B. H. Eom, H. G. Leduc, N. Llombart, C. M. McKenney, O. Noroozian, and J. Zmuidzinas, "Operation of a titanium nitride superconducting microresonator detector in the nonlinear regime", Journal of Applied Physics **113**, 104501 (2013) (Cited on pages 30, 34, 118, 119, 121).

[101] S. Moseley, R. Kelley, R. Schoelkopf, A. Szymkowiak, D. McCammon, and J. Zhang, "Advances toward high spectral resolution quantum X-ray calorimetry", IEEE Transactions on Nuclear Science **35**, 59–64 (1988) (Cited on page 35).

[102] A. E. Szymkowiak, R. L. Kelley, S. H. Moseley, and C. K. Stahle, "Signal processing for microcalorimeters", Journal of Low Temperature Physics **93**, 281–285 (1993) (Cited on page 35).

[103] J. W. Fowler, B. K. Alpert, W. B. Doriese, J. Hays-Wehle, Y.-I. Joe, K. M. Morgan, G. C. O'Neil, C. D. Reintsema, D. R. Schmidt, J. N. Ullom, and D. S. Swetz, "When "Optimal Filtering" Isn't", IEEE Transactions on Applied Superconductivity **27**, 1–4 (2017) (Cited on pages 35, 40, 43).

[104] G. Ulbricht, B. A. Mazin, P. Szypryt, A. B. Walter, C. Bockstiegel, and B. Bumble, "Highly Multiplexible Thermal Kinetic Inductance Detectors for X-Ray Imaging Spectroscopy", Applied Physics Letters **106**, 251103 (2015) (Cited on page 37).

[105] **N. Zobrist**, B. H. Eom, P. Day, B. A. Mazin, S. R. Meeker, B. Bumble, H. G. LeDuc, G. Coiffard, P. Szypryt, N. Fruitwala, I. Lipartito, and C. Bockstiegel, "Wide-band parametric amplifier readout and resolution of optical microwave kinetic inductance detectors", Applied Physics Letters **115**, 042601 (2019) (Cited on pages 37, 84, 87, 90, 91, 137).

[106] J. W. Fowler, B. K. Alpert, W. B. Doriese, Y. I. Joe, G. C. O'Neil, J. N. Ullom, and D. S. Swetz, "The Practice of Pulse Processing", Journal of Low Temperature Physics **184**, 374–381 (2016) (Cited on page 37).

[107] J. Gao, L. R. Vale, J. A. Mates, D. R. Schmidt, G. C. Hilton, K. D. Irwin, F. Mallet, M. A. Castellanos-Beltran, K. W. Lehnert, J. Zmuidzinas, and H. G. Leduc, "Strongly quadrature-dependent noise in superconducting microresonators measured at the vacuum-noise limit", Applied Physics Letters **98**, 232508 (2011) (Cited on pages 38, 72, 75).

[108] J. W. Fowler, B. K. Alpert, W. B. Doriese, D. A. Fischer, C. Jaye, Y. I. Joe, G. C. O'Neil, D. S. Swetz, and J. N. Ullom, "Microcalorimeter Spectroscopy at High Pulse Rates: a Multi-Pulse Fitting Technique", The Astrophysical Journal Supplement Series **219**, 35 (2015) (Cited on page 40).

[109] B. K. Alpert, R. D. Horansky, D. A. Bennett, W. B. Doriese, J. W. Fowler, A. S. Hoover, M. W. Rabin, and J. N. Ullom, "Note: Operation of gamma-ray microcalorimeters at elevated count rates using filters with constraints", Review of Scientific Instruments **84**, 056107 (2013) (Cited on pages 40, 112).

[110] J. W. Fowler, C. G. Pappas, B. K. Alpert, W. B. Doriese, G. C. O'Neil, J. N. Ullom, and D. S. Swetz, "Approaches to the Optimal Nonlinear Analysis of Microcalorimeter Pulses", Journal of Low Temperature Physics **193**, 539–546 (2018) (Cited on page 40).

[111] B. Shank, J. J. Yen, B. Cabrera, J. M. Kreikebaum, R. Moffatt, P. Redl, B. A. Young, P. L. Brink, M. Cherry, and A. Tomada, "Nonlinear optimal filter technique for analyzing energy depositions in TES sensors driven into saturation", AIP Advances **4**, 117106 (2014) (Cited on page 40).

[112] D. Yan, T. Cecil, L. Gades, C. Jacobsen, T. Madden, and A. Miceli, "Processing of X-ray Microcalorimeter Data with Pulse Shape Variation using Principal Component Analysis", Journal of Low Temperature Physics **184**, 397–404 (2016) (Cited on page 40).

[113] S. E. Busch, J. S. Adams, S. R. Bandler, J. A. Chervenak, M. E. Eckart, F. M. Finkbeiner, D. J. Fixsen, R. L. Kelley, C. A. Kilbourne, S.-J. Lee, S. H. Moseley, J.-P. Porst, F. S. Porter, J. E. Sadleir, and S. J. Smith, "Progress Towards Improved Analysis of TES X-ray Data Using Principal Component Analysis", Journal of Low Temperature Physics **184**, 382–388 (2016) (Cited on page 40).

[114] J. M. Miller, **N. Zobrist**, G. Ulbricht, and B. A. Mazin, "Improving the energy resolution of photon counting microwave kinetic inductance detectors using principal component analysis", Journal of Astronomical Telescopes, Instruments, and Systems **7**, 1–10 (2021) (Cited on page 40).

[115] D. J. Fixsen, S. H. Moseley, B. Cabrera, and E. Figueroa-Feliciano, "Pulse estimation in nonlinear detectors with nonstationary noise", Nuclear Instruments and Methods in Physics Research Section A: Accelerators, Spectrometers, Detectors and Associated Equipment **520**, 555–558 (2004) (Cited on page 40).

[116] D. J. Fixsen, S. H. Moseley, T. Gerrits, A. E. Lita, and S. W. Nam, "Optimal Energy Measurement in Nonlinear Systems: An Application of Differential Geometry", Journal of Low Temperature Physics **176**, 16–26 (2014) (Cited on page 40).

[117] S. Golwala, "Exclusion Limits on the WIMP-Nucleon Elastic-Scattering Cross Section from the Cryogenic Dark Matter Search", PhD thesis (Berkeley, 2000) (Cited on pages 41, 111).

[118] **N. Zobrist**, N. Klimovich, B. Ho Eom, G. Coiffard, M. Daal, N. Swimmer, S. Steiger, B. Bumble, H. G. LeDuc, P. Day, and B. A. Mazin, "Improving the dynamic range of single photon counting kinetic inductance detectors", Journal of Astronomical Telescopes, Instruments, and Systems **7**, 010501 (2021) (Cited on pages 48, 86, 87, 91).

[119] T. Guruswamy, D. J. Goldie, and S. Withington, "Quasiparticle generation efficiency in superconducting thin films", Superconductor Science and Technology **27**, 055012 (2014) (Cited on page 50).

[120] K. O'Brien, B. Mazin, S. McHugh, S. Meeker, and B. Bumble, "ARCONS: a Highly Multiplexed Superconducting UV-to-Near-IR Camera", Proceedings of the International Astronomical Union **7**, 385–388 (2012) (Cited on page 50).

[121] J. C. van Eyken, M. J. Strader, A. B. Walter, S. R. Meeker, P. Szypryt, C. Stoughton, K. O'Brien, D. Marsden, N. K. Rice, Y. Lin, and B. A. Mazin, "The Arcons Pipeline: Data Reduction for Mkid Arrays", The Astrophysical Journal Supplement Series **219**, 14 (2015) (Cited on page 50).

[122] S. R. Meeker, "DARKNESS: The First Microwave Kinetic Inductance Detector Integral Field Spectrograph for Exoplanet Imaging", PhD thesis (University of California, Santa Barbara, 2017) (Cited on page 50).

[123] A. Walter, B. A. Mazin, C. Bockstiegel, N. Fruitwala, P. Szypryt, I. Lipartito, S. Meeker, **N. Zobrist**, G. Collura, G. Coiffard, P. Strader, O. Guyon, J. Lozi, and N. Jovanovic, "MEC: the MKID exoplanet camera for high contrast astronomy at Subaru (Conference Presentation)", in Ground-based and Airborne Instrumentation for Astronomy VII, Vol. 10702, edited by H. Takami, C. J. Evans, and L. Simard (July 2018), p. 31 (Cited on pages 50, 80).

[124] A. B. Walter, "MEC : The MKID Exoplanet Camera for High Speed Focal Plane Control at the Subaru Telescope", PhD thesis (UC Santa Barbara, 2019) (Cited on page 50).

[125] B. A. Mazin, "Superconducting materials for microwave kinetic inductance detectors", 2020, arXiv:2004.14576 [astro-ph.IM] (Cited on page 50).

[126] H. G. Leduc, B. Bumble, P. K. Day, B. H. Eom, J. Gao, S. Golwala, B. a. Mazin, S. McHugh, A. Merrill, D. C. Moore, O. Noroozian, A. D. Turner, and J. Zmuidzinas, "Titanium nitride films for ultrasensitive microresonator detectors", Applied Physics Letters **97**, 102509 (2010) (Cited on page 51).

[127] P. Szypryt, B. A. Mazin, G. Ulbricht, B. Bumble, S. R. Meeker, C. Bockstiegel, and A. B. Walter, "High quality factor platinum silicide microwave kinetic inductance detectors", Applied Physics Letters **109**, 151102 (2016) (Cited on pages 51, 57, 58, 145).

[128] N. Fruitwala, P. Strader, G. Cancelo, T. Zmuda, K. Treptow, N. Wilcer, C. Stoughton, A. B. Walter, **N. Zobrist**, G. Collura, I. Lipartito, J. I. Bailey, and B. A. Mazin, "Second generation readout for large format photon counting microwave kinetic inductance detectors", Review of Scientific Instruments **91**, 124705 (2020) (Cited on page 52).

[129] A. G. Kozorezov, J. K. Wigmore, D. Martin, P. Verhoeve, and A. Peacock, "Phonon Noise in Thin Metal Films in an Advanced Energy Down-Conversion Stage", Journal of Low Temperature Physics **151**, 51–57 (2008) (Cited on pages 53, 90, 105, 141, 142).

[130] A. Peacock, "On the development of superconducting tunnel junctions as photon counting spectrometers for application in astrophysics", Physica B: Condensed Matter **263-264**, 595–603 (1999) (Cited on page 53).

[131] S. Kraft, A. J. Peacock, M. Bavdaz, B. Castelletto, B. Collaudin, D. Perez, R. Venn, and T. E. Harper, "Use of hafnium-based superconducting tunnel junctions as high-resolution spectrometers for X-ray astronomy", in Proceedings of

SPIE, Vol. 3445, edited by O. H. W. Siegmund and M. A. Gummin (Nov. 1998), pp. 226–235 (Cited on pages 53, 105).

[132] J. Hunacek, J. Bock, C. M. Bradford, V. Butler, T.-C. Chang, Y.-T. Cheng, A. Cooray, A. Crites, C. Frez, S. Hailey-Dunsheath, B. Hoscheit, D. W. Kim, C.-T. Li, D. Marrone, L. Moncelsi, E. Shirokoff, B. Steinbach, G. Sun, I. Trumper, A. Turner, B. Uzgil, A. Weber, and M. Zemcov, "Hafnium Films and Magnetic Shielding for TIME, A mm-Wavelength Spectrometer Array", Journal of Low Temperature Physics **193**, 893–900 (2018) (Cited on page 53).

[133] A. E. Lita, B. Calkins, L. A. Pellouchoud, A. J. Miller, and S. Nam, "Superconducting transition-edge sensors optimized for high-efficiency photon-number resolving detectors", in Proceedings of SPIE: Advanced Photon Counting Techniques IV, Vol. 7681, edited by M. A. Itzler and J. C. Campbell (Apr. 2010), p. 76810D (Cited on page 53).

[134] G. Coiffard, M. Daal, **N. Zobrist**, N. Swimmer, S. Steiger, B. Bumble, and B. A. Mazin, "Characterization of sputtered hafnium thin films for high quality factor microwave kinetic inductance detectors", Superconductor Science and Technology **33**, 07LT02 (2020) (Cited on pages 55, 64, 98, 100, 105).

[135] *Sonnet Software*, http://www.sonnetsoftware.com/ (visited on 03/22/2022) (Cited on page 56).

[136] M. R. Vissers, J. Gao, M. Sandberg, S. M. Duff, D. S. Wisbey, K. D. Irwin, and D. P. Pappas, "Proximity-coupled Ti/TiN multilayers for use in kinetic inductance detectors", Applied Physics Letters **102**, 232603 (2013) (Cited on pages 57, 58).

[137] O. Jepsen, O. K. Andersen, and A. R. Mackintosh, "Electronic structure of hcp transition metals", Physical Review B **12**, 3084–3103 (1975) (Cited on page 59).

[138] R. Barends, H. L. Hortensius, T. Zijlstra, J. J. A. Baselmans, S. J. C. Yates, J. R. Gao, and T. M. Klapwijk, "Contribution of dielectrics to frequency and noise of NbTiN superconducting resonators", Applied Physics Letters **92**, 223502 (2008) (Cited on page 59).

[139] M. Žemlička, P. Neilinger, M. Trgala, M. Rehák, D. Manca, M. Grajcar, P. Szabó, P. Samuely, Š. Gaži, U. Hübner, V. M. Vinokur, and E. Il'ichev, "Finite quasiparticle lifetime in disordered superconductors", Physical Review B **92**, 224506 (2015) (Cited on page 59).

[140] P. C. J. J. Coumou, E. F. C. Driessen, J. Bueno, C. Chapelier, and T. M. Klapwijk, “Electrodynamic response and local tunneling spectroscopy of strongly disordered superconducting TiN films”, Physical Review B **88**, 180505 (2013) (Cited on page 59).

[141] J. B. Johnson, “Thermal agitation of electricity in conductors”, Physical Review **32**, 97–109 (1928) (Cited on page 67).

[142] H. Nyquist, “Thermal agitation of electric charge in conductors”, Physical Review **32**, 110–113 (1928) (Cited on page 67).

[143] S. Letzter and N. Webster, “Noise in amplifiers”, IEEE Spectrum **7**, 67–75 (1970) (Cited on page 69).

[144] C. M. Caves, “Quantum limits on noise in linear amplifiers”, Physical Review D **26**, 1817–1839 (1982) (Cited on pages 70, 71, 134).

[145] J. Gao, M. Daal, A. Vayonakis, S. Kumar, J. Zmuidzinas, B. Sadoulet, B. A. Mazin, P. K. Day, and H. G. Leduc, “Experimental evidence for a surface distribution of two-level systems in superconducting lithographed microwave resonators”, Applied Physics Letters **92**, 152505 (2008) (Cited on pages 72, 74).

[146] J. Gao, M. Daal, J. M. Martinis, A. Vayonakis, J. Zmuidzinas, B. Sadoulet, B. A. Mazin, P. K. Day, and H. G. Leduc, “A semiempirical model for two-level system noise in superconducting microresonators”, Applied Physics Letters **92**, 2–5 (2008) (Cited on page 72).

[147] S. E. de Graaf, L. Faoro, J. Burnett, A. A. Adamyan, A. Y. Tzalenchuk, S. E. Kubatkin, T. Lindström, and A. V. Danilov, “Suppression of low-frequency charge noise in superconducting resonators by surface spin desorption”, Nature Communications **9**, 1143 (2018) (Cited on page 74).

[148] A. Megrant, C. Neill, R. Barends, B. Chiaro, Y. Chen, L. Feigl, J. Kelly, E. Lucero, M. Mariantoni, P. J. J. O’Malley, D. Sank, A. Vainsencher, J. Wenner, T. C. White, Y. Yin, J. Zhao, C. J. Palmstrøm, J. M. Martinis, and A. N. Cleland, “Planar superconducting resonators with internal quality factors above one million”, Applied Physics Letters **100**, 113510 (2012) (Cited on page 74).

[149] G. Calusine, A. Melville, W. Woods, R. Das, C. Stull, V. Bolkhovsky, D. Braje, D. Hover, D. K. Kim, X. Miloshi, D. Rosenberg, A. Sevi, J. L. Yoder, E. Dauler, and W. D. Oliver, “Analysis and mitigation of interface losses in trenched superconducting coplanar waveguide resonators”, Applied Physics Letters **112**, 062601 (2018) (Cited on page 74).

[150] O. Noroozian, J. Gao, J. Zmuidzinas, H. G. LeDuc, and B. A. Mazin, "Two-level system noise reduction for Microwave Kinetic Inductance Detectors", AIP Conference Proceedings **1185**, 148–151 (2009) (Cited on page 74).

[151] S. Beldi, F. Boussaha, C. Chaumont, S. Mignot, F. Reix, A. Tartari, T. Vacelet, A. Traini, M. Piat, and P. Bonifacio, "Design of Near Infrared and Visible Kinetic Inductance Detectors Using MIM Capacitors", Journal of Low Temperature Physics **193**, 184–188 (2018) (Cited on page 74).

[152] M. R. Vissers, M. P. Weides, J. S. Kline, M. Sandberg, and D. P. Pappas, "Identifying capacitive and inductive loss in lumped element superconducting hybrid titanium nitride/aluminum resonators", Applied Physics Letters **101**, 022601 (2012) (Cited on pages 74, 95).

[153] **N. Zobrist**, M. Daal, J. Y. Corbin, B. Sadoulet, and B. Mazin, "Disk Resonator Design for Kinetic Inductance Detectors", Journal of Low Temperature Physics **194**, 394–403 (2019) (Cited on page 74).

[154] S. Beldi, F. Boussaha, J. Hu, A. Monfardini, A. Traini, F. Levy-Bertrand, C. Chaumont, M. Gonzales, J. Firminy, F. Reix, M. Rosticher, S. Mignot, M. Piat, and P. Bonifacio, "High Q-factor near infrared and visible Al2O3-based parallel-plate capacitor kinetic inductance detectors", Optics Express **27**, 13319 (2019) (Cited on page 74).

[155] N. Wadefalk, A. Mellberg, I. Angelov, M. E. Barsky, S. Bui, E. Choumas, R. W. Grundbacher, E. L. Kollberg, R. Lai, N. Rorsman, P. Starski, J. Stenarson, D. C. Streit, and H. Zirath, "Cryogenic wide-band ultra-low-noise IF amplifiers operating at ultra-low DC power", IEEE Transactions on Microwave Theory and Techniques **51**, 1705–1711 (2003) (Cited on page 74).

[156] J. Schleeh, H. Rodilla, N. Wadefalk, P. Å. Nilsson, and J. Grahn, "Characterization and modeling of cryogenic ultralow-noise InP HEMTs", IEEE Transactions on Electron Devices **60**, 206–212 (2013) (Cited on page 74).

[157] J. Schleeh, G. Alestig, J. Halonen, A. Malmros, B. Nilsson, P. A. Nilsson, J. P. Starski, N. Wadefalk, H. Zirath, and J. Grahn, "Ultralow-power cryogenic InP HEMT with minimum noise temperature of 1 K at 6 GHz", IEEE Electron Device Letters **33**, 664–666 (2012) (Cited on page 74).

[158] C. Macklin, K. O'Brien, D. Hover, M. E. Schwartz, V. Bolkhovsky, X. Zhang, W. D. Oliver, and I. Siddiqi, "A near-quantum-limited Josephson traveling-wave parametric amplifier", Science **350**, 307–310 (2015) (Cited on page 75).

[159] J. Zmuidzinas and P. K. Day, "Dispersion-Engineered Traveling Wave Kinetic Inductance Parametric Amplifier", 2014 (Cited on page 75).

[160] S. Chaudhuri, D. Li, K. D. Irwin, C. Bockstiegel, J. Hubmayr, J. N. Ullom, M. R. Vissers, and J. Gao, "Broadband parametric amplifiers based on nonlinear kinetic inductance artificial transmission lines", Applied Physics Letters **110**, 152601 (2017) (Cited on pages 75, 77).

[161] B. H. Eom, P. K. Day, H. G. Leduc, and J. Zmuidzinas, "A wideband, low-noise superconducting amplifier with high dynamic range", Nature Physics **8**, 623–627 (2012) (Cited on pages 75, 76).

[162] M. R. Vissers, R. P. Erickson, H. S. Ku, L. Vale, X. Wu, G. C. Hilton, and D. P. Pappas, "Low-noise kinetic inductance traveling-wave amplifier using three-wave mixing", Applied Physics Letters **108**, 012601 (2016) (Cited on page 77).

[163] T. I. Baturina, Y. A. Tsaplin, A. E. Plotnikov, and M. R. Baklanov, "Anomalous Behavior near Tc and Synchronization of Andreev Reflection in Two-Dimensional Arrays of SNS Junctions", JETP Letters **81**, 10–14 (2005) (Cited on page 83).

[164] U. Fano, "Ionization Yield of Radiations. II. The Fluctuations of the Number of Ions", Physical Review **72**, 26–29 (1947) (Cited on page 90).

[165] M. Kurakado, "Possibility of High Resolution Detectors Using Superconducting Tunnel Junctions", Nuclear Instruments and Methods in Physics Research **196**, 275–277 (1982) (Cited on pages 90, 144, 145).

[166] N. Rando, A. Peacock, A. van Dordrecht, C. Foden, R. Engelhardt, B. Taylor, P. Gare, J. Lumley, and C. Pereira, "The properties of niobium superconducting tunneling junctions as X-ray detectors", Nuclear Instruments and Methods in Physics Research Section A: Accelerators, Spectrometers, Detectors and Associated Equipment **313**, 173–195 (1992) (Cited on pages 90, 144, 145).

[167] P. J. de Visser, S. A. de Rooij, V. Murugesan, D. J. Thoen, and J. J. Baselmans, "Phonon-Trapping-Enhanced Energy Resolution in Superconducting Single-Photon Detectors", Physical Review Applied **16**, 034051 (2021) (Cited on pages 90, 92, 103, 110, 141, 142).

[168] A. G. Kozorezov, J. K. Wigmore, D. Martin, P. Verhoeve, and A. Peacock, "Electron energy down-conversion in thin superconducting films", Physical Review B **75**, 094513 (2007) (Cited on pages 90, 105, 139).

[169] H. Ehrenreich, H. R. Philipp, and B. Segall, "Optical Properties of Aluminum", Physical Review **132**, 1918–1928 (1963) (Cited on page 92).

[170] S. B. Kaplan, “Acoustic matching of superconducting films to substrates”, Journal of Low Temperature Physics **37**, 343–365 (1979) (Cited on pages 94, 95, 104, 107, 139, 142, 144, 145).

[171] W. A. Little, “THE TRANSPORT OF HEAT BETWEEN DISSIMILAR SOLIDS AT LOW TEMPERATURES”, Canadian Journal of Physics **37**, 334–349 (1959) (Cited on page 94).

[172] X. Qi, X. Wang, T. Chen, and B. Li, “Experimental and first-principles studies on the elastic properties of α-hafnium metal under pressure”, Journal of Applied Physics **119**, 125109 (2016) (Cited on pages 95, 144).

[173] G. Destgeer, J. H. Jung, J. Park, H. Ahmed, K. Park, R. Ahmad, and H. J. Sung, “Acoustic impedance-based manipulation of elastic microspheres using travelling surface acoustic waves”, RSC Advances **7**, 22524–22530 (2017) (Cited on page 95).

[174] E. Dechaumphai, D. Lu, J. J. Kan, J. Moon, E. E. Fullerton, Z. Liu, and R. Chen, “Ultralow thermal conductivity of multilayers with highly dissimilar Debye temperatures”, Nano Letters **14**, 2448–2455 (2014) (Cited on page 96).

[175] A. Giri and P. E. Hopkins, “A Review of Experimental and Computational Advances in Thermal Boundary Conductance and Nanoscale Thermal Transport across Solid Interfaces”, Advanced Functional Materials **30**, 1903857 (2020) (Cited on page 96).

[176] K. Karatsu, A. Endo, J. Bueno, P. J. de Visser, R. Barends, D. J. Thoen, V. Murugesan, N. Tomita, and J. J. A. Baselmans, “Mitigation of cosmic ray effect on microwave kinetic inductance detector arrays”, Applied Physics Letters **114**, 032601 (2019) (Cited on page 97).

[177] A. P. Vepsäläinen, A. H. Karamlou, J. L. Orrell, A. S. Dogra, B. Loer, F. Vasconcelos, D. K. Kim, A. J. Melville, B. M. Niedzielski, J. L. Yoder, S. Gustavsson, J. A. Formaggio, B. A. VanDevender, and W. D. Oliver, “Impact of ionizing radiation on superconducting qubit coherence”, Nature **584**, 551–556 (2020) (Cited on page 97).

[178] R. D. Chaudhari and J. B. Brown, “Critical Currents in Superconducting Films of Indium”, Physical Review **139**, A1482–A1488 (1965) (Cited on page 97).

[179] J. M. Martinis, G. C. Hilton, K. D. Irwin, and D. A. Wollman, “Calculation of TC in a normal-superconductor bilayer using the microscopic-based Usadel theory”, Nuclear Instruments and Methods in Physics Research, Section A: Accelerators,

Spectrometers, Detectors and Associated Equipment **444**, 23–27 (2000) (Cited on pages 100, 140).

[180] A. Fyhrie, J. Glenn, P. Day, H. G. LeDuc, J. Zmuidzinas, and C. M. McKenney, "Progress towards ultra sensitive KIDs for future far-infrared missions: a focus on recombination times", in Millimeter, Submillimeter, and Far-Infrared Detectors and Instrumentation for Astronomy IX, edited by J. Zmuidzinas and J.-R. Gao (Aug. 2018), p. 109 (Cited on page 101).

[181] **N. Zobrist**, W. H. Clay, G. Coiffard, M. Daal, N. Swimmer, P. Day, and B. A. Mazin, "Membrane-less phonon trapping and resolution enhancement in optical microwave kinetic inductance detectors", 2022, arXiv:2204.13669 [astro-ph.IM] (Cited on page 107).

[182] S. E. Thompson, S. Withington, D. J. Goldie, and C. N. Thomas, "Dynamical behaviour of superconducting microresonators with readout-power heating", Superconductor Science and Technology **26**, 095009 (2013) (Cited on page 118).

[183] P. J. de Visser, S. Withington, and D. J. Goldie, "Readout-power heating and hysteretic switching between thermal quasiparticle states in kinetic inductance detectors", Journal of Applied Physics **108**, 114504 (2010) (Cited on page 118).

[184] M. Malnou, M. Vissers, J. Wheeler, J. Aumentado, J. Hubmayr, J. Ullom, and J. Gao, "Three-Wave Mixing Kinetic Inductance Traveling-Wave Amplifier with Near-Quantum-Limited Noise Performance", PRX Quantum **2**, 010302 (2021) (Cited on page 137).

[185] A. G. Kozorezov, C. Lambert, F. Marsili, M. J. Stevens, V. B. Verma, J. P. Allmaras, M. D. Shaw, R. P. Mirin, and S. W. Nam, "Fano fluctuations in superconducting-nanowire single-photon detectors", Physical Review B **96**, 054507 (2017) (Cited on page 139).

[186] H. Koc, E. Deligöz, and A. M. Mamedov, "The elastic, electronic, and optical properties of PtSi and PtGe compounds", Philosophical Magazine **91**, 3093–3107 (2011) (Cited on page 145).

[187] E. J. Graeber, R. J. Baughman, and B. Morosin, "Crystal structure and linear thermal expansivities of platinum silicide and platinum germanide", Acta Crystallographica Section B Structural Crystallography and Crystal Chemistry **29**, 1991–1994 (1973) (Cited on page 145).